DIRECTING THE MIGRATION OF MESENCHYMAL STEM CELLS AND BYSTANDER CELLS USING SUPERPARAMAGNETIC IRON OXIDE NANOPARTICLES

A Thesis
Presented to
The Academic Faculty

by

David Christopher Sotto

In Partial Fulfillment
of the Requirements for the Degree
Doctor of Philosophy in Bioengineering in the
School of Mechanical Engineering

Georgia Institute of Technology
May 1, 2015

DIRECTING THE MIGRATION OF MESENCHYMAL STEM CELLS AND BYSTANDER CELLS USING SUPERPARAMAGNETIC IRON OXIDE NANOPARTICLES

Approved by:

Dr. Gang Bao, Advisor
School of Mechanical Engineering
Georgia Institute of Technology

Dr. Michelle Dawson
School of Chemical and Biomolecular Engineering
Georgia Institute of Technology

Dr. Johnna Temenoff
School of Biomedical Engineering
Georgia Institute of Technology

Dr. Raphael Lee
School of Medicine
University of Chicago

Dr. Todd Sulchek
School of Mechanical Engineering
Georgia Institute of Technology

Date Approved: February, 27, 2015

To my mother Ileana and my grandfather Pablo

ACKNOWLEDGEMENTS

I am extremely grateful to my advisor, Dr. Gang Bao, for all of his guidance, help and support. His patience and guidance as an advisor and mentor have been invaluable to me. I would like to thank the members of my thesis committee, Dr. Michelle Dawson, Dr. Raphael Lee, Dr. Todd Sulchek, and Dr. Johnna Temenoff for generously giving of their time and expertise to my project.

To the past and present members of Bao Lab, thank you for the foundation you have built and for your help with this research. In particular, I would like to thank Dr. Sheng Tong and Chris Quinto for their help and expertise on this project. I also would like to thank our lab manager Annie for her help with cellular studies and lab management. Finally, I would like to thank my present and past undergraduate students, Andrea Fernandez, Jenny Lin, Christian Jreige, Camila Rodriguez, and Abhinaya Uthayakumar for their help throughout the years and wish them happy and successful careers.

Finally, I would like to thank my family for all their support and encouragement through the past 6 years. I would like to especially thank my father for his constant love, support, and positive outlook on life. He has suffered from a number of diabetic ulcers in his life and almost lost his leg in more than one occasion. This research work is motivated by his experiences and pains realized through poor treatment.

TABLE OF CONTENTS

	Page
ACKNOWLEDGEMENTS	iv
LIST OF TABLES	viii
LIST OF FIGURES	ix
LIST OF SYMBOLS AND ABBREVIATIONS	xi
SUMMARY	xiii
CHAPTER	
1 INTRODUCTION	1
CENTRAL HYPOTHESIS	3
SPECIFIC AIM 1	4
SPECIFIC AIM 2	5
SPECIFIC AIM 3	6
2 RESEARCH SIGNIFICANCE	8
3 LITERATURE REVIEW	10
IRON OXIDE NANOPARTICLES	12
MECHANICS OF CELL MOTILITY	14
Persistent Random Walking	14
Dendritic Nucleation	15
Protrusion	16
Graded Adhesion	17
MESENCHYMAL STEM CELL	18
Mesenchymal Stem Cell Secretome	20
MAGNETIC CELL MANIPULATION	21

4 MATERIALS AND METHODS 25
NANOPARTICLE DELIVERY 25
SPEED AND PERSISTENCE MOTILITY MODEL 27
MECHANICAL STRESS ON MSC ADHESIONS 29
MECHANICAL STRESS ON MSC PROTRUSIONS 31
MECHANICAL STRESS ON MSC SECRETION 33
MOTILITY OF NHEK UNDER MIGRATORY FACTORS 35
MIGRATION SECRETION IN MIXED MEDIA 36
5 DIRECTED MIGRATION OF SPIO LABELED MSCS 39
INTRODUCTION 39
RESULTS 40
Nanoparticle Delivery 40
Speed And Persistence 45
Comparative Model For Persistent Random Walk 49
DISCUSSION 55
CONCLUSION 57
6 CELL RESPONSE TO MAGNETIC FORCE LOADING 58
INTRODUCTION 58
RESULTS 59
Protrusions 59
Adhesions 62
Cell Stiffness 68
Cytoskeletal Response 68
Cell Area And Shape 74
DISCUSSION 78

CONCLUSION 81

7 BYSTANDER CELL MIGRATION 82

INTRODUCTION 82

MSC Secretome 84

Keratinocytes 85

Migratory Signaling Cytokines 86

RESULTS 87

DISCUSSION 93

CONCLUSION 95

8 CONCLUSION 96

IMPROVING THE SPIO-MAGNETIC FIELD SYSTEM 97

ADDITIONAL SECRETION FACTORS AND CELL REPROGRAMMING 99

APPENDIX A: ADDITIONAL REFERENCE CELL IMAGES 100

VITA 104

REFERENCES 105

LIST OF TABLES

Page

Table 1.1: Magnetic Nanoparticles and Surface Modification in Cell Manipulation 3

Table 5.1: Superparamagnetic Iron Oxide Nanoparticle Characterization 39

Table 7.1: Kown Promigratory Cytokines for Keratinocytes 86

LIST OF FIGURES

Page

Figure 3.1: SPIO Core Size and Magnetization 13

Figure 3.2: Role of MSCs in Regenerative Medicine 19

Figure 3.3: MNP labeled Tie2 Receptors Promote Tubulogenesis 22

Figure 3.4: MNP mediated EGFR Clustering 23

Figure 3.5: MNP and AMF Controlled Apoptosis in Cancer Cells 24

Figure 5.1: Schematic of SPIO Delivery Method 41

Figure 5.2: Heatmap of the Magnitude of the Gradient of the Magnetic Field for a 4 Grid Maget Array 42

Figure 5.3: Iron Loading and Delivery Efficiency of SPIOs in MSCs 44

Figure 5.4: MSC Viability after SPIO Delivery 45

Figure 5.5: Speed and Persistence Schematic 47

Figure 5.6: MSC and NIH/3T3 Cell Mobility Speed and Persistence 48

Figure 5.7: Comparative Persistent Random Walk Schematic and Conditions 50

Figure 5.8: Cell Trajectories of Comparative Persistent Random Walking 51

Figure 5.9: MSD of Comparative Persistent Random Walking 52

Figure 5.10: Directionality Ratio of Persistent Random Walking 52

Figure 5.11: Autocorrelation of Persistent Random Walking 53

Figure 5.12: Average Speed of MSCs during PRW Model 53

Figure 5.13: Average Speed of MSCs versus Distance from Magnet 54

Figure 6.1: Resultant Force and Directional Components of SPIO-MSCs 58

Figure 6.2: MSC Protrusion Schematic 60

Figure 6.3: MSD for MSCs and SPIO-MSC under x-y Component Force 61

Figure 6.4: Adherence Ratio of MSCs for Varying Incubation Times and Centrifugal Detachment Forces 64

Figure 6.5: Cell Attachment Rate for +/- SPIO-MSCs 65

Figure 6.6: Adherence Ratio for +/- SPIO-MSCs 66

Figure 6.7: Rate of Cell Spreading by Area-Fold Change 67

Figure 6.8: Immunofluorochemistry Signal Distribution Across Cell Length 70

Figure 6.9: DiI-SPIO Signal Isolation 71

Figure 6.10: F-Actin Signal Isolation 71

Figure 6.11: Vinculin Signal Isolation 72

Figure 6.12: Beta-1 Integrin Signal Isolation 73

Figure 6.13: Tubulin Signal Isolation 73

Figure 6.14: Cell Area Reported by Median and Middle 50% 75

Figure 6.15: Cell Area, Roundness, and Aspect Ratio after Cytochalasin D Treatment 76

Figure 6.16: Cell Area, Roundness, and Aspect Ratio after Nocodazole Treatment 77

Figure 6.17: Cell Area, Roundness, and Aspect Ratio after Blebbistatin Treatment 78

Figure 7.1: Summary of the Role of Vinculin in Cell Biology 83

Figure 7.2: MSC Secretion ELISA Schematic 88

Figure 7.3: VEGF, HGF, and TGF beta 1 Secretion Levels of MSCs 89

Figure 7.4: Coculture Media Optimization 90

Figure 7.5: HGF/TGF beta 1 Effect on NHEK Transwell Migration 92

Figure 7.6: Transwell Migration of NHEK cells in MSC Conditioned Media 93

Figure 8.1: Nickel Microrod Magnetophoresis of SPIO Encapsulated Vesicles 98

LIST OF SYMBOLS AND ABBREVIATIONS

MSC	Mesenchymal Stem Cell
NIH/3T3	Murine Fibroblasts with 3T3 cycle
NHEK	Neonatal Human Epidermal Keratinocyte
KBM/KGM-Gold	Keratinocyte Basal Media/Growth Media
MSCBM/MSCGM	Mesenchymal Stem Cell Basal Media/Growth Media
MNP	Magnetic Nanoparticle
IONP/SPIO	Iron Oxide Nanoparticle/Superparamagnetic Iron Oxide
Fe_3O_4	Magnetite
Fe_2O_3	Maghemite
EF	Electric Field
MF	Magnetic Field
F_M	Magnetic Force
acac	Acetylacetonate
DSPE	1,2-distearoyl-sn-glycero-3-phosphoethanolamine
PEG/mPEG	polyethylene glycol/methyl-polyethylene glycol
TEM	Transition Electron Microscopy
SQUID	Superconducting Quantum Interference Device
MRI	Magnetic Resonance Imaging
NdFeB	Neodynium Iron Boron Magnet
HGF/SF	Hepatocyte Growth Factor/Scatter Factor
SDF-1	Stromal Cell Derived Factor 1
TGF-beta-1	Transforming Growth Factor beta 1

VEGF	Vascular Endothelial Growth Factor
IGF-1	Insulin-like Growth Factor 1
EGF	Epidermal Growth Factor
FGF	Fibroblast Growth Factor
Tie2	Angiopoietin-2 Receptor
ADP/ATP	Adenoside Diphosphate/Triphosphate
GTPase	Guanosine Triphosphate Hydrolizing Enzyme
MMP-9	Matrix Metallopeptidase 0
WASP	Wiskott-Aldrich Syndrome Protein
Arp2/3	Actin Related Protein 2/3
PLC	Phospholipase C
PKC	Protein Kinase C
APC	Adenomatous Polyposis Coli
ROS/RNS	Reactive Oxygen Species/Nitrogen Species
PRW	Persistent Random Walk
MSD	Mean Square Displacement
VACF	Velocity Autocorrelation Function

SUMMARY

Cell migration plays an important role in numerous normal and pathological processes. The physical mechanisms of adhesion, protrusion/extension, contractions, and polarization can regulate cell migration speed, persistence time, and downstream effects in paracrine and endocrine signaling. Methods for understanding these biophysical and biochemical responses to date have been limited to the use of external forces acting on mechanotransductive receptors. Additionally, as the use of magnetic nanoparticles for cell tracking and cell manipulation studies continues to gain popularity, so does the importance of understanding the cellular response to mechanical forces caused by these magnetic systems.

This thesis work utilizes superparamagnetic iron oxide nanoparticles and static magnets to induce an endogenous magnetic force on the cell membrane. This cell manipulation model is used to better understand the mechanobiological responses of mesenchymal stem cell to SPIO labeling and endogenous force generation. Directionally persistent motility, cytoskeletal reorganization, and altered pro-migratory cytokine secretion is reported in this thesis as a response to SPIO based cell manipulation.

CHAPTER 1

INTRODUCTION

Cell migration plays an important role in numerous normal and pathological processes. Physical mechanisms of adhesion, protrusion/extension, contractions, and polarization can regulate cell migration speed, persistence time, and downstream effects in paracrine and endocrine signaling. Methods for understanding these biophysical and biochemical responses to date have been limited to the use of external forces acting on mechanotransductive receptors. The focus of this thesis is to utilize a superparamagnetic iron oxide nanoparticle labeled cell system to induce a measureable force on the cytosolic membrane for understanding how it affects mesenchymal stem cell (MSC) adhesions, protrusions, paracrine secretion, migration speed and persistence, and migration effects to bystander keratinocytes.

Electrotherapy and stem cell therapy have emerged over the past decade as possible treatment methods for complex acute and chronic wounds that fail to respond to standard treatment [1-3]. Although they bring a novel approach and mechanism for treatment, each falls short of a truly effective advanced wound healing therapy. Electrotherapy delivers a constant voltage across a wound space improving microcirculation and prompting electrotaxis of cells toward the device anode [4-6]. Although this technology has reported promising results *in vitro*, further development in clinical settings have been limited by the skewing affect tissue has on electric field lines [6]. In contrast, stem cells (and especially mesenchymal stem cells) have produced promising results in *in vivo* studies for advanced wound healing [7-10]. Even one human

trial treating 1-year long chronic wounds non-responsive to standard treatment reported wound closure using bone marrow derived-MSC seeded autologous skin grafts as quickly as 2 weeks after engraftment [11]. Understanding that the improved healing capability of MSCs can be bolstered by its recruitment and migration into the wound space paired with the a directed migration technique similar to electrotherapy I proposed to explore the basic cell mechanisms behind the potential to accelerate cutaneous wound healing by magnetically directing super paramagnetic iron oxide (SPIO) labeled MSCs into the wound space.

This research direction is only a small part of the realm of magnetic cell manipulation. Biofunctional magnetic nanoparticles have been utilized to manipulate cell functions primarily driven by interactions with surface bound protein through antibody labeling. Recent publications in magnetic cell manipulation have garnered much attention and covering an expansive variety of topics including cell tracking, shepherding and homing, cell creeping, patterning, cell separation, suspended cell culture, and receptor clustering. Although many of these new developments are exciting and validate the usefulness of magnetic nanparticles in biological applications many common concerns have been raised for both *in vitro* and *in vivo* studies utilizing these techniques. Disappearance of delivered nanoparticles from the transplanted site in tissue cultures has been reported as a common yet unexplained occurrence. Poor transplantation and integration efficiency of nanoparticle containing cells and disruption of cell-cell interactions have also been reported in magnetic nanoparticle containing cells for regenerative medicine applications [12].

Table 1. MNPs and Surface Modifications in Cell Manipulation.

Nanoparticle	Size(nm)	Ligand/antibody	protein
Co/Fe_2O_3, $SmCo_{5.2}/Fe_2O_3$	8.5, 9.5	NTA	His-GFP
FePt	3	NTA	His-GFP
$Silica/Fe_2O_3$	630	Ni^{2+} salts impregnation	histidine-tagged protein
MNP	10	terpyridine	histidine-tagged protein
Fe_3O_4	15	aminophenylboronic acid	glycoprotein
Ni/NiO	13	imidazole	His-GFP
Au/Fe_3O_4	4/20	NTA	histidine-tagged protein
Fe_2O_3	200-400	goat anti-mouse, anti-rabbit, and anti-human(H+L)antibodies	human, rabbit, mouse IgG
Fe_3O_4	12	$silane/Cu^{2+}$	histidine-tagged protein
iron oxide	10	Ni/NiO	histidine-tagged GFP
Fe_3O_4	50	TiO_2	phosphopeptides
Fe_3O_4	6	GSH	GST-tagged protein
Fe_3O_4	6	TMP	eDHFR tagged protein
γ-Fe_2O_3	<9	double-stranded RNA[poly(IC)]	35 kDa protein
Fe_xO_y	5-100	anti-rabbit IgG	protein A
magnetic bead	300	secondary antibody	S100ββ antigens
Fe_3O_4	10	CRP antibody	CRP
Fe_3O_4	5–15	antibody	SAA, CRP, SAP
Fe_3O_4/TiO_2		IgG	
Fe_3O_4	220	NTA	histidine-tagged protein
Fe_3O_4	5-15	NTA	histidine-tagged protein
Fe_3O_4	20	NTA	histidine-tagged protein
BacMP	80-120	antibody	protein A
Fe_3O_4	40	hydrophobic chains	BSA

With such a significant number of current magnetic nanoparticle types paired with so much academic and clinical interest in their applications within regenerative medicine it is surprising that there is such a poor understanding of cellular mechanobiology when manipulated by magnetic nanoparticles [13]. Prior to exploring the potential of developing yet another magnetic nanoparticle based application for regenerative medicine applications, a firm understanding of the influence that magnetic nanoparticles have on stem cell mechanobiology should be studied.

Central Hypothesis

Forces produced by superparamagnetic iron oxide nanoparticles paired with external static magnets produce measureable effects to the mechanical response system of mesenchymal stem cells. To address this hypothesis, three specific aims were pursued.

Specific Aim 1: Directed Migration of SPIO loaded MSCs

In order to understand the potential that iron loaded cells have in directed migration when under a magnetic field there are a number of factors that must first be evaluated. Iron loading of cells through pinocytic/endocytic nanoparticle delivery methods must be determined and optimized for a range of nanoparticle sizes and quantities. An emphasis is placed on uniform delivery and threshold iron levels per cell in order to induce an internal stress on the cell membrane.

Iron loaded cells are expected to migrate in the direction of a magnetic field driven by attraction to the highest magnetic field gradient. The attractive force acting on the nanoparticles should translate into an internal stress on the cell body that can drive cell migration at a measureable speed and direction. This speed and direction should be dependent on bulk iron loading, particle size, number of particles, and magnitude and direction of the magnetic field and its gradient. These conditions can be optimized to measure a maximum directional speed. Considering that these MSCs would be loaded with high iron content, changes to morphology and physiology will be determined and is the focus of Aim 2. Also, since there will be a substantial force acting on the SPIOs, nanoparticle retention would be a concern as well [14]. Magnetofected SPIOs have been shown to stay in cells for over 7 days and we believe that the behavior of directional force under migratory conditions when dealing with nanoparticle should not have a change in retention within the short time frames studied.

Iron loaded cells can be used to specifically direct migration under static magnetic fields when internalized into MSCs by internal mechanical stress. Work previously done

on magnetic force calculations on magnetic nano- and micro-beads in microrheology studies through the use of magnetic tweezers and other static and dynamic magnetic fields, have shown that the force exerted on an individual iron nanoparticle can range from 500-2400 pN. A similar although unique model was developed for the SPIOs I intend to use measuring up to a force of 20.8 pN on a single particle of core size of 14.7 nm under a gradient field of 180 mT strength. Under this model and at an iron loading of 4.5-7 pg of Fe/cell and particle quantity of 1.45 million particles/cell an internal force of over 30 μN can be exerted on the cell body. This accounts for a significant force over adhesive and drag forces acting on a cell body under migratory culture conditions allowing for a net resultant force in the direction of the magnetic field. For mesenchymal cell types, adhesion forces range from 480-650 dyne/cm^2 in culture on a collagen coated surface [15].

Specific Aim 2. Cellular response under magnetic force loading

Iron loading and substantial internal force loads are foreign influences to MSCs and can substantially alter cellular behavior. In order to determine affects to cell behavior analysis of morphological changes to the cell body must be completed, and a thorough understanding of changes to cell physiology under iron loading and internal stress. MSC mechanotransduction can also be better understood by the use of this new method for inducing mechanical stress on the cell body. There has not been a previously reported method for inducing cell body stress without the use of an external stress/strain or ligand-receptor binding of membrane bound receptors (primarily integrin) to ECM or modifiable bound particles or surfaces [16].

We hypothesize that an internal mechanical stress on the cell membrane will induce modifications of the cytoskeleton that prompts paracrine/autocrine signaling. Mechanical stress from externally bound integrin have reported measureable affects to alpha helical stretch in talin which is believed to upregulate vinculin binding in crytic sites on force loaded talin (above 12 pN). Vinculin binding signals a number of downstream affects including the recruitment of paxillin which is essential to the maturation of focal adhesions and docking for tyrosine kinases and phosphatases. This should create a measurable effect to both nascent focal adhesions and actin polymerization in cell protrusions.

Specific Aim 3. Directed migration of bystander cells by SPIO-MSCs

SPIO labeled MSCs when activated by a magnetic field could increase focal adhesion area, which regulated a number of migratory signaling pathways primarily mediated through morphological changes from internal mechanical stress initiating Rho-GTPase/ROCK-signaling pathway and integrin-talin/Wnt signalling pathway that affects regulation of a number of transcription factors not exclusive to cell migration [17].

Upregulation of paracrine activity in migrating MSCs have shown induced migration of bystander keratinocytes, fibroblasts, macrophages, and epithelial cells. Particularly through the release of HGF and SDF-1 and is believes to contribute to the creation of chemical gradients in tissue when migrating towards a wound site [17]. The exact mechanism for bystander migration is not well understood and both paracrine signaling and cell-cell interactions through anchoring junctions and direct contact of receptor protein have been theorized. We hypothesize that HGF and SDF-1 secretion

from MSCs while directionally migrating can create local chemical gradients that direct bystander keratinocytes towards a specified migration direction.

Collectively, these studies contribute to a better understanding of mesenchymal mechanobiology specific to mechanical force loading from MNPs and static magnets. The results herein shed light on how activated SPIOs affect the migratory response, cytoskeletal tensile response, and cytokine secretion of mesenchymal stem cells. As MNP cell manipulation developments continue, this contribution will enable design improvements of sophisticated stem cell programming and directed function studies and ultimately avenues into wound healing applications.

CHAPTER 2

RESEARCH SIGNIFICANCE

The use of magnetic nanoparticles (MNPs) has expanded precipitously in recent years as their potential for biomedical applications as a magnetic resonance imaging contrast agent was first discovered decades ago and its cellular labeling techniques has been substantially developed since. Despite this progress there have been numerous concerns raised that have limited the translation of magnetically labeled cells as an interesting novelty to applications within the regenerative and wound healing healthcare space [18]. Multiple reports of cell disappearance after transplantation in vivo has gone unexplained for years and the possibility of MNPs as a passive imaging label does not quite hold [19, 20]. The studies explored in this thesis help add to the understanding of mesenchymal stem cell (MSC) biomechanics proving that even small common magnets can induce dynamic force responses within cell populations that cannot be considered passive. The applied gradient magnetic fields are significantly lower than tissue is traditionally exposed to by magnetic resonance imaging (MRI) and therefore are relevant to current and future applications of MNP labeled cells of this design.

MNP labeled MSCs without any exposure to a magnetic field suffer from poor adhesion, measureable overall cell stiffness, cytoskeletal reorganization that substantially deviates from unlabeled MSCs, and altered cell-spreading rates as reported in this thesis. These same cells when exposed to gradient magnetic fields of magnitude as low as 40 mT can recover from many of these ailments and in some cases even exhibit an enhanced ability to migrate in a controlled, directional manner with an overall increase in average speed and directional persistence. These magnetically stressed MSCs experience a force substantial enough to cause active reorganization of cytoskeletal, relocalization of focal adhesion protein expression, and prompt sensory mechanisms that alter paracrine

signaling for two promigratory cytokines studied herein. These finding confirm that MNP labeling even in the presence of low gradient magnetic fields play an active role in MSC mechanobiological responses that have design implications for cell manipulation studies both *in vitro* and *in vivo*. These reports would be of tremendous value to the MNP cell manipulation community as well as the wound healing and regenerative medicine research community who so readily utilized MSCs and cell tracking methods.

CHAPTER 3

LITERATURE REVIEW

Wound repair is an orchestra of highly integrated biological and molecular events of cell migration, proliferation, extracellular matrix deposition, and remodeling [21]. There are a number of advanced therapies used for wound care, the most common of which include: bioengineered tissue, negative pressure wound therapy, and hyperbaric oxygen therapy [2]. Among emerging technology, electrotherapy and stem cell therapy have produced the most promising clinical results and are expected to become more commonly used to treat challenging acute and chronic wounds [2, 21].

Within the field of wound healing and regenerative medicine, the American Society of Mechanical Engineers' NanoEngineering for Medicine and Biology Steering Committee has identified three primary challenges to address in order to advance this field of research [22]:

1. Establishing a better understanding of the biological processes that impact wound healing
2. Determining how to accurately model, measure, and control the wound healing processes using engineering techniques
3. Developing and applying advanced engineering techniques for wound healing that incorporate mechanical, chemical, and/or electrical approaches.

This project addresses all three areas by aiming to understand the biological process of wound healing as it pertains to cellular recruitment and migration for MSCs and

epidermal keratinocytes, computational modeling and empirical validation of directed healing treatments, and the incorporation of electromagnetic and mechanical approaches to a biological problem.

SPIO labeled MSCs have been reported to maintain multipotency even at high iron concentrations, are non-toxic, and can be safely and effectively internalized by cells through magnetofection [23-25]. Utilizing magnetic fields to direct cell migration is expected to translate well into *in vivo* studies as MFs are not dependent on tissue composition as EFs are [26, 27]. MFs are limited by their field strength and penetration depth but this is only a minimal concern when interacting with cutaneous wounds with high strength neodymium-iron magnets. Additionally, MSC treatments have established benchmarks, facilitating the validation of a potential treatment's safety and efficacy [7-9]. Understanding the mechanical effects that force induced migration have on MSCs is a necessary first step in developing and improving wound healing stem cell therapies. The core steps of adhesion and protrusion in cell migration is not completely understood and can lead to discoveries directly addressing the shortcomings of MSC engraftment, dispersion, and retention.

Additionally, developing technologies to treat chronic wounds has tremendous incentives such as low cost, at-home care, and improved compliance by both patients and providers [21, 22]. Current treatment types still suffer from poor success rates and remain a challenge despite efforts to develop novel techniques. RNAi and molecular approaches have failed in clinical trials and a significant need is left unmet for a safe and effective treatment method.

Iron oxide nanoparticles

Superparamagnetic iron oxide nanoparticles have been used for a wide variety of *in vivo* applications in the past decade such as a MR imaging contrast agent, detoxification of biologics, hyperthermia, drug delivery, cell separation, and immunoassays among others [28, 29]. This particle type has become so useful because of its high magnetization, small size, narrow particle size distribution, and versatility in functional coating techniques [12]. The unique property of superparamagnetism and its subsequent ability for an individual particle to exert a translational force is exploited in this thesis.

SPIOs exhibit no magnetization in suspension and remain magnetically inactive unless acted upon by an external magnetic field and retain no magnetism after the removal of that magnetic field [29]. When magnetically active, SPIOs can exhibit a high magnetic saturation and become attracted to the magnetic field gradient [28]. Active particles with a sufficiently high magnetic field gradient can transverse space along magnetic field lines, exerting a force on its environment [24].

In our lab, we have developed a new method for synthesizing SPIOs with strong control over their diameter and surface chemistry [30]. SPIOs are synthesized in two steps. First, 6 nm iron oxide nanocrystals are synthesized by thermal decomposition of $Fe(acac)_3$ in the presence of oleic acid, oleylamine, 1,2-hexadecanediol, and benzyl ether. Iron oxide nanocrystals of size 14.9 nm are used for all experiments in this thesis work and are obtained by continuous seed-mediated growth of the 6 nm iron oxide nanocrystals with 2-3 nm growth steps until the desired diameter is reached [23]. Water-dispersible SPIOs are generated by a minor surface modification of the hydrophobic

nanocrystals with a layer of DSPE-mPEG, lipid PEG, through dual solvent-exchange of first DMSO then water. The specific nanocrystal used for these studies were synthesized by the Bao lab and have a core diameter of 14.9 nm and magnetization curves for a range of core sizes are shown in Figure 3.1.

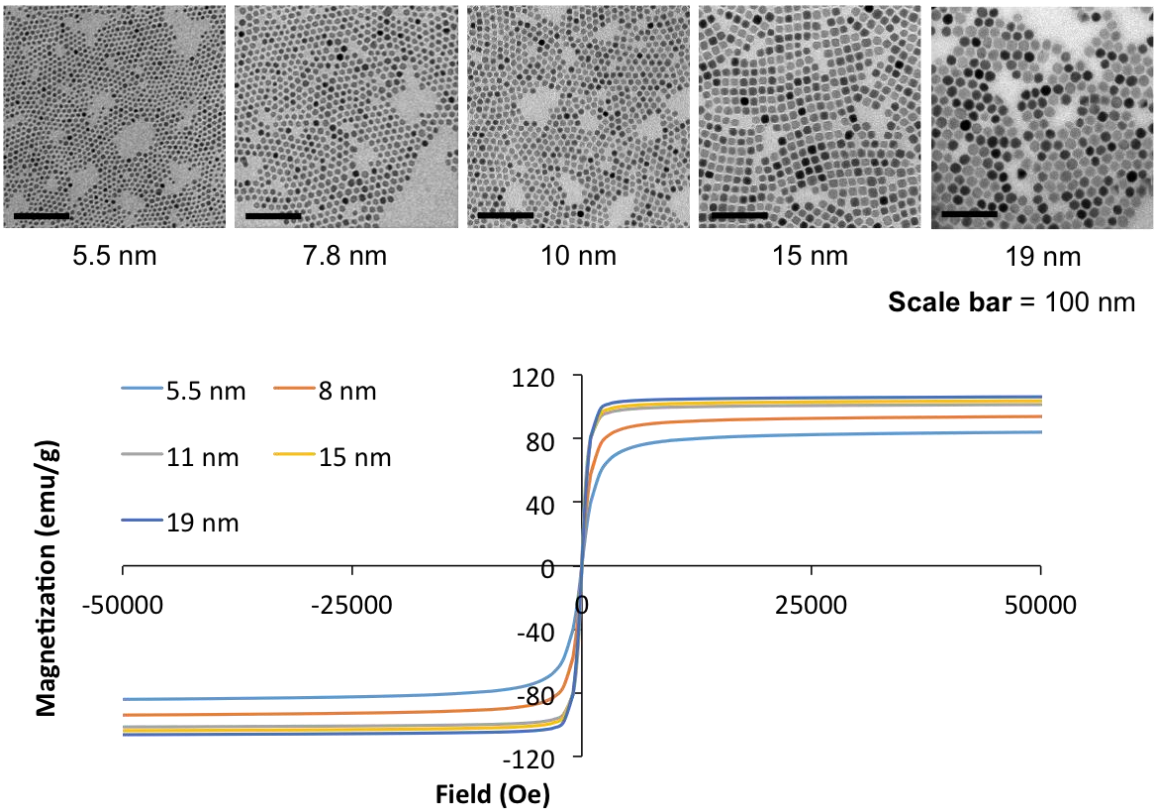

Figure 3.1. SPIO Core Size and Magnetization. Bao lab synthesized Iron Oxide core sized are displayed (top) by transition electron microscopy for core sizes ranging from 5.5 nm - 19 nm. Each core's respective magnetization curve is shown (bottom) in emu/gram for a full magnetic field range.

The significance of this new synthesis and coating method is that it allows for a range of iron content, particle size, and functional coatings when optimizing particle delivery, migration speeds, cell retention, and toxicity.

Mechanics of Cell Motility

For three centuries the mechanics of cell crawling has been a heavy focus of cell and molecular bioengineering, ever since van Leeuwenhoek discovered "pleasing and nimble" motions of tiny creatures in rainwater that put forth little horns, extended and contracted [31]. This simple model of leading edge extensions, graded adhesions across the cell body, and finally contractions that pull up the rear has been essential in understanding the underlying layers of complexity in the motile cycle through experimental research and mathematical modeling, especially in the last four decades [32].

Persistent Random Walking

Among basic motility models, the persistent random motion of cells has been most commonly explained based on the Ornstein-Uhlenbeck process as the archetypal model [33, 34].

$$\frac{d\mathbf{v}}{dt} = -\frac{1}{\tau}\mathbf{v} + \frac{\sqrt{2D}}{\tau}\boldsymbol{\xi}(t) \qquad (1)$$

$$\langle \mathbf{r}^2(t) \rangle = 2nD\tau(e^{-t/\tau} + t/\tau - 1) \qquad (2)$$

$$\langle \mathbf{v}(t)\mathbf{v}(0) \rangle = \frac{nD}{\tau}e^{-t/\tau} \qquad (3)$$

This process if defined by the Langevin equation (1). For the velocity vector v, [] representing a vector with white-noise components, D as the diffusion coefficient characteristic of Brownian motion, and the timescale tau representing persistence time [34]. Its popular use can be attributed to the fact that the Fürth formula (2) describing mean square displacement (MSD) and velocity autocorrelation functions (VACF) (3)

have been experimentally observed to fit its predicted behavior for numerous cell times. A number of more advanced motility models have been developed and explored since this cell-walking model to explain functional subsystems of motility [31].

Dendritic Nucleation hypothesis and network contraction model

The prevailing model for lamellipodial motility relies on self-organization of actin filaments into motile networks in leading edge based on dendritic nucleation along growing filaments and myosin-powered contraction along aged filaments in the lagging edge [35]. The lamellipod is the motile engine of the cell and is located at the front, advancing edge. It is characterized by a flat leaf-like extension filled with a dense rectangular actin network and is sometimes noted to contain multiple layers of varying crosslinking and actin density. According to this model, nascent actin filaments branch from the sides of existing filaments so that there is a 70° angle between the mother and daughter filaments, and all the leading edge filaments' barbed ends are oriented forward at about 35° to the direction of the protrusion [35]. Barbed end elongation has been reported to be ~0.1 μm/sec and push out the leading edge membrane. These protruding barbed edged have been reported to extend to 0.1-1μm before being capped. Once capped, a new generation of actin filaments must push the leading edge membrane. All the while the actin filament pointed ends are being disassembled into G-actin subunits in a process called treadmilling.

Myosin contraction occurs on the lagging edge of the cell. Myosin molecules are distributed throughout the cell body and are the motor protein that use ATP hydrolysis to glide toward actin barbed ends. These myosin cannot interact with highly cross-linked

actin filament networks as are common in the lamellipodia but can much more easily interact in the aged disassembled actin filaments at the rear of the cell. This ability only to interact in the cell rear coupled with the graded adhesions across the cell membrane, where stronger adhesions exist at the leading edge and weaker ones at the lagging edge, allows for lagging edge membrane retraction toward the cell body creating a net translation across a surface.

The molecular machinery involved in this lamellipodial treadmilling is first believed to be the activation of GTPases and phosphoinositides who then activate WASP/Scar proteins which in turn activate Arp2/3 protein complexes nucleating nascent actin filaments at the side of the existent filaments [32, 35]. F-actin is disassembled into G-actin monomers across the lamellipod by proteins of the ADF/cofilin family and these G-actin subunits associated with ADF/cofilin are rapidly exchanged with profilin and thymosin and ADP-ATP exchange [35]. ATP active G-actin monomers then diffuse to the barbed end and contribute to F-actin polymerization.

Protrusion: Polymerization Brownian Ratchet Model

The dendritic nucleation model explains the forward creation of lamellipodia by actin polymerization but fails to explain a cause for creation of the nucleation sites [32]. The protrusion ratchet model delves more deeply into the mechanics of protrusion creation and contains an elegant mathematical model of actin nucleation in protrusions by ratcheting, a step-wise force loading on actin filaments creating kinks that allows for monomeric integration and dendritic nucleation [36]. This model hypothesizes that the creation of a gap in F-actin filaments in the front maintains high concentrations of G-

actin monomers by creating additional locations for polymerization besides that of the uncapped barbed end [36]. These force-load-created gaps can also be used to explain force-based motility persistence in future models. The protrusion ratchet model predicts that one filament can generate a force in the pN range ~1 pN and if grown to an ideal length between 70-500 nm can bend under the load of the leading edge membrane [36]. This elastic tension pushes filaments to the cell sides while creating nucleation sites toward the center of the membrane protrusion. The location and force load in the filament might contribute to the specific angular polymerization of daughter filaments at ± 35° to the direction of the protrusion [32, 36]. Mechanical stress on individual actin filaments and bulk stress to the cell membrane can restructure the manner in which protrusions are made, making it an interesting area to explore with internal stressors. Tension and compression limits for actin filaments and their subsequent polymerization rate and angles have yet to be reported under an internally exerted force.

Graded adhesion model

The most heavily published area of research on the topic of cell motility is adhesion. Adhesions are crucial for cell locomotion and precise gradients of adhesion ages and strengths determine the ability for cell locomotion [37]. The first principle of adhesions in cell motility is that strong adhesions in the leading edge and weak ones in the lagging edge are necessary for forward translocation of a cell. Without graded adhesion, contraction and protrusion would just recycle cytoskeleton. Adhesion aging is incompletely understood, a popular hypothesis is that adhesion age is determined by spatial gradients of regulatory molecules like calpain and that force loading of the velcro-

like mechanical and signaling protein near focal adhesion complexes are necessary for nascent adhesion maturation [37]. Talin, vinculin, paxillin, FAK, and alpha-actinin have been identified as the most crucial in adhesion formation but their contributions to adhesion aging has not been explored [37]. The graded adhesion model stands by a biphasic control of migration, if adhesions are too strong in the lagging edge then contraction cannot occur and if the adhesions in the leading edge are too weak then protrusion cannot occur. The precise graded adhesive strength has not been studied but is now possible with a controlled cytosolic stress made by an internal mechanical force altering the distribution of adhesion sites and strength.

Mesenchymal Stem Cells

Stem cells (and especially mesenchymal stem cells) have produced promising results in *in vivo* studies for advanced wound healing [7, 10, 38]. Marrow derived MSCs are mobilized into the peripheral circulation, engraft near adnexal structures in the skin, and are reported to promote wound closure by differentiation into keratinocytes and fibroblasts while initiating the release of ECM bound VEGF through upregulation of MMP-9 from environmental cues [8]. VEGF upregulation results in an angiogenic response accelerating wound healing and promoting wound closure [39]. MSC seeded collagen constructs have shown over 60% improved wound closure after 15 days in both acute and chronic wound mouse models [39]. Even one human trial treating 1-year long chronic wounds (non-responsive to standard advanced wound care techniques) reported wound closure using bone marrow derived-MSC seeded autologous skin grafts as quickly

as 2 weeks after a single treatment [11]. The potential MSCs have for wound treatment is substantial and can be improved by the use of directed migration [6, 40].

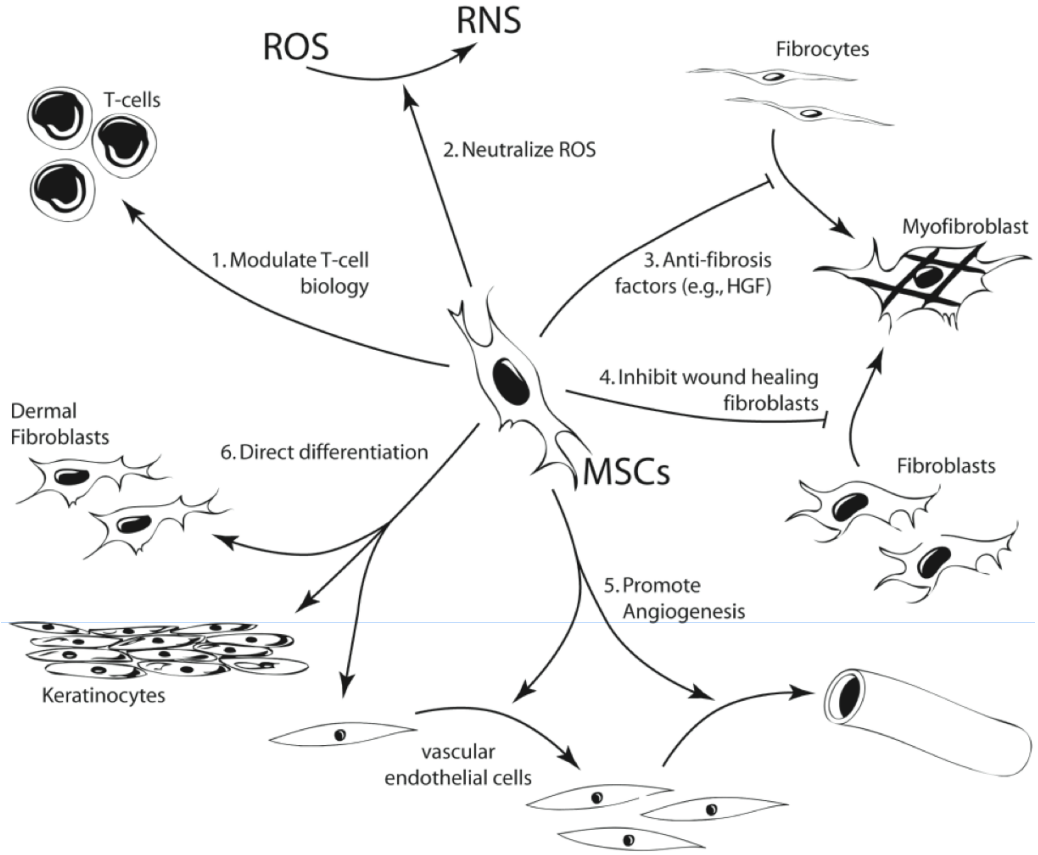

Figure 3.2. Role of MSCs in Regenerative Medicine. The multifaceted role of mesenchymal stem cells in regenerative medicine and six of the primary ways in which it interacts with the wound environment [8].

Mesenchymal stem cells can influence cutaneous regeneration by multiple distinct mechanisms acting on multiple cell types. These cellular events and interactions also have regenerative and preventative implications on advanced wound healing and scarring. HGF, hepatic growth factor; MSC, mesenchymal stem cells; RNS, reactive nitrogen species; ROS, reactive oxygen species [9].

The role of the MSC in wound healing is multifaceted. They are involved in immune cell signaling, management of reactive oxygen species, decreasing fibrosis by inhibiting fibroblast and fibrocyte conversion to myofibroblasts, the direct and indirect release of angiogenic factors including VEGF, and their potential for differentiation into keratinocytes, dermal fibroblasts, and a number of epithelial cell types [41, 42]. Despite this plentiful potential that MSCs provide as a wound healing therapeutic agent, the delivery and retention of MSCs in a wound space brings along a number of challenges [43, 44]. Three of the biggest challenges include: directed differentiation, cellular retention after injection, and directed migration from injection site or cell niches [6, 41, 44].

MSC Secretome

MSCs exhibit a set of pro-regenerative features that make them attractive candidates for modulation of cell and tissue responses and regenerative therapy approaches. MSCs have multi-lineage differentiation capacity, homing to sites of injury and inflammation, and paracrine pro-migratory, immunomodulatory, pro-angiogenic, anti-apoptotic, and pro-proliferative effects [45]. Most of this research conducted in tumor and wound microenvironments has produced a generally well understood (although some contradicting reports exist) MSC secretome including its paracrine and endocrine migratory secreted factors [46]. CCL5, TGF-β, VEGF, IL-17b, IGF-1, EGF, FGF, HGF, SDF1, IL-6 are all identified as pro-migratory secreted factors for a number of cancer cell lines both *in vitro* and *in vivo [45, 46]*. Although a number of these migratory factors have reported enhanced cell migration in wound healing studies; TGF-

β1, VEGF, IGF-1, EGF, FGF, HGF, and SDF1 report direct and measureable migratory effects on keratinocytes and fibroblasts *in vitro [37, 47]*. Signaling pathways for TGF-β1, IGF-1, EGF, VEGF, HGF, and SDF1 expression has substantially similar stimulatory (Wnt-GCPR, Integrin) and secondary signaling factors (Rho-GTPase, PLC, PKC, APC, IP3) as mechanotransduction pathways in MSCs allowing for the possible activation and up/down-regulation of these migratory factors under force loading conditions [37, 45].

Magnetic Cell Manipulation

Magnetic nanoparticles (MNPs) are one of the most well established nanomaterials due to its biocompatibility, functionalization potential, and widespread use as a functional contrast agent for magnetic resonance imaging. Recently, however, MNPs' usefulness has expanded over the last 5 years due to its ability to manipulate protein and cells as reported in qualitative and conceptual demonstrations in the literature [13]. What makes these MNP so interesting to the nanobiotechnology research community is the ability to manipulate these particles with an external magnetic force providing a action at a distance or a form of "remote" control. By using a range of surface modifications on a variety of MNPs, targeting of specific proteins and protein complex can be obtained. Recombinant protein purification and sorting by small ligand conjugated MNPs is one such example of protein manipulation in cell lysate [48]. Further developing this technique to label whole cells with functionalized nanoparticles at a sufficient quantity of iron has lead to MRI capability for cells in bulk, magnetic cell sorting, and more interestingly, single cell studies of membrane bound protein under attractive force influences [13].

Antibody conjugated MNPs can also interact directly with surface bound protein. These now magnetized receptors can be forced to cluster due to the magnetically-induced aggregation potential of some MNPs in order to control gain control over cell activities.

One such group demonstrated this by using a TiMo214 monoclonal antibody conjugated to a zinc-doped ferrite magnetic nanoparticle to target and manipulate Tie2 receptors with two static NdFeB magnets (Figure 3.3) [49]. Tie2 receptor aggregation is directly linked to downstream signaling and the group reported tubulogenesis of endothelial cells.

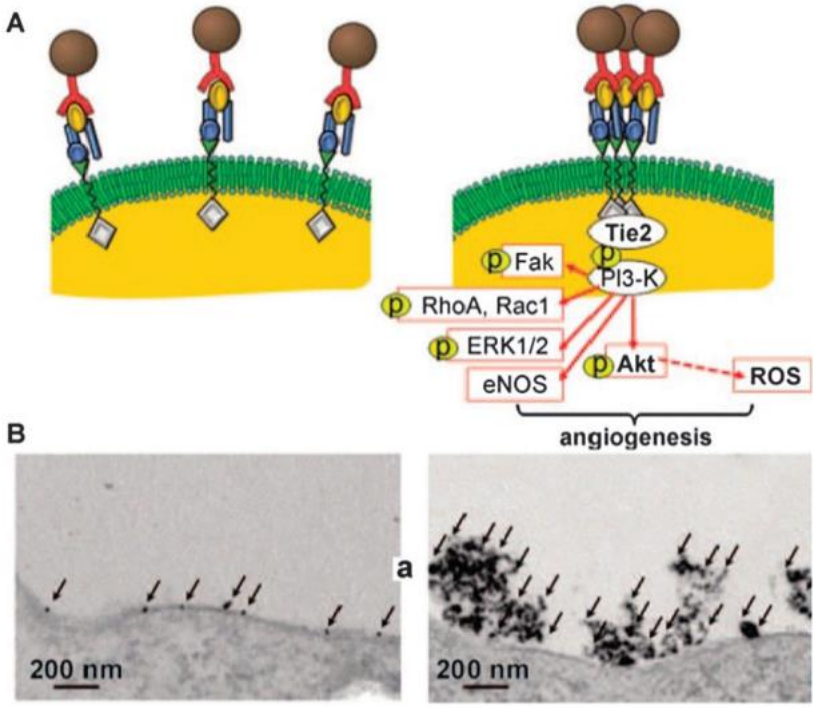

Figure 3.3 MNP labeled Tie2 Receptors Promote Tubulogenesis. (A) Depicts Zinc-doped ferrite nanoparticles clustering Tie2 surface receptors causeing a signaling cascade that promote angiogenesis. (B) Represents TEM images stained for iron showing an increase in nanoparticle clustering after the influence of a magnetic field (right) [49].

This ability to effect downstream signaling by targeting and aggregating surface bound receptors with MNPs was repeated for epidermal growth factor receptors in A431 cells with ligand-blocking monoclonal anti-EGFR antibody conjugated superparamagnetic iron oxide nanoparticles. This study reported activation of transphosphorylation and initiation of signaling cascades in quiescent cells, similar to those inherent to the ligand dependent EGFR pathway [50].

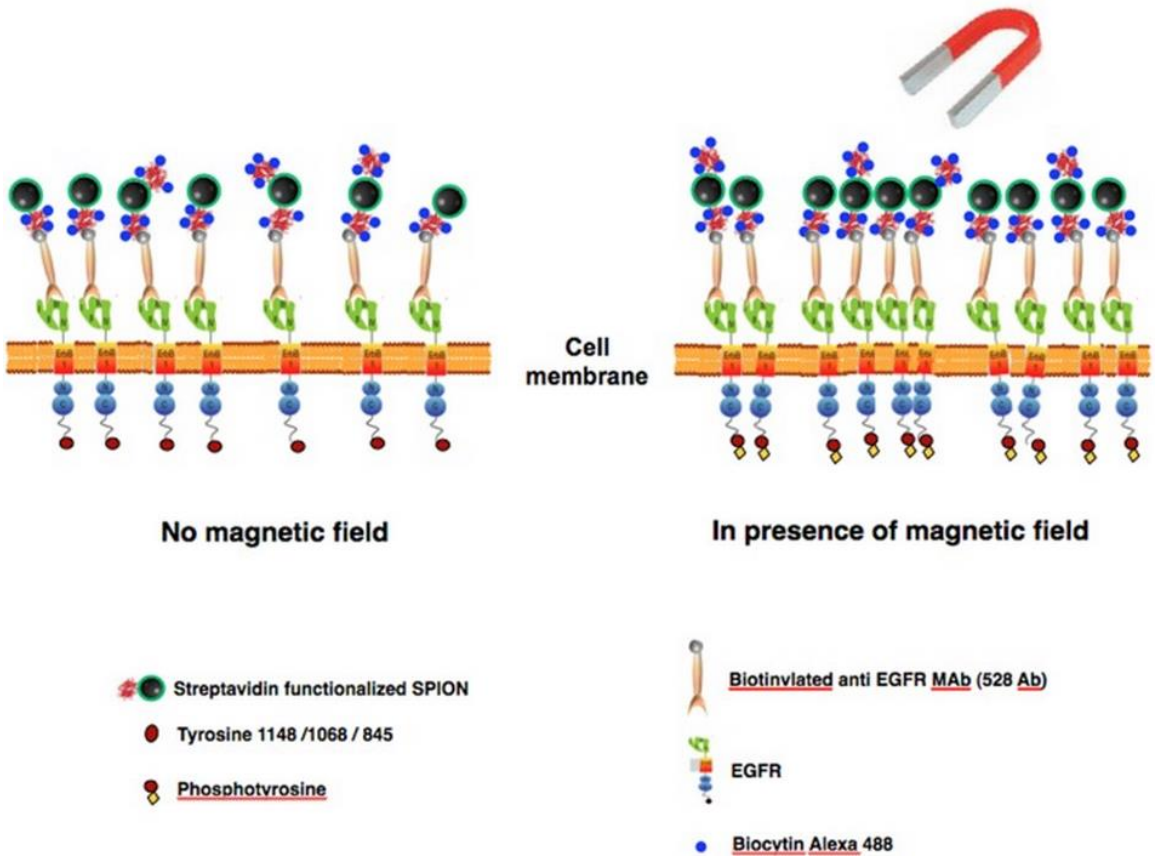

Figure 3.4. MNP Mediated EGFR Clustering. Streptavidin coated SPIOs were conjugated to biotinylated anti EGFR antibodies and made to aggregate surface bound EGFR when prompted by an external magnetic field [50, 51].

In addition to using unidirectional attractive forces cause by static magnets one group published the potential of MNPs causing mechanical forces by spin-vortex in a low frequency alternating magnetic field in order to induce apoptosis in several cancer cell lines. Anti-Interleukin13-alpha-2R antibody labeled magnetic microdiscs were made by nanolithography and selectively bound to the cancer cell membrane [24, 51].

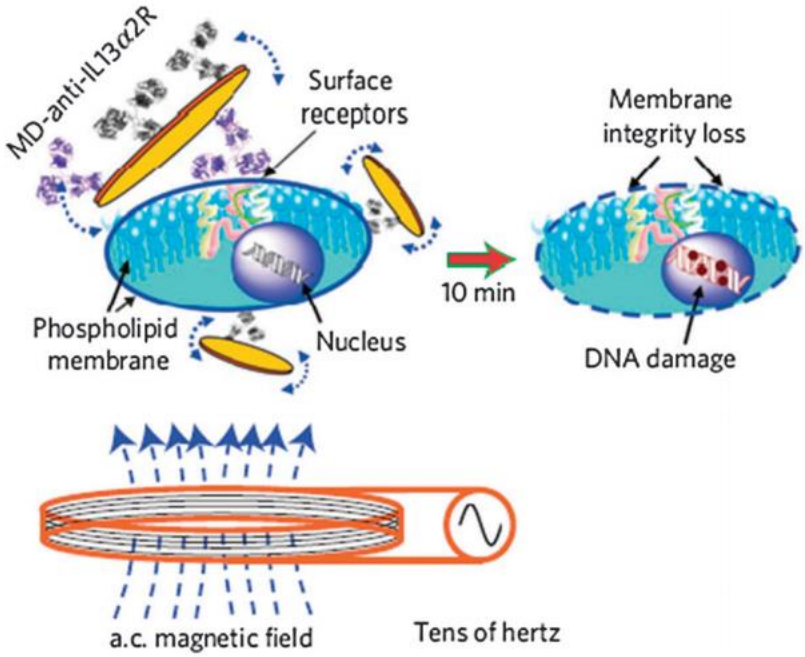

Figure 3.5. MNP and AMF Can Prompt Apoptosis in Cancer Cells. Magnetic microdiscs conjugated to surface bound receptors were caused to vibrate when influences by an alternating magnetic field leading to membrane integrity loss and apoptosis in cancer cell lines [51].

In the presence of an alternating magnetic field the disc begins to oscillate which transmits a mechanical force to the cell resulting in membrane destruction and ultimately apoptosis [51]. This low frequency field applied for only 10 minutes was sufficient to achieve over 90% cancer cell destruction in vitro [51]. These examples serve as a testament to the great potential superparamagnetic nanoparticles have in biological mechanics studies even with the use of simple strong magnets.

CHAPTER 4

MATERIALS AND METHODS

All materials and methods used for the experiments conducted in this thesis will be presented as the specific protocol with accompanied materials and suppliers.

Nanoparticle Delivery

Cell types:

hMSCs (Lonza) and NIH 3T3 murine fibroblasts (ATCC)

Media:

MSC-GM (Lonza), DMEM +10% FBS

Culture Conditions:

Cells seeded at 5000 cells/ cm^2 and grown until monolayer at 80% confluent (32000 cells/cm^2) into 4 well labtekII borosilicate glass chambers (poly-L-lysine coated for 3T3 fibroblasts only). Cells trypsinized with Trypsin-EDTA 0.25% in media, counted by automated cell counter (BioRad), dried in 1.5 mL eppendorf tubes and digested in 12M HCl for iron content measurements.

Nanoparticle:

Fe_3O_4 (Magnetite) cores of 5-15 nm diameters (synthesized in-house), dspe-PEG 2000 (Me) coated (Avanti polar lipids), coated diameters of 15-40 nm.

Magnetic plate:

Grid array of vertically oriented N42 NdFeB cylindrical magnets of diameter 2.54 mm and height of 25.4 mm.

Experimental conditions:

Two dimensional experimental design. Ranging SPIO sizes from 5-15 nm cores for varying spacer distances from the magnetic array ranging from 1-5.5 mm at the same cell density, media, and cell type.

Controls:

Non SPIO treated cells with no magnetic array, non-SPIO treated cells with magnetic array, SPIO treated cells with no magnetic array.

Repeats:

Each experimental condition was repeated in triplicate for each core size and each spacer length. Each experiment was repeated in triplicate with cells between P5-7.

Dye Labels:

SPIOs are conjugated with DiI fluorescent dye (549/564), cell nuclei are Hoescht dye labeled (352/461)

Equipment and Software:

DeltaVision fluorescent microscope, TECAN Safire Multiwell plate reader, MATLAB, ImageJ

Measurements:

Dual color fluorescent images were taken with DAPI and TRITC filter sets for 0.25 cm^2 area within each well of each chamber. Cells were counted by those having Hoescht labeled nuclei (T), and cells were counted containing SPIOs with DiI fluorescence (M). The percent of cells with successful SPIO delivery was calculated by M/T x 100.

Iron content per cell was measured by ferrozine assay by mixing 50 µL of 12M HCl for 30 minutes at RT on a shaker, then the solution is mixed with 240 µL of 2M NaOH, 50 uL of 4N ammonium acetate, and 110 µL of 5% hydroxylamine HCL for 30 minutes.

After incubation, 50 µL of the sample is mixed with 50 µL of 0.1% ferrozine solution and incubated for 15 minutes. Absorbance is read at 562 nm with an 810 nm reference and compared to an SPIO-only standard curve produces in the same fashion.

Cell viability will be measured by MTS assay after 24, 48, and 72 hours of SPIO delivery incubation.

Speed and Persistence Motility Model

Cell type:

hMSCs (Lonza) and NIH 3T3 murine fibroblasts (ATCC)

Media:

MSC-GM (Lonza) (Basal medium + bullet kit) +25 mM HEPES Buffer, DMEM +10% FBS + 25 mM HEPES Buffer

Culture Conditions:

Cells seeded at 5000 cells/ cm^2 and grown until monolayer at 80% confluent (32000 cells/cm^2) into 4 well labtekII borosilicate glass chambers (poly-L-lysine coated for 3T3 fibroblasts only). Cells trypsinized with Trypsin-EDTA 0.25% in media, counted by automated cell counter (BioRad), and reseeded at 40-50% confluent (16000-20000 cells/cm^2) into 1 well labtekII borosilicate glass chambers (poly-L-lysine coated for 3T3 fibroblasts only).

Nanoparticle:

Fe_3O_4 (Magnetite) cores nm diameters (synthesized in-house), dspe-PEG 2000-Me coated (Avanti polar lipids), coated diameters 40 nm.

Magnetic plate:

Dual bar magnetic array of horizontally oriented N52 NdFeB rectangular prism magnets of square cross-section 5 mm x 5 mm and length of 25 mm.

Experimental conditions:

Individual cells' speed and direction will be measured with respect to their path trace and the magnetic field trace for 4 hours of monitored time in 10 min increments. Mean square displacement of the cell body and cell nucleus will be measured versus time for a range of iron loading (# of particles/cell) and at varying distances from the magnetic surface (0-1000 μm in 100 μm increments). Cell areas containing 100-120 cells per panel will be monitored at each distance increment from the magnet surface.

Controls:

Non SPIO treated cells with no magnetic array, non-spio treated cells with magnetic array, SPIO treated cells with no magnetic array.

Repeats: Each experimental condition had three panels analyzed for each distance increment and each iron loading condition. Each experiment was repeated in triplicate with cells between P5-7.

Dye Labels:

SPIOs are conjugated with DiI fluorescent dye (549/564), cell nuclei are Hoescht dye labeled (352/461), and cell body is labeled with calceinAM cytosol stain (495/515).

Equipment and Software:

DeltaVision fluorescent microscope, microscope heat regulated objective box, MATLAB, ImageJ

Measurements:

Triple color fluorescent images were taken with DAPI, GFP, and TRITC filter sets for three 100-120 cell panels within each well of each chamber for each distance. Each individual cell per panel will have report a mean square displacement measured after each timepoint (10 min) and angular displacement by cos (theta), where theta is the angular displacement between the cell walk trace line and the magnetic field trace line. Startpoint to endpoint (6hrs) will be calculated in addition to each incremental speed and direction for variance from the ideal trace calculated by end-point analysis.

Mechanical stress on MSC adhesion

Cell type:

hMSCs (Lonza) and NIH 3T3 murine fibroblasts (ATCC)

Media:

MSC-GM (Lonza) (Basal medium + bullet kit) +25 mM, DMEM +10% FBS

Culture Conditions:

Cells seeded at 5000 cells/ cm^2 and grown until monolayer at 80% confluent (32000 cells/cm^2) into 1 well labtekII borosilicate glass chambers (poly-L-lysine coated for 3T3 fibroblasts only). SPIOs delivered at concentration of 100 ug/mL and incubated over cylindrical magnetic array at spacer length of 2.5 mm for 12 hours. Cells are trypsinized with Trypsin-EDTA 0.25% in media, counted by automated cell counter (BioRad), and reseeded at 40-50% confluent (16000-20000 cells/cm^2) onto a fibronectin coated coverslip for cell adhesion strength measurements via spinning disk device. Coverslip incubated over magnetic array for 0-12 hours and measured in 4 hour increments.

Equipment and Software:

DeltaVision fluorescent microscope, spinning disk device (Garcia Lab)

Measurements:

Cell adhesion strength measured as adhesion strength to glass slide or coated substrate quantified by using centrifugal detachment that applies a well-defined range of hydrodynamic force to adherent cells and provides sensitive reproducible measurements of adhesion strength. After spinning, cells are labeled with calceinAM and counted by photoluminescence measurements on a Tecan Safire Multiplate reader. Cell adhesion surface area was additionally calculated by direct vincullin staining at varying durations of magnetically induced adhesion to the coverslip.

Mechanical stress on MSC protrusion/extension

Cell type:

hMSCs (Lonza) and NIH 3T3 murine fibroblasts (ATCC)

Media:

MSC-GM (Lonza) (Basal medium + bullet kit) +25 mM, DMEM +10% FBS

Culture Conditions:

Cells seeded at 5000 cells/ cm^2 and grown until monolayer at 80% confluent (32000 cells/cm^2) into 1 well labtekII borosilicate glass chambers (poly-L-lysine coated for 3T3 fibroblasts only). SPIOs delivered at concentration of 100 ug/mL and incubated over cylindrical magnetic array at spacer length of 2.5 mm for 12 hours. Cells are trypsinized with Trypsin-EDTA 0.25% in media, counted by automated cell counter (BioRad), and reseeded at 40-50% confluent (16000-20000 cells/cm^2) onto a fibronectin coated gridded coverslip for imaging on a glass slide over 4 hours of induced migration. Cells are then fixed, stained, and imaged. Additionally 2 hours of induced migration will be measured through live cell imaging.

Magnets:

A single and paired N52 NdFeB cube magnet of side length 1 cm will be used to direct migration rotated to 45 degrees to the length of the glass slide. The single cube magnet will be placed within 5 mm of the imaging area resting on the top surface of the glass

slide. The paired cube magnets will be located 5 mm from the imaging area with one resting on top and one below, sandwiching the glass slide and gridded coverslip.

Experimental conditions:

Cells will be influenced by magnetic forces for 48 hours under static fields with a directional shift every 12 hours.

Controls:

Non SPIO treated cells with no magnetic array, non-spio treated cells with magnetic array, SPIO treated cells with no magnetic array.

Repeats: Each experimental condition had three panels analyzed for each distance increment and each iron loading condition. Each experiment was repeated in triplicate with cells between P5-7.

Fluorescent Labels:

SPIOs are conjugated with DiI fluorescent dye (549/564), paxillin-RFP plasmid vector (invitrogen), CellLight Actin-GFP BacMam 2.0 (Life Technologies), Alexa-488 phalloidin.

Equipment and Software:

DeltaVision fluorescent microscope, MATLAB, ImageJ, IgorPro

Measurements:

Cell protrusions were measured by the increase in adherent surface area proximal to the direction of migration from the nuclear axis (perpendicular to the direction of migration). Cell protrusion area was measured over varying distances from the magnetic force proportional to the strength of the magnetic force acting on the cell leading edge therefore quantity protrusion versus magnetic force can be determined. Each protrusion was imaged for quantity and directionality of F-actin polymerization. Quantity of vincullin activation and paxillin expression was also be dye labeled and quantities compared to force acting on the cell body in the formation of protrusions.

Mechanical stress on MSC migratory secretion factors

Cell type and media:

hMSCs (Lonza)

MSC-GM (Lonza) (Basal medium + bullet kit)

Culture Conditions:

Cells seeded at 5000 cells/ cm^2 and grown until monolayer at 80% confluent (32000 cells/cm^2) into 1 well labtekII borosilicate glass chambers (poly-L-lysine coated for 3T3 fibroblasts only). SPIOs delivered at concentration of 100 ug/mL and incubated over cylindrical magnetic array at spacer length of 2.5 mm for 12 hours. Cells are trypsinized with Trypsin-EDTA 0.25% in media, counted by automated cell counter (BioRad). Cells are seeded at 150000 cells/well (~50% confluent) in a 6 well plastic culture plate. Media is changed every 3 days.

Nanoparticle:

Fe_3O_4 (Magnetite) cores nm diameters (synthesized in-house), dspe-PEG 2000 (Me) coated (Avanti polar lipids), coated diameters 40 nm.

Magnetic plate:

Grid array of vertically oriented N42 NdFeB cylindrical magnets of diameter 2.54 mm and height of 25.4 mm.

Experimental conditions:

Cells will be influenced by magnetic forces for 48 hours under static fields with a directional shift every 12 hours.

Controls:

Non SPIO treated cells with no magnetic array, non-spio treated cells with magnetic array, SPIO treated cells with no magnetic array.

Repeats: Each experimental condition had three panels analyzed for each distance increment and each iron loading condition. Each experiment was repeated in triplicate with cells between P5-7.

Dye Labels:

SPIOs are conjugated with DiI fluorescent dye (549/564) to confirm delivery.

Equipment and Software:

DeltaVision fluorescent microscope, ELISA Kits (Abcam), IgorPro, MATLAB

Measurements:

Migratory sectretome in MSC conditioned media (HGF, PDGF, VEGF, SDF-1, TGFβ) will be analyzed by ELISA while under maximum and minimum migratory conditions as established by aim 1.3 and compared to non iron treated control group, and an iron treated control group with no magnet.

Motility of keratinocytes under migratory factors

Cell type:

Adult Normal Human Epidermal Keratinocytes, NHEK (Lonza)

Media:

KGM-Gold (Lonza) + Supplements of HGF, PDGF, VEGF, SDF-1, TGFβ, MSC-GM (Lonza) conditioned after 3 days in culture with hMSC

Culture Conditions:

Keratinocytes are seeded at 6000 cells/cm^2 and grown until monolayer at 80% confluent (38000 cells/cm^2) into 1 well labtekII borosilicate glass chambers. Cells are then trypsinized with Trypsin-EDTA 0.25% in media, counted by automated cell counter (BioRad), and reseeded in a 24 well plastic culture plate (Costar). A scratch is made with a 0.1-1 um pipette tip and rate of closure is measured over 24 hours.

Experimental conditions:

NHEK cell migration will be influenced by chemotaxic factors across physiological concentrations for migration in a scratch assay *in vitro* model over 24 hours. HGF, PDGF, VEGF, SDF-1, and TGFβ will be tested.

Measurements:

Rate of wound (scratched area) closure over 24 hours in 6 hour imaged intervals.

Cell density within wound area at 6 hour intervals

Migration path traces for each cell type

Mean square displacement for 100 individual cells per well per experiment will be determined

Migratory secretome in mixed media

Cell type and media:

hMSCs (Lonza)

MSC-GM (Lonza), KGM-Gold (Lonza), KGM-2 Gold (Lonza), DMEM + 10% FBS + pen/strep/amphotericin B

Culture Conditions:

Cells seeded at 5000 cells/ cm^2 and grown until monolayer at 80% confluent (32000 cells/cm^2) into 1 well labtekII borosilicate glass chambers (poly-L-lysine coated for 3T3 fibroblasts only). SPIOs delivered at concentration of 100 ug/mL and incubated over cylindrical magnetic array at spacer length of 2.5 mm for 12 hours. Cells are trypsinized

with Trypsin-EDTA 0.25% in media, counted by automated cell counter (BioRad). Cells are seeded at 150000 cells/well (~50% confluent) in a 6 well plastic culture plate. Media is changed every 3 days.

Nanoparticle:

Fe_3O_4 (Magnetite) cores nm diameters (synthesized in-house), dspe-PEG 2000 (Me) coated (Avanti polar lipids), coated diameters 40 nm.

Magnetic plate:

Grid array of vertically oriented N42 NdFeB cylindrical magnets of diameter 2.54 mm and height of 25.4 mm.

Experimental conditions:

Cells will be influenced by magnetic forces for 48 hours under static fields with a directional shift every 12 hours. Across a variety of media mixtures each containing a minimum of 50% KGM-Gold or KGM-2-Gold.

Controls:

Non SPIO treated cells with no magnetic array, non-spio treated cells with magnetic array, SPIO treated cells with no magnetic array.

Repeats: Each experimental condition had three panels analyzed for each distance increment and each iron loading condition. Each experiment was repeated in triplicate with cells between P5-7.

Dye Labels:

SPIOs are conjugated with DiI fluorescent dye (549/564) to confirm delivery.

Equipment and Software:

DeltaVision fluorescent microscope, ELISA Kits (Abcam), IgorPro, MATLAB

Measurements:

Migratory sectretome in MSC conditioned media (HGF, PDGF, VEGF, SDF-1, TGFβ) will be analyzed by ELISA while under maximum and minimum migratory conditions compared across varying media mixtures.

CHAPTER 5

DIRECTED MIGRATION OF SUPERPARAMAGNETIC IRONOXIDE NANOPARTICLE LABELED MESENCHYMAL STEM CELLS

Introduction

The internalization of superparamagnetic iron oxide nanoparticles by mesenchymal stem cells when paired with external static magnets produces a magnetic force system that allows for the exertion of a mechanical force on the cell membrane from within the cytosol. Exerting a maximal force on the cell membrane may have measurable effects to cellular migration. In order to determine the effects on cell motility both SPIO delivery optimization and comparative persistent random walking was studied.

Table 5.1. Superparamagnetic Iron Oxide Nanoparticle Characterization

Nanoparticle core size	Hydrodynamic diameter (nm)	Polydispersity (%)	Coating type
15 nm	32.0±1.1	6.3±5.1	DSPE-PEG2000
25 nm	45.6±2.0	9.3±5.2	DSPE-PEG2000
40 nm	57.0±2.0	9.1±1.2	DSPE-PEG5000

The specific parameters for SPIOs used in the subsequent experiments are presented in Table 5.1.

Results

Nanoparticle Delivery

SPIOs were delivered by magnetofection as shown in the delivery schematic in Figure 5.1. 14.7 nm core sized DSPE-PEG-2000 coated SPIOs were incubated with MSCs at a concentration of 100 μg/mL Fe over a magnetic array at varying spacer lengths between the culture well and the magnets for 24 hrs. Cells (P5-P10) were cultured in a single well LabTekII borosilicate glass chamber with seeding density of 150,000 cells/well using MSC-Growth Medium (Lonza). In order to image nanoparticle labeled cells, SPIOs were incubated with DiI for 2 hours and excess dye was removed by ultracentrifugation. A magnetic array comprised of cylindrical magnets (Dia: 2.5 mm, length: 1 cm) arranged in a grid was placed below the cell culture chamber at varying distances ranging from 1 mm – 5.5 mm in 1.5 mm increments. Images were taken with a fluorescent microscope for 25 mm^2 cell area panels and delivery uniformity was determined by image processing with ImageJ and MATLAB. Amount of iron delivered was quantified by ferrozine assay.

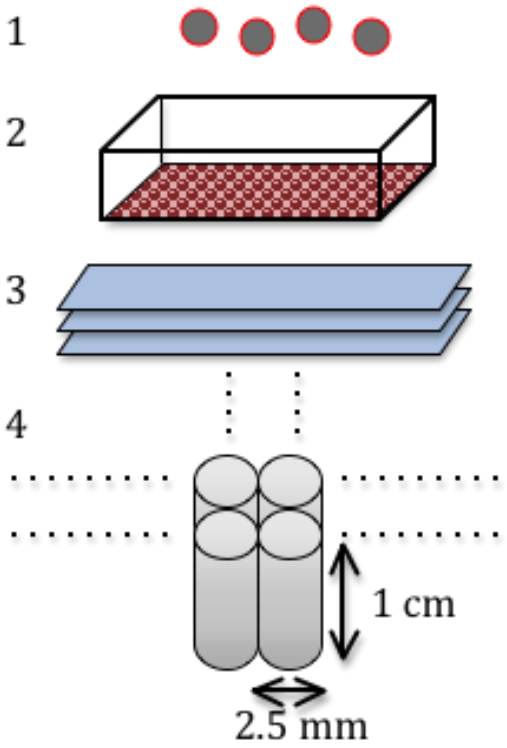

Figure 5.1. Schematic of SPIO delivery into cells by magnetofection. (1) DiI labeled 14.7 nm core-sized SPIOs are incubated with cells seeded in (2) single well borosilicate glass LabTekII chambers. (3) 1.5 mm spacers are used to separate the cell culture chamber from (4) the gridded magnetic array of cylindrical magnets.

The magnetic field gradient for a range of spacer lengths can be visualized using COMSOL Multiphysics software for a 4 grid array of N42 NdFeB cylindrical magnets of dimensions 2.54 mm (Dia) x 1 cm (length) (Indigo Instruments). Figure 5.2 shows the magnetic field gradient as a colormap with their respective scales (in mT) for the spacer lengths of 1, 2.5, 3.5, and 4 mm from the magnetic surface. At a spacer length of 1 mm the highest magnetic field gradient is seen at the junctions between magnets and are calculated as high as 250 mT. Uniformity is determined within the selected area (black square) for each model parameter as it comprises the minimal repeatable unit across a

larger grid of the same design. A spacer length of 2.5 mm or higher produced a uniform gradient for ~75% of the selected region through histogram analysis. But because the magnitude of the magnetic field gradient significantly decreases with increasing spacer length, a spacer length of 2.5 mm is ideal to maintain a gradient of 40 ± 4 mT for 75% of the selected region (Figure 5.2: Top right).

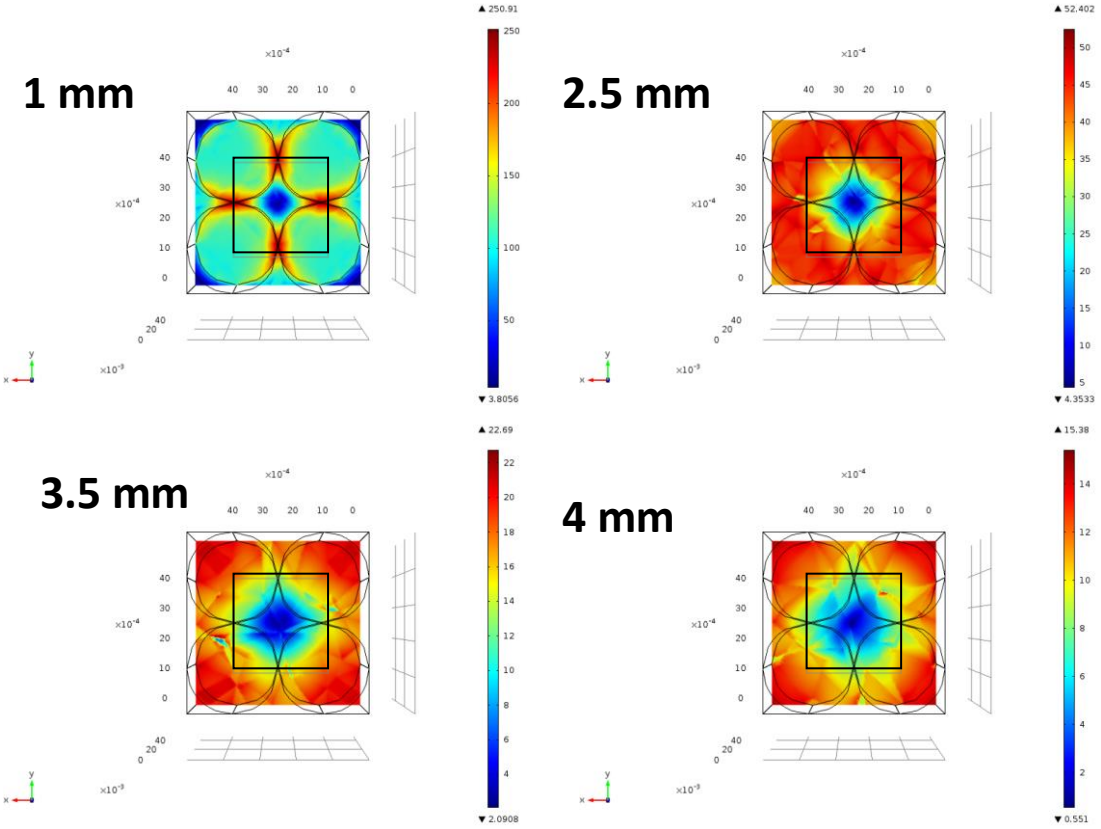

Figure 5.2. **Heatmap of the Magnitude of the Gradient of the Magnetic Field for a Four Grid Array.** Magnetic Field Gradient Colormap at varying spacer lengths reported in mT. Top left: View of x-y plane at a z height of 1 mm from a 2 x 2 cylindrical magnetic grid array of N42 NdFeB magnets, colormap legend max-min: 250 - 3.8 mT. Top right, 2.5 mm: 52.4 - 4.35 mT. Bottom left, 3.5 mm: 22.5 – 2.1 mT. Bottom right, 4mm: 15.4 – 0.55 mT.

Delivery efficiency and cell iron loading for MSCs with 14.7 nm core sized SPIOs is shown in Figure 5.3. Experimentally 82.3 ± 7.2% of cells showed DiI fluorescence from delivered SPIOs within 25 mm^2 area at a magnetic array spacing of 2.5 mm (Figure 5.3 – primary axis) resulting in 4.72 ± 1.10 pg-Fe delivered per cell (Figure 5.3 – secondary axis). Delivery of SPIOs into 3T3 fibroblasts cultured in a poly-L-Lysine coated single well LabTekII borosilicate glass chamber at a seeding density of 200,000 cells/well with a 2.5 mm spacing resulted in similar fluorescence and an iron loading of 1.08 ± 0.77 pg-Fe/cell. Delivery efficiency of 82.3 ± 7.2% is consistent with predicted field uniformity of ~75% from the COMSOL software (Figure 5.2). The difference in iron loading between the MSCs and the fibroblasts can be attributed to the notable difference in cell size. This experiment was repeated three times with each sample in triplicate.

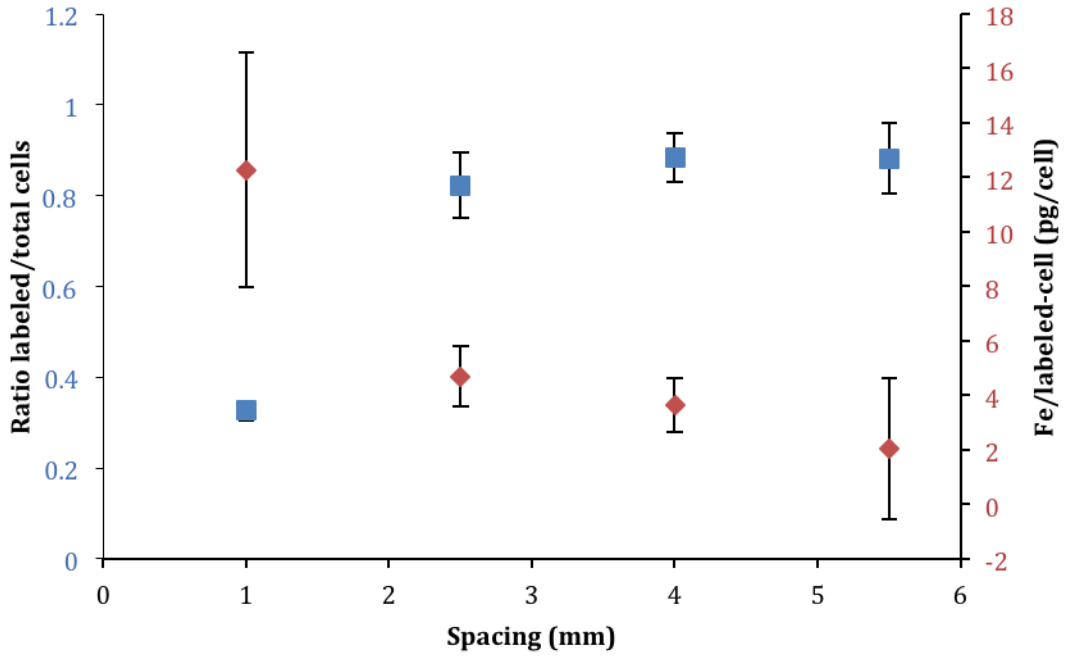

Figure 5.3. Iron Loading and Delivery Efficiency of SPIOs in MSCs. Delivery efficiency and human MSC iron loading for DiI labeled 14.7 nm core size dspe-PEG-2000 coated SPIOs. The fraction of labeled cells after delivery at five distinct spacer lengths between the culture well and the magnetic delivery array is shown with its respective axis (blue, primary axis). The quantity of iron delivered per cell in pg for the same spacer lengths is shown with its respective axis (red, secondary axis). Each sample was prepared in triplicate and experiment repeated three times. Standard error of the mean is reported for each experimental condition (n = 3).

MSC cell viability was measured for three SPIO core sizes (6, 12, 15 nm) and two iron loading incubation concentrations (25 and 100 µg/mL) by MTS assay (Promega). No noticeable loss of viability was found for all conditions when compared to the control (Figure 5.4). MSCs were incubated with SPIOs for 12 hours over a cylindrical magnetic array, media was then changes and viability was measured 36 hours after SPIO delivery.

Data reported is from an experiment repeated in triplicate with triplicate samples per condition.

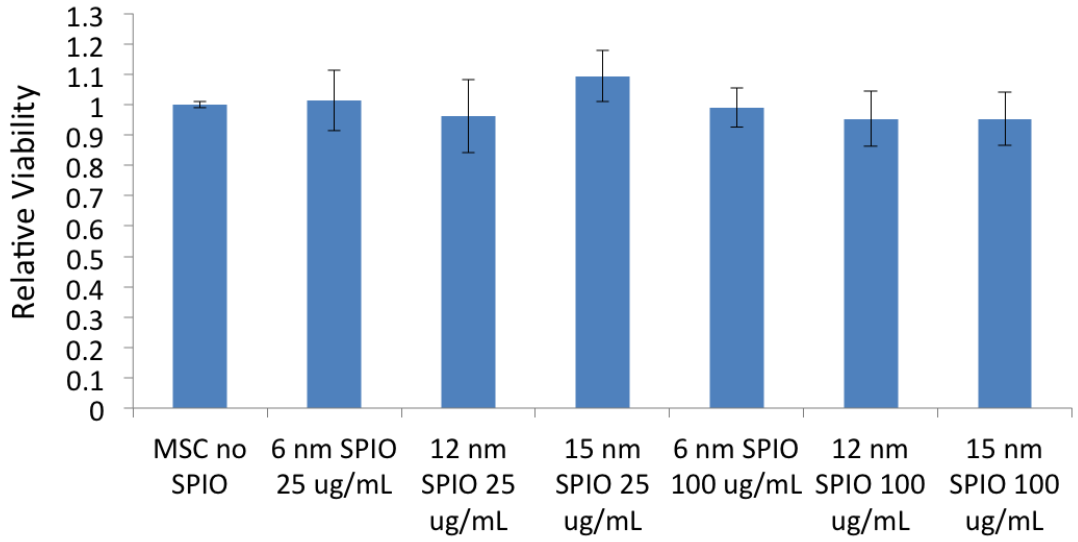

Figure 5.4. MSC Viability after SPIO Delivery. Relative cell viability to a non SPIO labeled control group was measured for three SPIO core sizes (6, 12, 15 nm) and two iron loading incubation concentrations (25 and 100 μg/mL) by MTS assay (Promega) after a 12 hour delivery cycle and 36 hours of additional incubation.

Speed and Persistence

In order to measure cellular migration speed and direction NIH/3T3 Fibroblasts and MSCs were cultured in single well LabTekII borosilicate glass chambers overnight at seeding density of 200,000 cells/well. SPIOs were delivered at an iron concentration of 100 μg/mL over 24 hours on an array of 2.5 mm diameter x 1 cm length cylindrical NdFeB magnets with a 2.5 mm spacer. The migration model consisted of a monolayer of SPIO-labeled cells over a single bar magnet with a static magnetic field acting on the cell sample. Figure 5.5 shows the experimental setup for the speed and persistence study

(Figure 5.5, A), the direction of the magnetic field lines highlighting x-y and z directional forces affecting both adhesions and protrusions (Figure 5.5, B), and the magnitude of the magnetic field gradient at the surface of the culture slide (Figure 5.5, C). The cell nuclei were stained with Hoescht dye and the whole cell body with calceinAM and tracked in panels of at least 100 cells/panel for 2 hrs in 10-minute intervals. DMEM + 10% FBS Media and MSCGM was supplemented with 25 mM HEPES buffer and temperature was maintained at 37°C with a custom temperature regulator on the DeltaVision fluorescent microscope. Migration speed was measured for each cell by measuring absolute displacement of the centroid of the nucleus in μm in the direction of the magnetic field divided by the total time in minutes. The direction of cell migration was measured by persistence, defined as the directed displacement (compared to magnetic field line trace) over the total displacement.

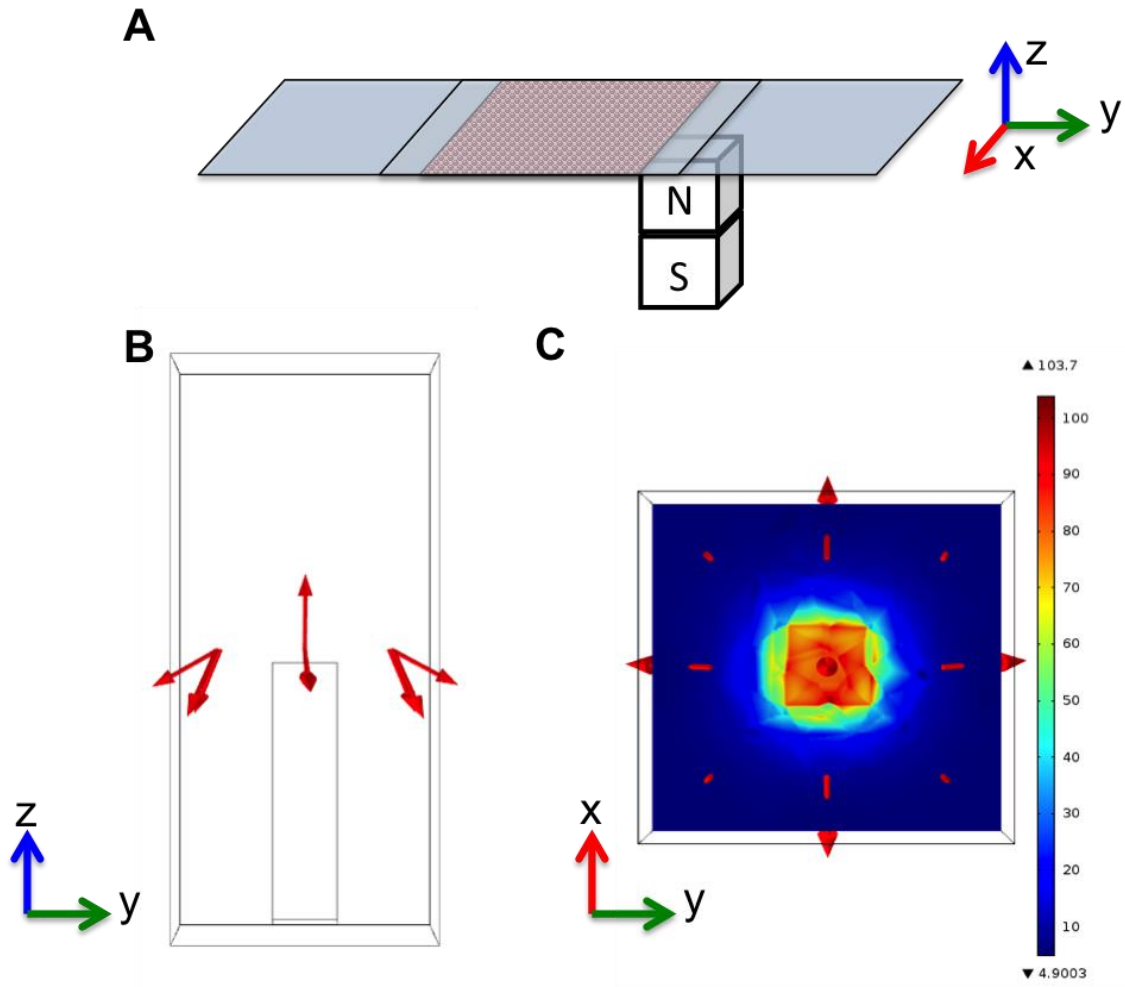

Figure 5.5. Speed and Persistence Schematic. Magnet placement on culture slide for the speed and persistence studies (A), the direction of the magnetic field lines highlighting x-y and z directional forces theoretically affecting both cell adhesions and protrusions (B), and the magnitude of the magnetic field gradient at the surface of the culture slide (C).

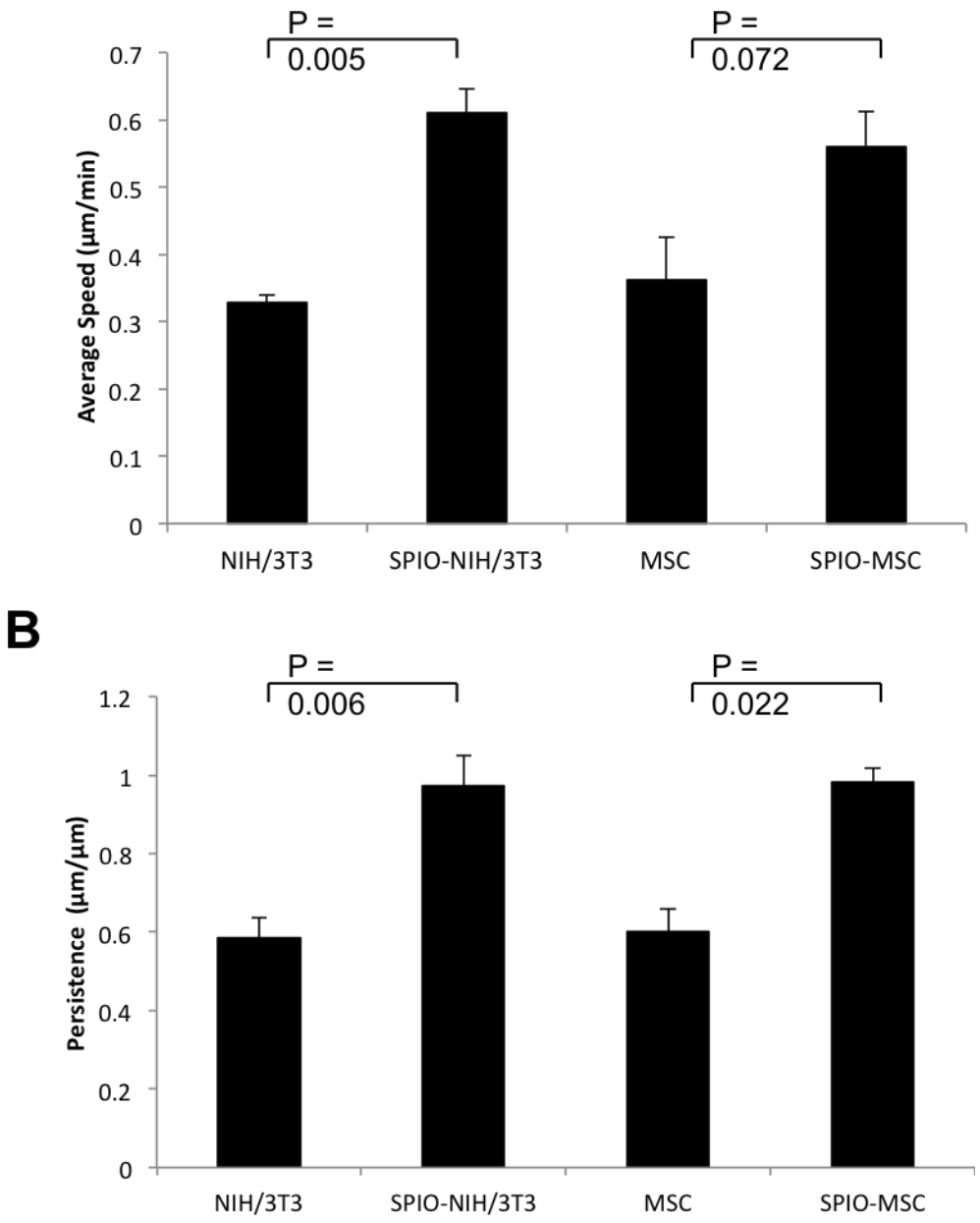

Figure 5.6. MSC and NIH/3T3 Cell Motility Speed and Persistence. Average speed (A) and persistence (B) reported with standard error of the mean for NIH/3T3 murine fibroblasts and human MSCs with and without internalized SPIOs after 2 hrs. of directed motility at 37°C.

Average speed and persistence of both labeled and unlabeled murine fibroblasts and human MSCs are shown in Figure 5.6. SPIO labeled murine fibroblasts showed high significance for both speed ($p = 0.005$) and persistence ($p = 0.006$) with an average speed and persistence of 0.611 μm/min (1.86-fold difference from the control) and 0.974 (1.66-fold diff.) respectively. SPIO labeled MSCs showed a noticeably increased speed of 0.561 μm/min (1.55-fold diff.) although not statistical significant ($p = 0.074$). SPIO labeled MSCs showed statistical significance ($p = 0.022$) in persistent motility with a persistence value of 0.984.

Comparative Model for Persistent Random Walk

In order to better determine the strength of persistent directional control the magnetic force has on cell walking, a comparative model was used. 76 μm-thick fibronectin track coated coverslips were used as a positive persistent random walking control where the physical space constraint drives cells to maintain a high level of persistent walking across a cell seeding density gradient. Figure 5.7 displays the four experimental conditions including with and without SPIO labeling, with and without the use of external magnet, and with and without the use of tracks. All surfaces are fibronectin coated to control for surface dependent variations in motile behavior. Centroid based displacement was tracked by hoescht staining the cell nucleus for 84-100 cells per slide over a 200 minute period at 10 minute time intervals. Cell trajectories, mean square displacement, directionality, and autocorrelation were plotted with the help of Gorilek & Gautreau's DiPer (directional persistence) computer program from Liebniz University [52].

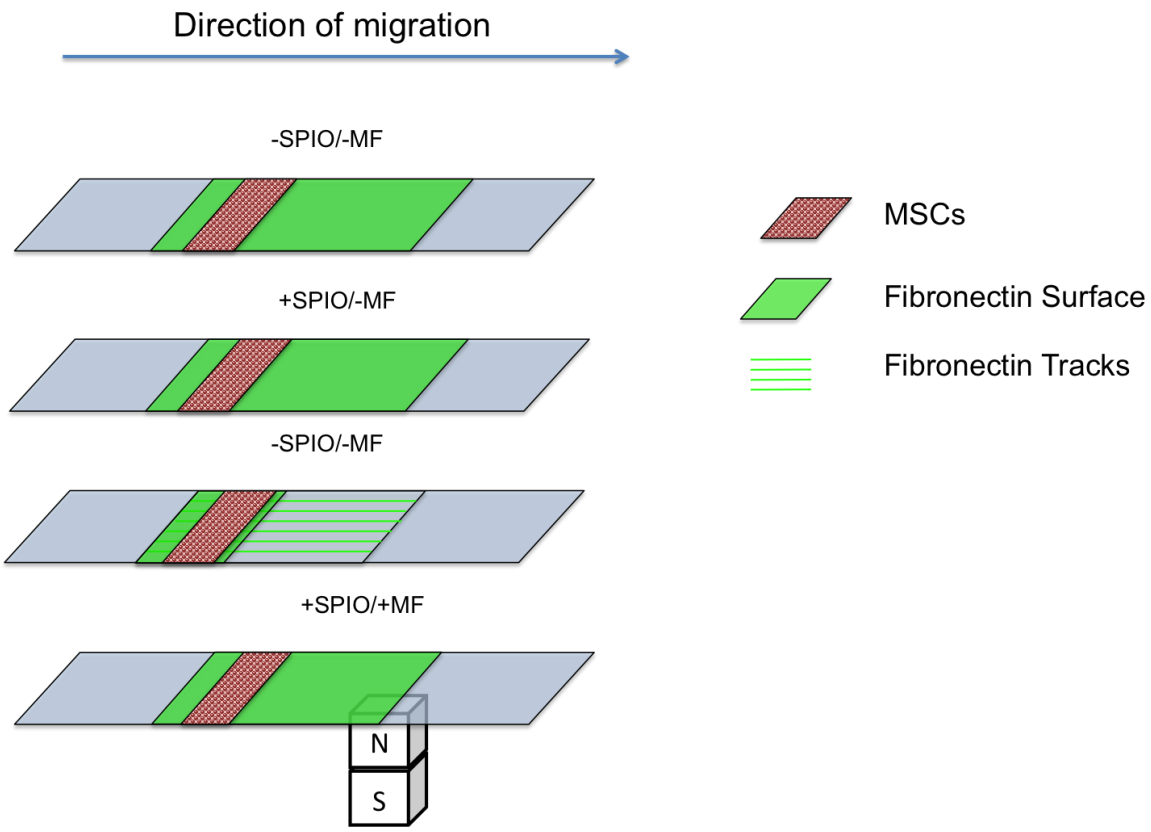

Figure 5.7. Comparative Persistent Random Walk Schematic of Experimental Conditions. Four cell treatment conditions were seeded onto fibronectin-coated coverslips containing either a planar surface or space confined tracks. A single N42 bar magnet was used to maintain a directional force on the SPIO labeled cells.

Figure 5.8 shows cell trajectories for 20 representative cells for each condition. All four conditions show a rightward bias indicating an overall rightward directionality due to decreasing cell density in the same direction. Semi random motion is seen for –SPIO and +SPIO labeled negative controls where highly directional motion is seen for both cells confined to tracks and cells that were magnetically driven. Mean squared displacement was plotted as the average for the complete cell population tracked and plotted across each 10 minute interval for a total of 200 minutes (Figure 5.9). No

significant difference can be shown across the conditions without an experienced magnetic force indicating that the difference between fibronectin coating in the form of tracks or as a plane has no effect on average displacement whereas an experienced force has a major effect on overall displacement over the same time period (Figure 5.9). The +SPIO/+MF condition also exhibits a nonlinear trend indicating an increase in speed over the given time period (Figure 5.9-right panel-green).

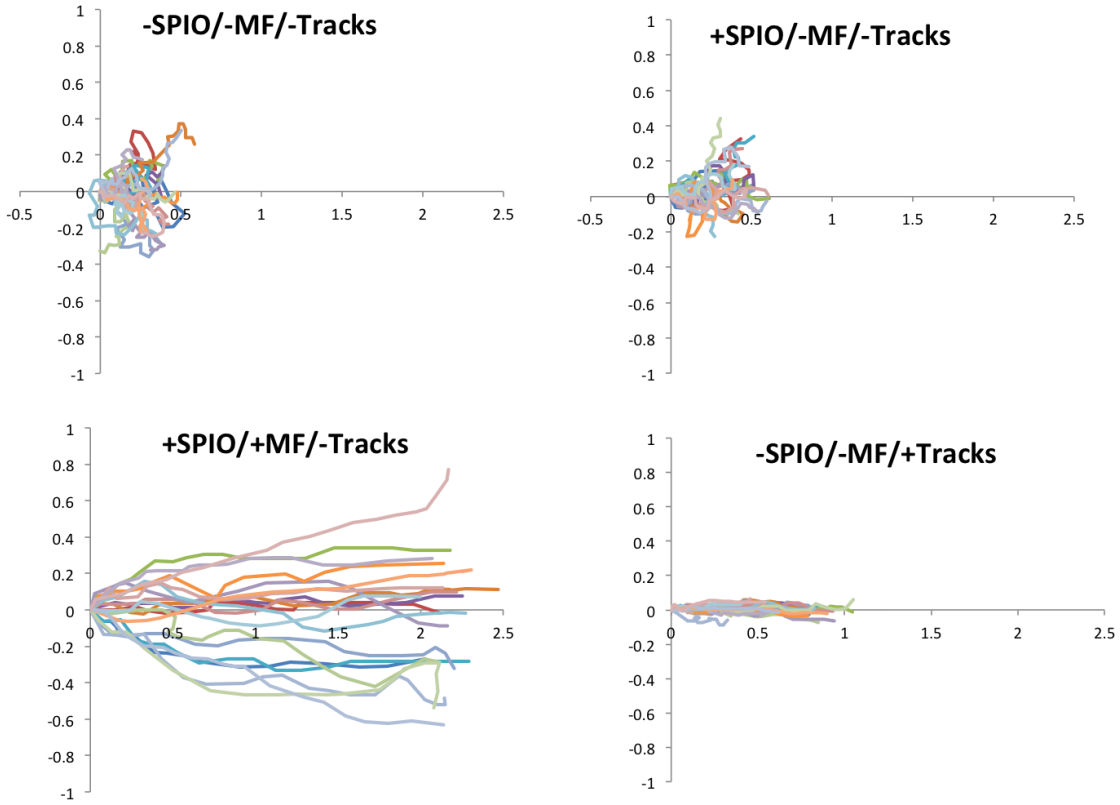

Figure 5.8. Cell Trajectories of Comparative Persistent Random Walking. Four conditions were tracked for a minimum of 84 cells per population over 200 minutes. Shown are 20 randomly selected cell trajectories representative of the whole.

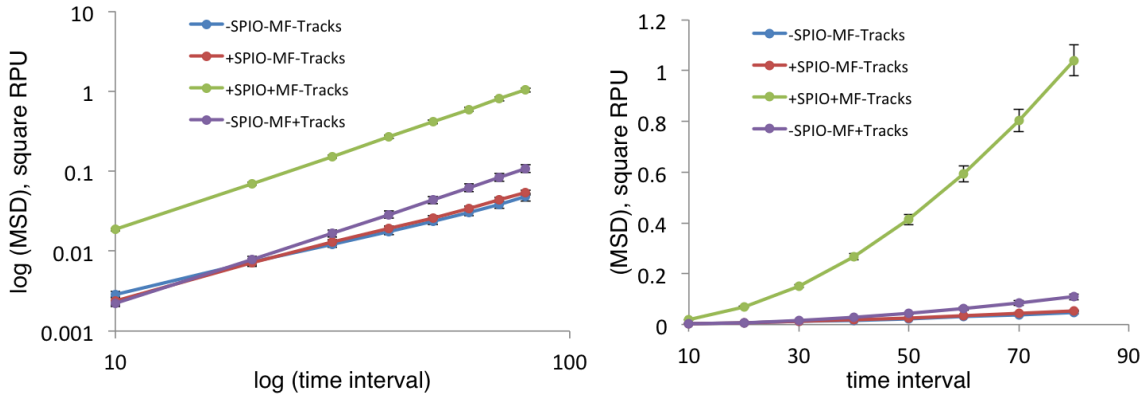

Figure 5.9. MSD of Comparative Persistent Random Walking. Figure shows the MSD for the four measured conditions in linear (right) and logarithmic (left) axes.

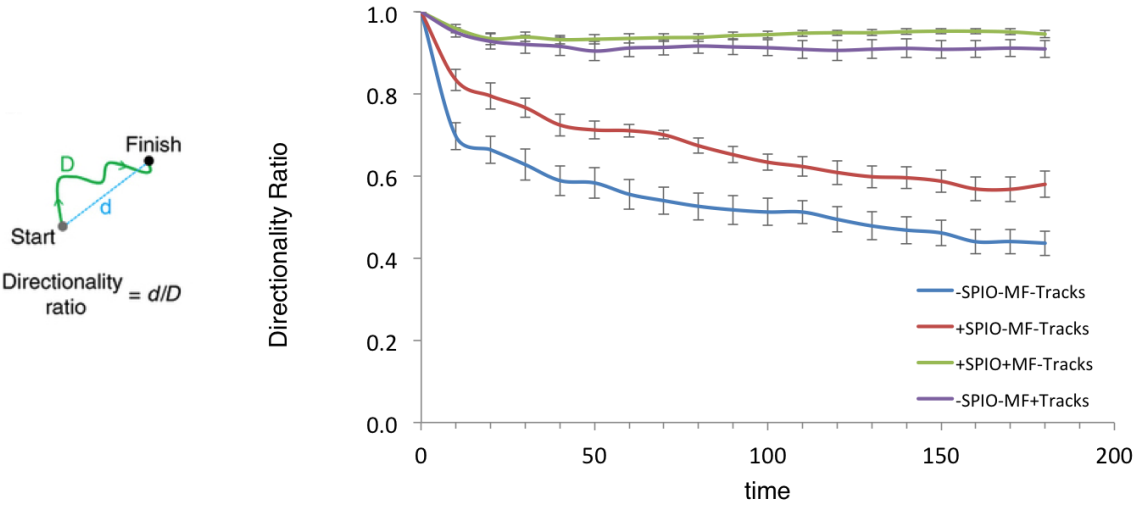

Figure 5.10. Directionality Ratio of Comparative PRW Model

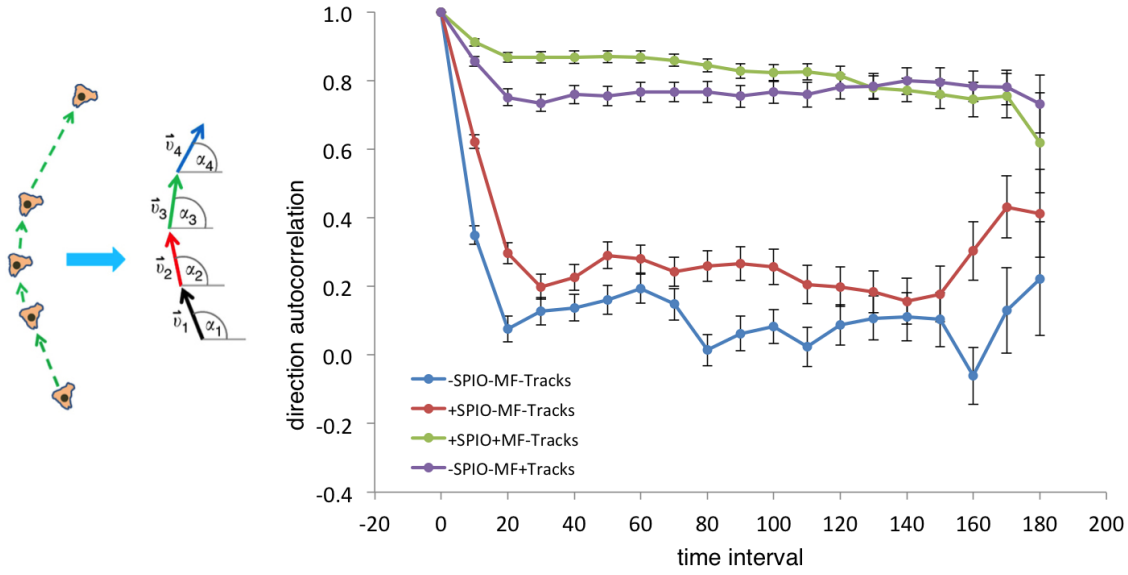

Figure 5.11. Autocorrelation for Comparative PRW Model

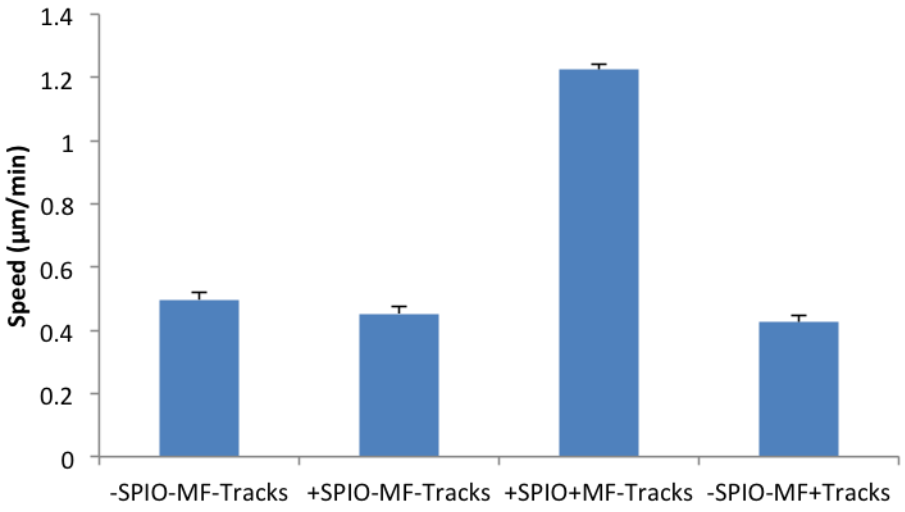

Figure 5.12. Average Speed of MSCs During PRW Model

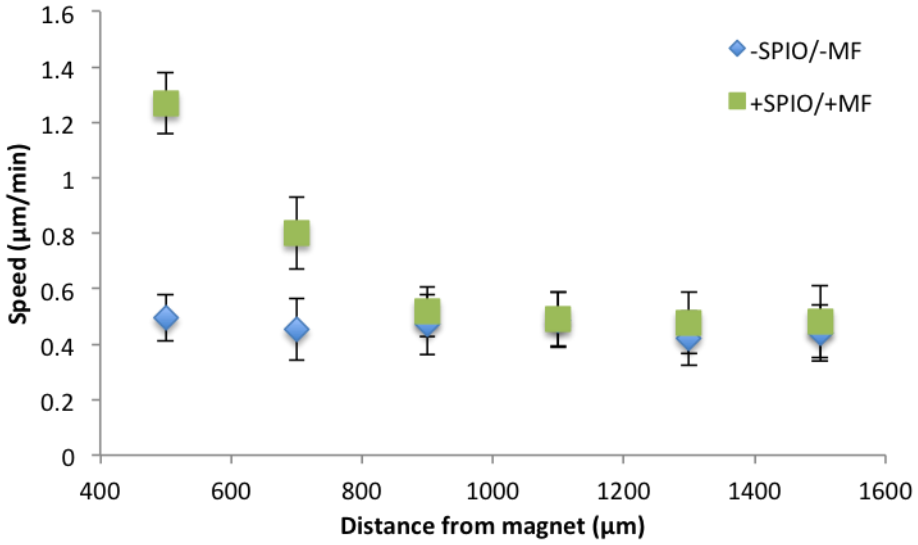

Figure 5.13. Average Speed of MSCs vs. Distance from Magnet

Directionality ratio (Figure 5.10) and autocorrelation (Figure 5.11) are two distinct methods for measuring persistence. Directionality ratio is a measure of the final displacement of the centroid from its location at time = 0 to time = 200 minutes over the total distance traveled on a per cell basis. A directionality ratio of 1 indicates a perfectly straight trajectory from the initial to final centroid location. Autocorrelation is a measure of the average angular change from time point to time point and reported as the cosine of the angular change per interval. An autocorrelation value of 1 indicates a cosine of zero angular change from the previous motion. SPIO labeling alone shows a slight increase in directionality and autocorrelation but no significance across all time points (Figure 5.10). The use of tracks, as expected, shows a near 0.91 directionality ratio for all time points indicating a consistently high level of persistent motion (Figure 5.10-purple). Similarly, the +SPIO/+MF condition exhibits a higher average directionality at a ratio of 0.95

(Figure 5.10-green). Both the magnetic force and tracked conditions significantly exhibit persistence when compared to the –SPIO/-MF negative control.

Autocorrelation shows a similar result with the +Tracks and +SPIO/+MF conditions having a significantly higher angular persistence over the same time period (Figure 5.11-green and purple). Average speed was calculated over the 19 intervals for the four conditions. The magnetic force experienced by the SPIO labeled cells attracted to the gradient magnetic field produced by the N42 static magnet enhanced average speed by over 2.7x over the negative control (Figure 5.12). This speed result is distance dependent, seen in Figure 5.13 where 20 cells where monitored at varying distances from the magnet surface. A substantial drop in speed is noticed and no significant speed increase (when compared to the negative control) was observed at distances greater than 700 μm (Figure 5.13).

Discussion

Multiple changes to motility were demonstrated with the use of a magnetically driven force on the cell body. Primarily, an overall enhanced average speed was demonstrated on both a non-specific (PLL) and specific (fibronectin) surface coating when SPIO labeled cells were exposed to a magnetic force. SPIO labeled cells can be directed to migrate toward a high magnetic field gradient (50-180 mT) at speeds comparable to previously reported galvanotaxic and chemotaxic speeds ranging from 0.5-0.7 μm/min with a high degree of persistence [53-55]. A high level of controlled motility through magnetism *in vitro* has potential for 3D and tissue culture studies due to the consistency of magnetic fields through various mediums. In order to better understand the

mechanism of directed migration, adhesion and protrusion effects must be studied independently. Additionally, this force induction model allows for a unique internal mechanical stress on the cell membrane and is applicable to a number of biophysical and biochemical response studies. In the case of the +SPIO/+MF condition and the –SPIO/-MF negative control, a 145% maximum increase in average speed was demonstrated on fibronectin coated surfaces (Figure 5.12). This increase in average speed is highly dependent on the experienced magnetic force on the cell that is a function of the gradient of the magnetic field produced by the static magnet that is in turn a function of the strength and distance of the magnet from the cells within the region of interest. When this distance is greater than 700 μm for the N42, NdFeB magnet used in this study, no significant increase in average speed is observed (Figure 5.13).

Additionally, the +SPIO/+MF condition expressed strong directionality and persistence. Migration occurred in the direction of the magnetic field, towards the point of the greatest gradient of the magnetic field of the static magnet confirmed by comparison to the modeled gradient heat map of the N42, NdFeB magnet. Although, in this study, all conditions had a rightward bias due to a graded cell density across the fibronectin coated coverslips (Figure 5.8). Because of this overall bias, no absolute claim can be made regarding magnetic directionality in the +SPIO/+MF condition unless these two systems for directional control can be decoupled. Regardless, a strong correlation was seen for cell trajectories along magnetic field lines in the +SPIO/+MF experimental condition.

Persistence for both of the –SPIO/-MF/+Tracks and the +SPIO/+MF conditions held at above 90% throughout the duration of the study for the two methods of

persistence quantification (directionality ratio and autocorrelation) (Figures 5.10, 5.11). This indicated that the magnetically driven motile cells performed at a similar level positive control of size-constrained fibronectin tracks in both displacement-based persistent cell walking and point-to-point angular change.

Conclusion

This study demonstrated the overall changes to motile behavior for SPIO labeling and the introduction of a magnetic force on the cell body. SPIO labeling can be accomplished through magnetofection with iron loading quantities on average of 4.72 pg/cell with a delivery efficiency of 82% for human mesenchymal stem cells with no observable loss in viability. SPIO labeling alone did not contribute changes in average speed, directionality, or persistence for a fibronectin coated persistent random walk motility model. Magnetically directed cells, on the other hand, did exhibit a substantial increase in average speed (although dependent on distance from the magnet) with directional persistence comparable to that measured for a size-constrained positive persistence control group. Overall, the force experienced by MSC caused by internally delivered SPIOs and controlled by an external magnet is sufficient to cause measureable changes to directionally persistent cell motility.

CHAPTER 6

CELLULAR RESPONSE TO MAGNETIC FORCE LOADING

Introduction

The mechanical force experienced by an individual cell using internalized SPIOs and an external static magnet is a complex three-dimensional distributed force on the cell membrane made up of the accumulated effect of the attractive force on each SPIO nanoparticle producing a summed tension on the cell body [13, 56]. A more simple approach to understanding this tensile force on the cell body is to assume a net resultant point force in the direction of the magnetic field. The net sum of each nanoparticle's force contribution would result in a single point force (as an overestimation of the real force over a distributed area) [57].

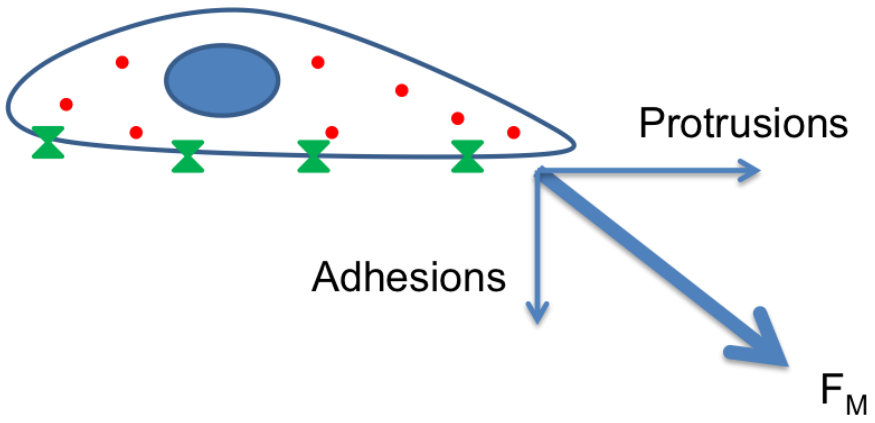

Figure 6.1. Resultant Force and Directional Components of SPIO-MSCs. This resultant force would contribute to cell body deformations (if able to overcome cytoskeletal tension response forces) directly influencing both adhesions and protrusions. Z-component of the net magnetic force on the cell would likely contribute to adhesion

effects and the x,y-components of the net magnetic force would likely contribute to protrusion and lamelipodia-like extensions of the cell body. In order to attempt to decouple these two distinct contributions, two unique magnet arrangements were used to study resulting effects of magnetic force on MSC protrusions, adhesions, cytoskeletal response, and cell shape response.

Results

Protrusions

In order to measure directed migration in the absence of additional adhesive forces caused by magnetic attraction in the z-direction, MSC were seeded onto a poly-L-Lysine coated coverslip, placed on a glass slide and induced to migrate by paired magnets oriented to minimize z directional forces on the cells. Two rectangular (0.5 x 0.5 x 1 cm) N52 NdFeB magnets were used to sandwich the glass slide and coverslip. Figure 6.2 shows the experimental setup for all following protrusion/extension (Figure 6.2, A), the direction of the magnetic field lines highlighting the absence of a z directional force (Figure 6.2, B), and the magnitude of the magnetic field gradient at the surface of the culture slide (Figure 6.2, C).

Mean square displacement for 100 cells were tracked and measured over a 2 hour time period in 10 minute intervals. The experiment was repeated three times with 100 cells tracked per experiment. Figure 6.3, A shows the experimental data for migrating cells over 2 hours with only magnetic effects to cell protrusion. Figure 6.3, B shows the internal relocation of SPIOs during the first 40 minutes (time period highlighted in gray in Figure 6.3, A).

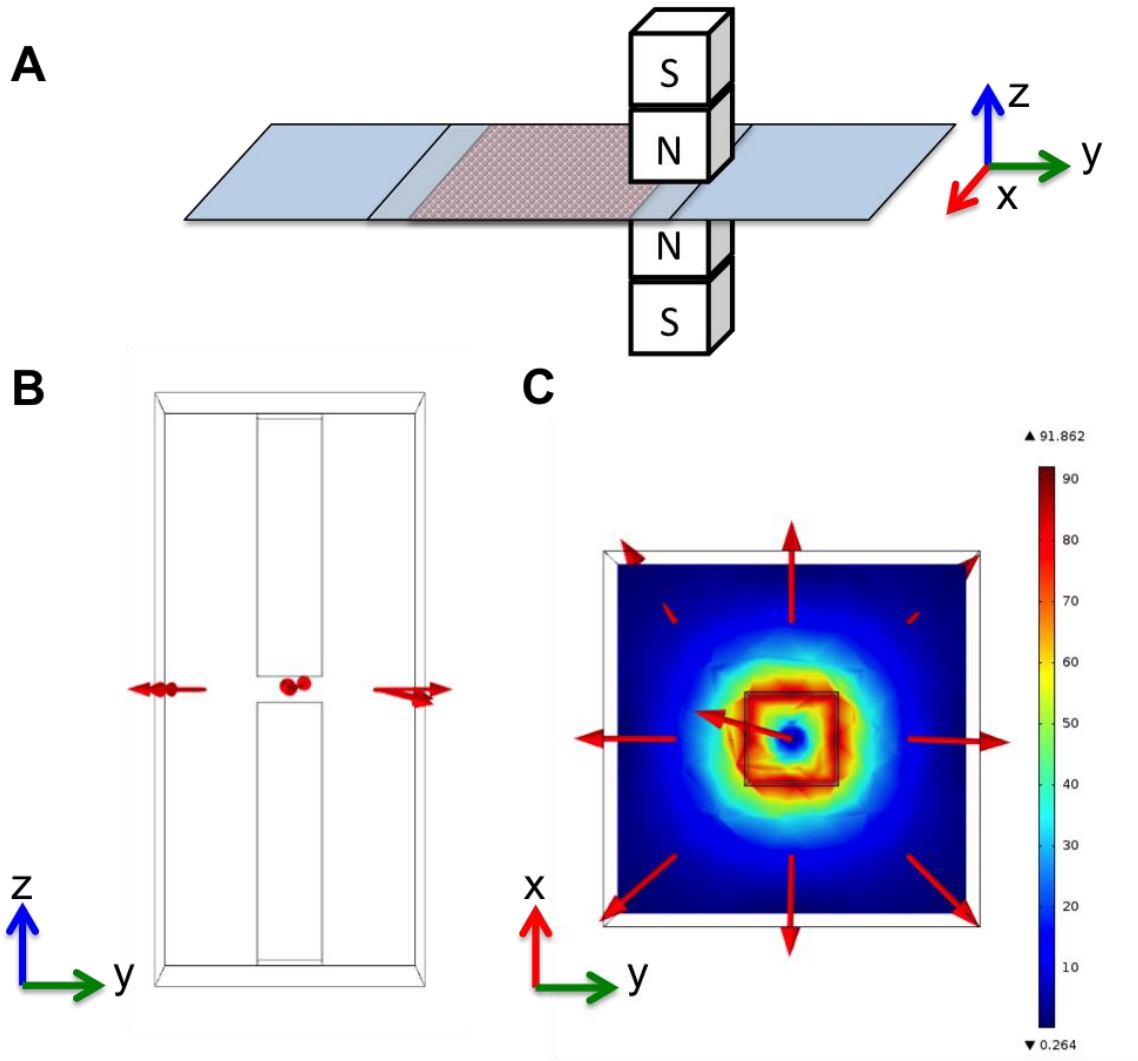

Figure 6.2. **MSC Protrusion Schematic**. Protrusion in the absence of added adhesion study: magnet properties and setup. The experimental setup for all following protrusion/extension (A), the direction of the magnetic field lines highlighting the absence of a z directional force (B), and the magnitude of the magnetic field gradient at the surface of the culture slide in mT (C).

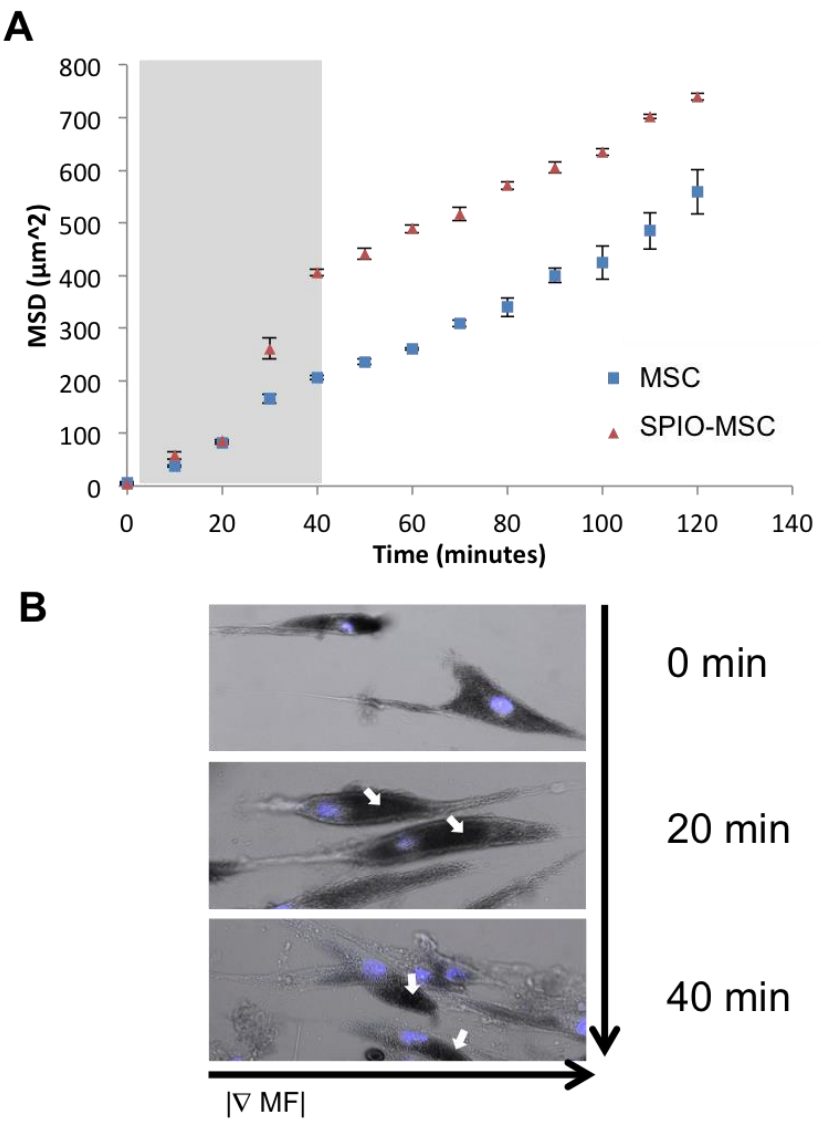

Figure 6.3. MSD for MSCs and SPIO-MSCs under x-y Component Force. Experimental data of protrusion/extension study. Mean square displacement over 2 hrs. for MSCs with and without SPIO labeling was recorded for 100 cells per sample with each experimental condition repeated in triplicate (A); region in gray highlights first step of directed migration by manipulation of protrusions alone. Visual of SPIO relocation in the MSC cytosol during the first 40 minutes of directed protrusion (B); corresponds to the gray subsection of subfigure A.

Directed protrusions resulted in the unexpected finding of a stepwise response as seen in Figure 6.3, A. SPIO labeled cells exhibit a non-linear response to magnetically directed protrusion formation within the first 40 minutes, resulting in a substantial increase in speed during SPIO relocation (polarization toward the direction of migration). The specific cytosolic relocation of internalized SPIOs can be seen in Figure 6.3, B (white arrows). The major difference in displacement before and after the first 40 minutes must be analyzed independently and highlights an interesting feature not noticed during the comparative motility study. Relocalization of the SPIOs during the early phase of motility contributes to an increase in MSD. Once SPIO polarization within the cell body is completed, it is maintained throughout the rest of the study and MSD increases at a linear rate comparable to the non-SPIO control group. This indicated protrusion driven migration does not increase migration speed in steady state but might contribute to motile directional persistence. Additionally, considering the speed effect during polarization and artificial protrusion creation within the first 40 min., nascent adhesions are likely to be the contributing factor in increasing migration speed where protrusion directed migration likely contributes to directionality and persistence.

Adhesions

In order to understand the enhanced adhesion effects of SPIO labeled cells when under a uniform magnetic field, three adhesion effects were measured. The rate of attachment, rate of cell spreading, and strength of adhesions were compared to non-labeled and labeled cell controls. SPIO labeled cells were seeded on borosilicate glass single well LabTekII chambers and placed over the cylindrical magnetic array described

and shown in Figures 5.5 at a spacer length of 2.5 mm to produce a pseudo uniform z directional force on the cells in culture for 16 hours. The attached cell area was measured from live cell images at numerous time points on ImageJ for 50 cells per sample well. (1) MSCs are first labeled with SPIOs as previously detailed in single well LabTekII borosilicate glass plates, trypsinized and seeded onto (2) poly-L-Lysine coated 96 well plates in quadruplicate for varying time points from 0-12 hours, the plate is always left on a large magnetic grid array producing a pseudo-uniform –z directional force, (3) the plates are calcinAM stained and centrifuged upside down at a known RCF/RPM for 5 minutes. Fluorescence of calceinAM from viable cells is measured before and after spin.

Before the study could be done, an appropriate spin speed had to be determined to notice a difference in adherence rate and strength. MSCs were seeded onto 96 well plates and spun at 8 different speeds varying from 300-3000 RPMs to measure adherence ratio after 6,12, 18 and 24 hours of incubation. The specific speeds used with the known rotor length could be converted to RCF values and then to a specific detachment force experienced on a per cell basis. 99 pN/cell was determined to detach 50% of cells after 12 hours of incubation seen in Figure 6.4. Serving as the ideal midpoint for subsequent spins to observe measurable deviations from the control.

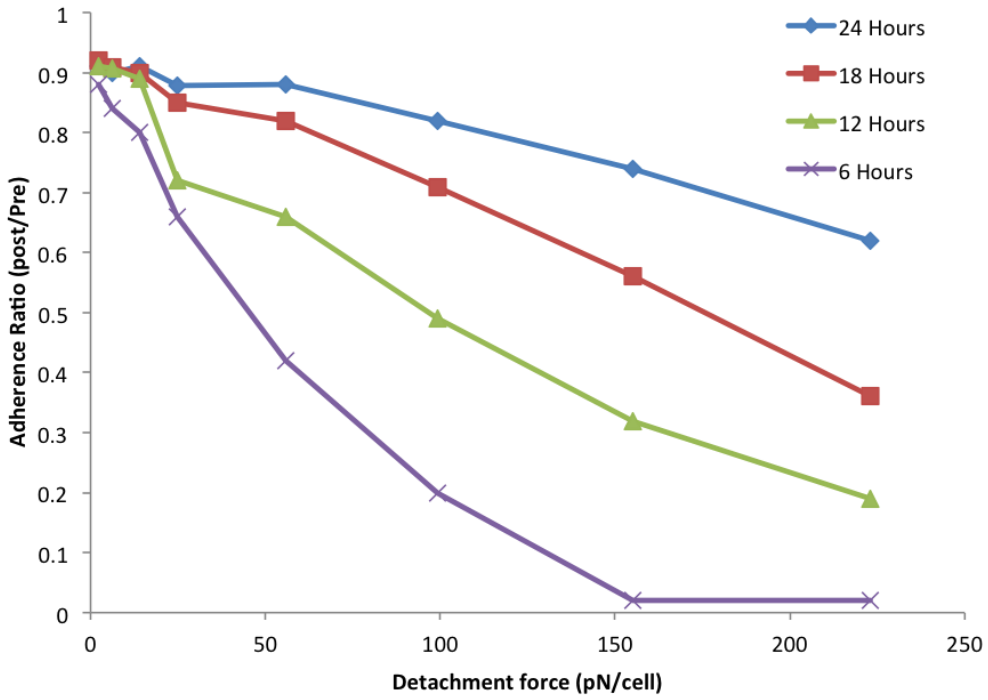

Figure 6.4. Adherence Ratio of MSCs for Varying Incubation Times and Centrifugal Detachment Forces. Data above represents varying cell adherence strength as measured by adherence ratio after centrifugal detachment for optimization of incubation time and spin speed for unlabeled MSCs. Detachment force is directly related to spin speeds ranging from 300-3000 RPMs.

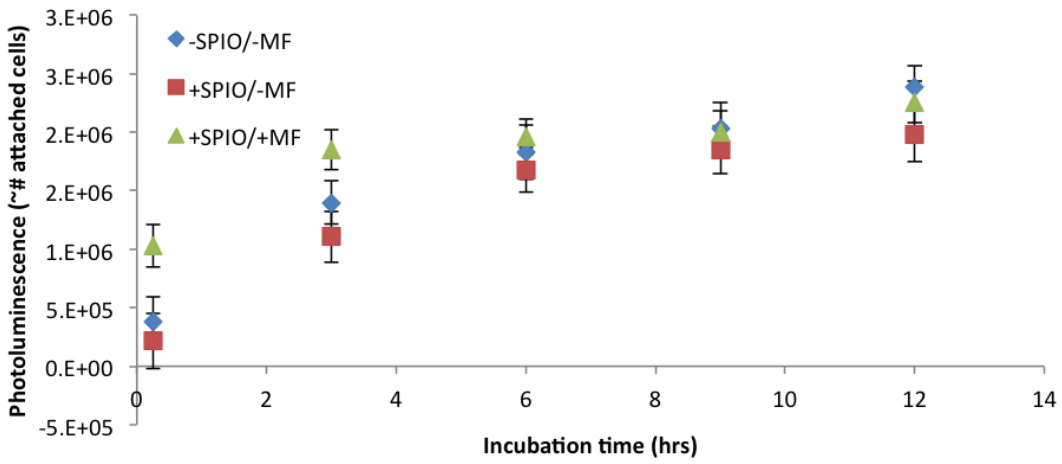

Figure 6.5. Cell Attachment Rate for MSCs and SPIO-MSCs. Date represents cell attachment rate over a total of a 12 hour incubation time at 3 hour increments for three cell treatment conditions, -SPIO/-MF, +SPIO/-MF, and +SPIO/+MF.

The overall rate of attachment for the three culture conditions do not widely differ and no significance is seen after the 3 hour incubation time point (Figure 6.5). However, at the 15 minute and 3 hour time point the SPIO labeled cells, which experienced a magnetic force, showed significant enhanced levels of cell attachment (Figure 6.5-green).

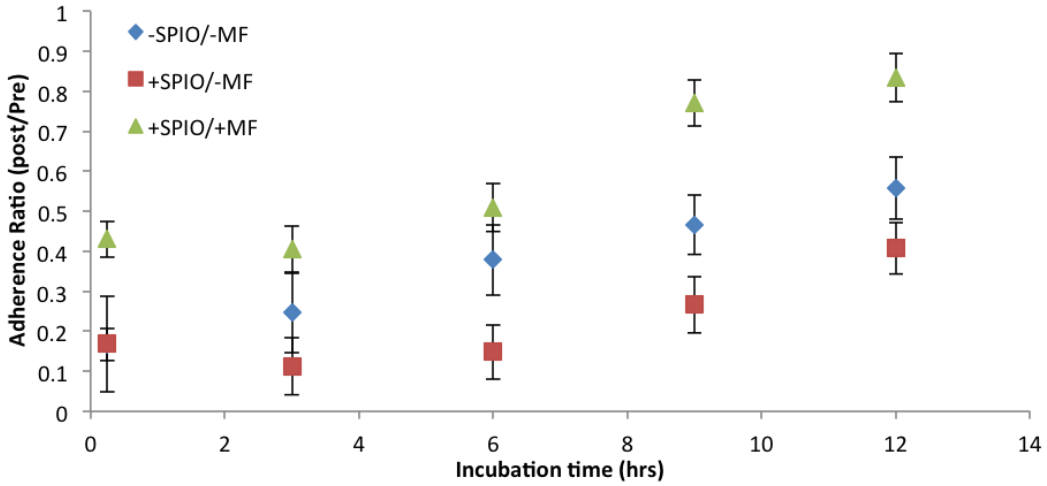

Figure 6.6. Adherence Ratio for MSCs and SPIO-MSCs. Date represents a measure of the strength of cell adhesion for a bulk population after experiencing a centrifugal detachment force of 99 pN/cell for 5 minutes.

In Figure 6.6 data is reported as a percent of cells that remained attached after experiencing the aforementioned detachment force. When compared to the –SPIO/-MF negative control, SPIO labeling alone (+SPIO/-MF) consistently showed lower adherence ratios for all time points above 15 minutes of incubation. The greatest difference of the means, -0.2, is noticed at the 6-hour incubation time point. The +SPIO/+MF condition, on the other hand, consistently exhibited a higher adherence ratio when compared to the –SPIO/-MF negative control for all time points with the greatest difference of the means, 0.31, at the 9-hour incubation time point.

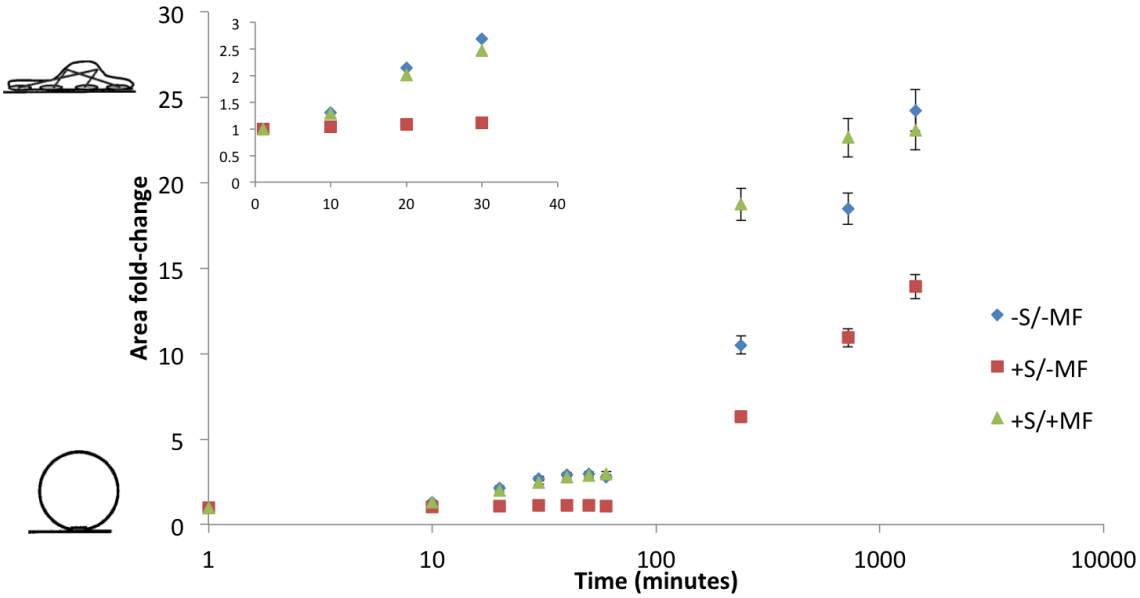

Figure 6.7. Cell Spreading. Cell Spreading reported as area fold change over 24 hours.

In order to better understand this difference in adherence ratio attached cell area was measured over the same time period for the same experimental conditions. Figure [] shows the rate of cell spreading as a percent of area-fold change from the suspended spherical cells at time point 0 minutes. Similarly, the rate of cell spreading for the three conditions follow the trend of cell adherence ratio where the SPIO labeled cells without a magnetic field (+SPIO/-MF) presented a lower cell spreading rate than the –SPIO/-MF negative control and the +SPIO/+MF condition presenting a higher cell spreading rate up until the 240 minute (4 hour) time point when the spreading rate levels off and plateaus by the 720 minute (12 hour) time point (Figure 6.7-green). After 24 hours, after maximum cell spreading has been reached, the average cell area for the three conditions vary such that the SPIO labeled cells that did not experience magnetically assisted spreading only reached a maximum cell area 61% of both the negative control and the magnetically assisted spread cell groups (Figure 6.7-end points).

Cell Stiffness

In order to gain some understanding on effective changed to cell stiffness before and after SPIO labeling, the Young's modulus for four cell conditions was measured using atomic force microscopy. Young's modulus in kPa for four total conditions was measured at various SPIO core sizes. A minimum of 24 cells was measured for each population. SPIO labeling showed highly significant increase in cell stiffness with means of 5.24 ± 1.06 kPa for the 15 nm cores ($p = 0.005$), 5.66 ± 1.60 kPa for the 25 nm cores ($p = 0.018$), 8.16 ± 1.71 kPa for the 40 nm cores ($p = 0.001$). The unlabeled negative control reported a mean Young's modulus of 1.19 ± 0.44 kPa consistent with reported literature values of 0.70 - 2.1 kPa [58].

Cytoskeletal Response

Cell images were taken after immunohistochemistry staining for F-actin, Vinculin, β1-Integrin, and α-Tubulin. Cell nuclei were Hoescht stained and SPIOs were DiI (lipid burying dye) labeled for fluorescent imaging. Figures [] and [] show representative panel images for the five colors imaged. The imaging experiments were split into two grouping of 4 colors each in order to minimize fluorescent color overlap. The first group included: F-actin, Vinculin, DiI-SPIO, Hoescht-nuclei. The second group included: α-Tubulin, β1-Integrin, DiI-SPIO, Hoescht-nuclei. Signal distribution for each grouping was plotted across both the length and the width of each cell, averaged as a percent of each length for a total of 24 cells for each of the three experimental conditions and plotted in Figure 6.8. Length and width cross-sections were determined by a custom ImageJ macro protocol outlining cell area, determining nuclear centroid location and

delineating cell length as the longest distance bisection of the cell area that passes through the nuclear centroid. Width was determined by DiI signal intensity selection of as the central quarter section of each the fore and aft length segment from the nuclear centroid. Numerous observations were made for each of the cytoskeletal and adhesion responses to SPIO labeling and magnetic force loading.

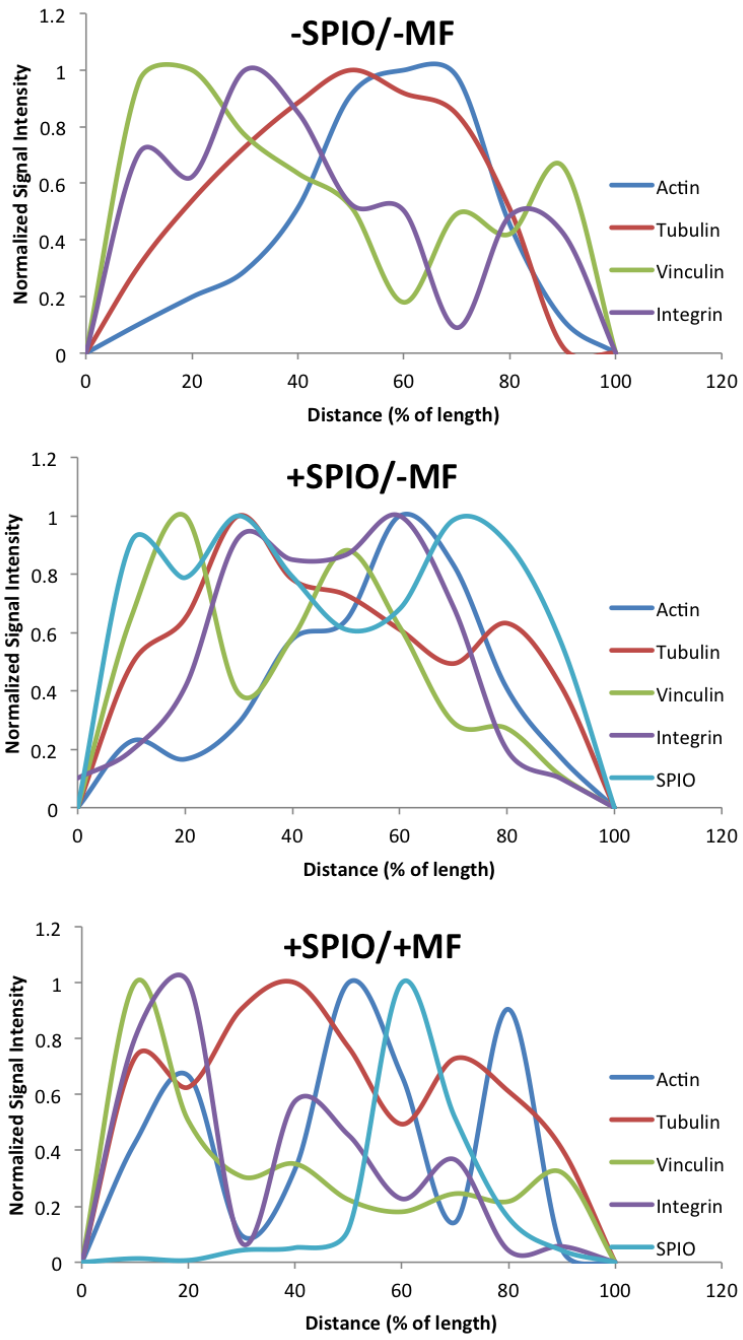

Figure 6.8. Immunofluorochemistry Signal Distribution Across Cell Length. Signal distribution across the length of MSCs for three cell conditions, -SPIO/-MF, +SPIO/-MF, +SPIO/+MF. Actin, α-Tubulin, Vinculin, β1-Integrin, and DiI-SPIO signal is reported for

each condition respectively. All signal intensity is background subtracted and normalized to each colors' respective maximum intensity.

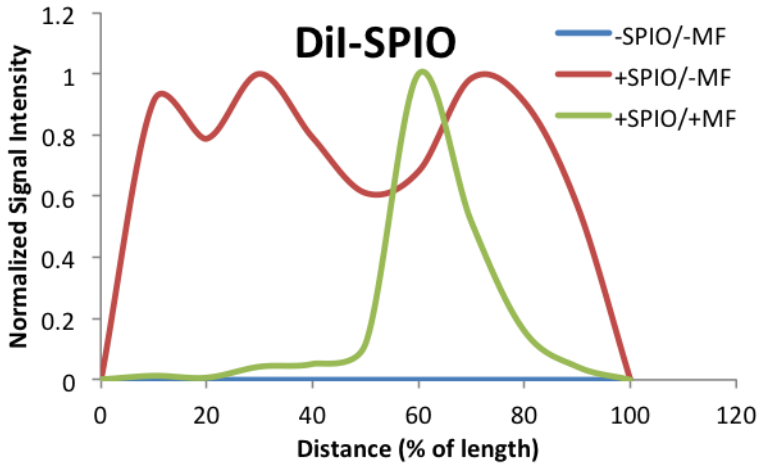

Figure 6.9. DiI-SPIO signal from Figure 6.8 for the three cell conditions.

As expected, SPIO signal changes from distributed throughout the cell body to concentrated at the fore half of the cell.

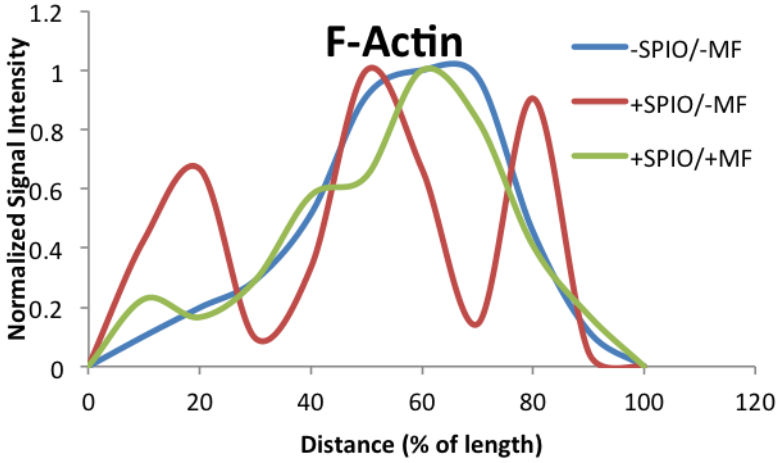

Figure 6.10. F-Actin signal from Figure 6.8 for the three cell conditions.

Actin signal does not colocalize with DiI-SPIO signal indicating that SPIO labeling inhibits actin polymerization within the same plane of SPIO cytosolic clustering.

This can be observed for both SPIO labeled conditions. Additionally, actin stress fiber signal is enhanced for both SPIO labeled conditions.

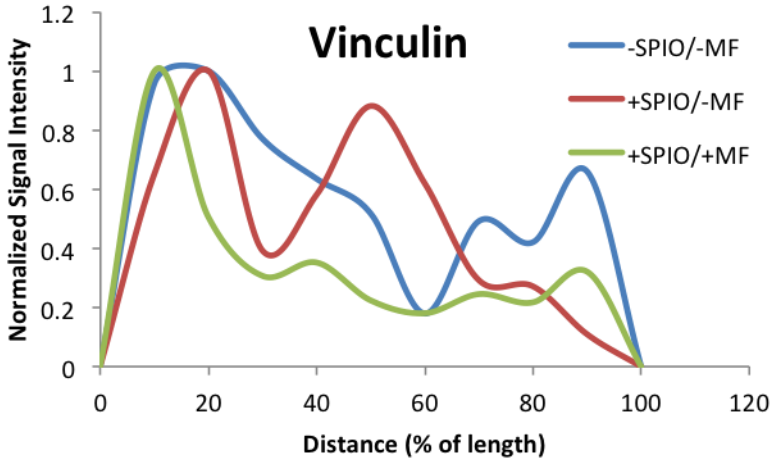

Figure 6.11. Vinculin signal from Figure 6.8 for the three cell conditions.

Vinculin signal changes, on average, from a primarily perinuclear localization in the –SPIO/-MF cells to widely dispersed throughout the cell body in the +SPIO/+MF cells. For the +SPIO/+MF condition, vinculin signal is primarily located at the opposing half of the cell (width-bisection) of SPIO clustering indicating focal adhesion polarization across the length of the cell body.

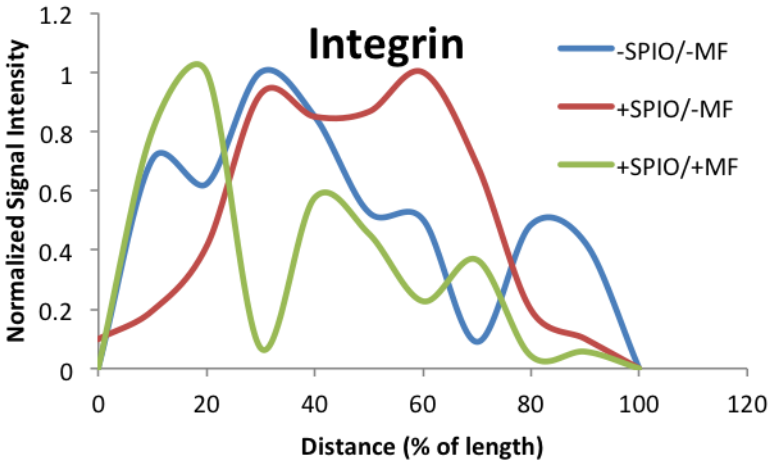

Figure 6.12. Beta1-Integrin signal from Figure 6.8 for the three cell conditions.

Similar to vinculin signal, integrin signal is primarily localized in the perinuclear region for the –SPIO/-MF cells when circular but polarizes across the cell length when spread. The +SPIO/-MF cells maintain this perinuclear localization whereas the +SPIO/+MF cells present a polarized signal distribution across the cell length.

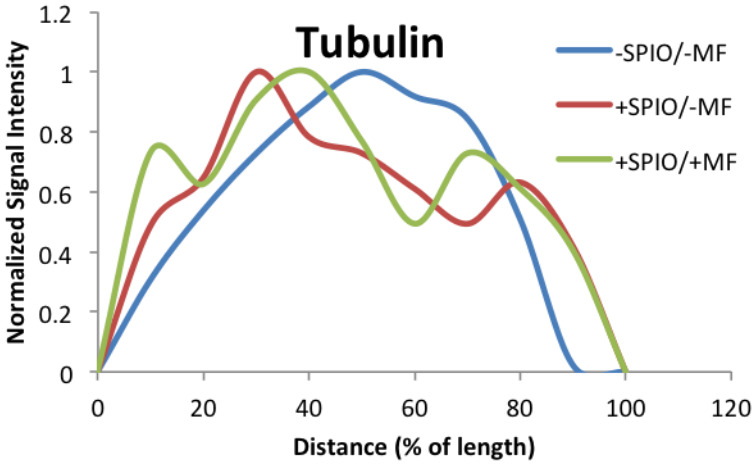

Figure 6.13 α-Tubulin Signal from Figure 6.8 for the three cell conditions.

Microtubule polymerization did not exhibit any major changes across the negative control and that of the +SPIO/-MF cell groups but presented an enhanced signal in the perinuclear region of the cells for the +SPIO/+MF group, experiencing a magnetic force.

Cell Area and Shape

In order to better understand the cell's mechanical response to this magnetically induced endogenous force, cell shape and area was measured for the three conditions in the presence of cytoskeletal inhibitors. α-Tubulin polymerization was inhibited with Nocodazole at a concentration of 0.25 μM, actin polymerization was inhibited with Cytochalasin D at a concentration of 2 μM, and actin/myosin contraction was inhibited with Blebbistatin at a concentration of 12 μM. All inhibitors were added to the MSC Basal Medium at the aforementioned final concentrations and cells were incubated for 24 hours. Cell area and shape was determined by cytosolic staining (calceinAM), ImageJ threshold filtering, area and roundness analysis for at least 24 cells per condition. Data is presented in Figure 6.14. Subfigure 6.14.A presents the variations in cell shape and area for the untreated cells with no significant differences in cell shape by either a measure of aspect ratio or circularity. General trends for each respective inhibition is noticed in Subfigures 6.14-B and C. Consistent with previous studies, cell area for +SPIO/-MF is lower that the negative control with a 23.9% decrease in average area in this experiment. For the three inhibitor conditions, numerous interesting observations were made.

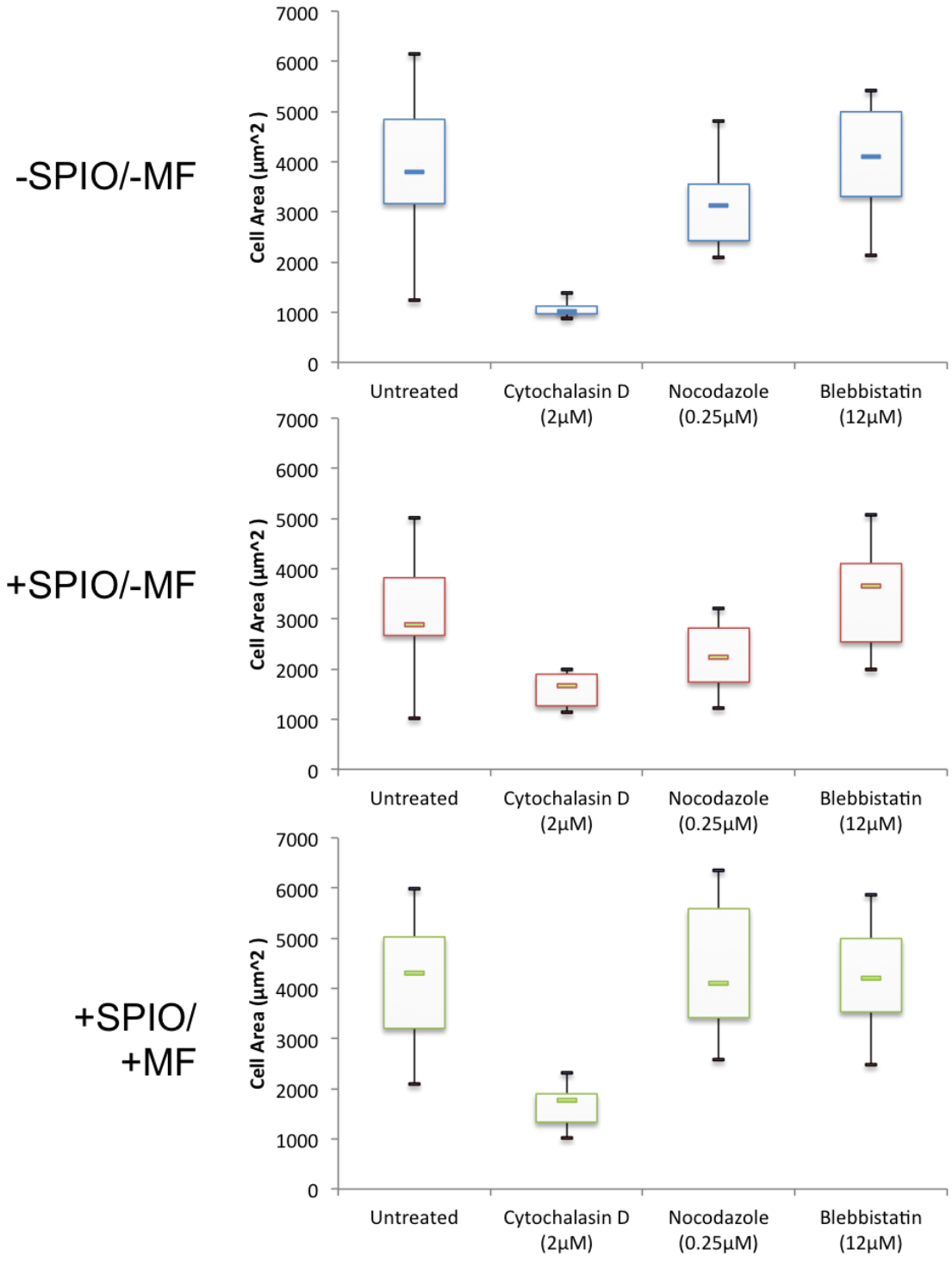

Figure 6.14. Cell Area Reported by Median and Middle 50% Population. Cell Area reported after a 24 hours incubation with each respective inhibitor: Cytochalasin D, Nocodazole, and Blebbistatin.

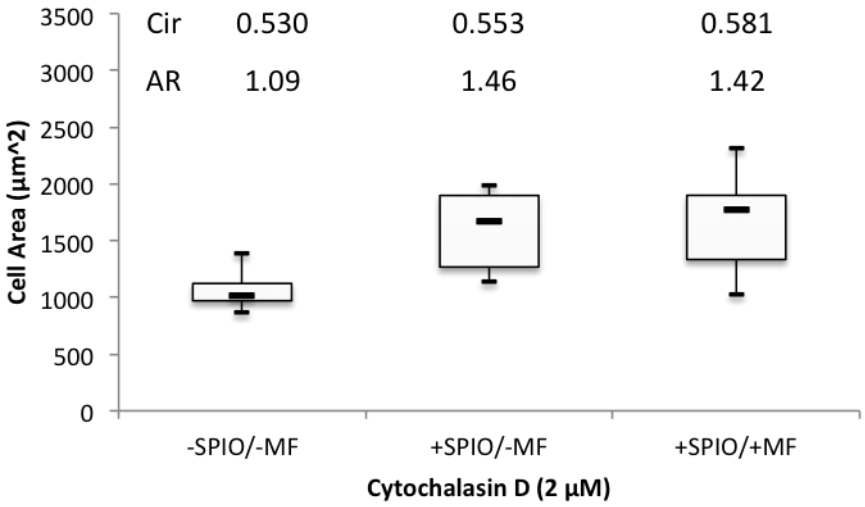

Figure 6.15. Cell area, Roundness, and Aspect ratio for –SPIO/-MF, +SPIO/-MF, and +SPIO/+MF cell conditions after 24 incubation with 2 µM Cytochalasin D treated MSC basal medium.

As expected, the cell area for the –SPIO/-MF negative control dropped significantly to less that 27% of its original spread area with a highly circular shape (median drop from 3801 μm^2 to 1010 μm^2). However, although both SPIO labeled cells followed suit by observing a loss in median cell area, a substantial retained area when compared to the negative control was noted for +SPIO/-MF and +SPIO/+MF, median values of 1679 μm^2 and 1769 μm^2 respectively. This retained area can likely be attributed to the enhanced resistance to compressive forces from the increased cell stiffness observed for SPIO labeled MSCs.

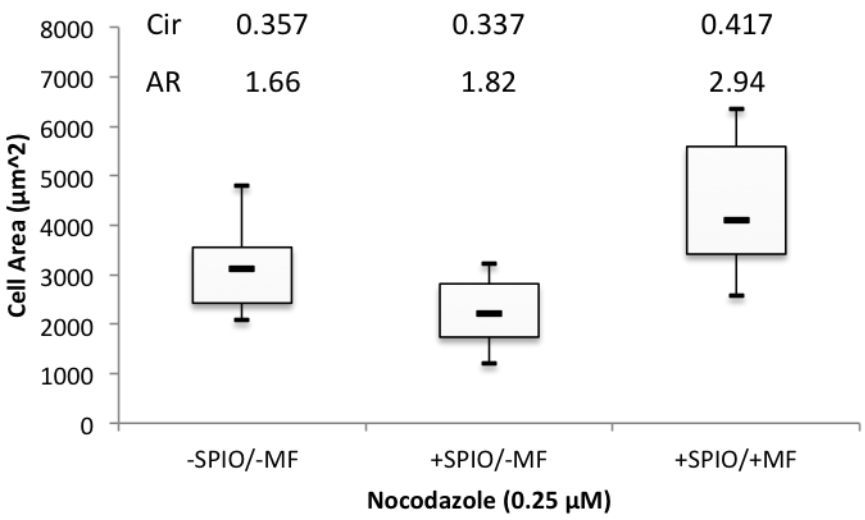

Figure 6.16. Cell area, Roundness, and Aspect ratio for –SPIO/-MF, +SPIO/-MF, and +SPIO/+MF cell conditions after 24 incubation with 0.25 µM Nocodazole treated MSC basal medium.

Inhibition of microtubule polymerization had no measureable effect to +SPIO/-MF cells in either shape or area when compared to the negative control but the +SPIO/+MF cells exhibited increased cell area over both the –SPIO/-MF and +SPIO/-MF cell populations. Additionally, the +SPIO/+MF group exhibited additional cell stretching confirmed by the increase in mean aspect ratio of 48% from the same population when not treated with nocodazole. This cell stretch indicates an enhanced experienced force on the cell body by the magnetically activated SPIOs in the absence of microtubule polymerization that mechanically provides resistance to tension [59, 60].

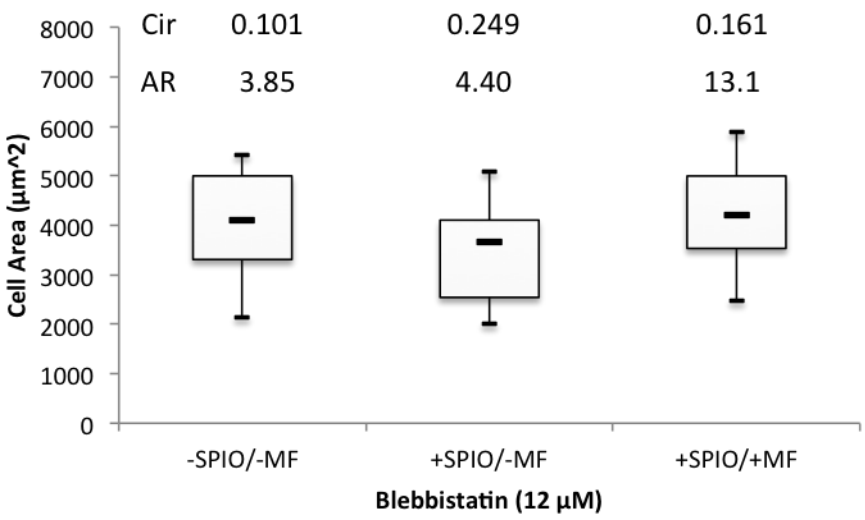

Figure 6.17. Cell area, Roundness, and Aspect ratio for –SPIO/-MF, +SPIO/-MF, and +SPIO/+MF cell conditions after 24 incubation with 12 µM Blebbistatin treated MSC basal medium.

All three conditions maintained general cell area but exhibited substantial shape change with sharply pointed protrusions. Where the –SPIO/-MF and the +SPIO/-MF groups presented 3 and 4-point star shaped cell bodies, the +SPIO/+MF group presented long single tail extensions. The significant difference in cell shape can be noted in the average observed aspect ratio of 13.1 (Figure 6.17) for the magnetically active SPIO labeled cell group.

Discussion

After delivery of SPIOs into the cytosol of MSCs, a variety of external magnet arrangements were used to relocate the nanoparticles into clusters in the forward half of the cell. The attractive force of the neodymium magnetic field acting on the now “active”

SPIOs is capable of not only reorganizing the nanoparticles within the cell body but sufficiently strong enough to cause cell body deformations. When focused on forming artificial protrusions by using a unique paired magnet arrangement, previously unreported in the literature, on SPIO loaded MSCs long lamellipodial extensions were formed which deviated slightly from the traditional fanned conformation taken by traditionally motile MSCs [60]. During the formation of these initial extensions within the first 40 minutes of magnet exposure there was a noticeable increase in MSD indicative of an increase in speed similar to what was noted in the comparative model of Aim 1. Once the nanoparticle reorganization reached equilibrium, at or around 40 minutes of magnet exposure, the MSD maintained a steady rate similar to the negative control, indicating no measureable speed change. This finding is especially important for understanding the difference between the directional influences of the experienced force on the cell body. Since the protrusion model used a paired magnet arrangement designed to minimize any z directional force on the cells we had hypothesized that adhesions would be minimally affected. This two-step response shown in the protrusion MSD data seems to support this hypothesis.

Wherein the first phase the reorganization of SPIOs increases the lamellipodial area by extending the cell body in the direction of the magnetic field thus forming nascent focal adhesions polarizing the cell body. This reaction is similar to starting of the engine and aligning the steering wheel as we see the creation of a directional path towards the highest gradient of the magnetic field and an immediate increase in speed for the first 40 minutes. The steady state response is much more similar to cruising. The number of focal adhesions is unlikely to change once the artificial protrusion has reached

in maximum extension and SPIO reorganization is completed. At this point, without a z component to the magnetic field, the SPIOs cannot contribute an effect to focal adhesion maturity (or disruption) that might cause a change to migration speed, it seems to only maintain direction.

On the other hand, when reintroducing the z component of the magnetic field substantial adhesion effects were reported. SPIO labeled cells alone did not adhere as well as the negative control in a centrifugal detachment study caused primarily by an inability to spread. The rate of cell spreading of SPIO labeled cells was substantially lower than both the negative control and the force loaded cells, even after the cells had fully spread at 24 hours, the total cell area only reached about 61% of the negative control. We believe that this difference in cell spreading is caused by an increase in cell stiffness and therefore increasing the contribution cortex tension has on the rate of cell spreading. This stiffness change was confirmed by more than quadrupling of the SPIO labeled MSCs' Young's Modulus from a mean of 1.19 kPa to 5.24 kPa when measured in the cytosol immediately outside the nucleus. Although this study indicated a significant increase by unpaired t-test with a p value of 0.005 and was conducted for a sample population each of no less than 24 cells it was for a very specific location and no overall stiffness claims can be made for the entire cell body. However this significant difference near the nucleus where SPIO density is highest helps understand this difference in cell spreading and average cell area when actin polymerization is inhibited by Cytochalasin D. SPIO labeling alone is sufficient to add some structural integrity to the MSCs supported by these two findings.

When MSCs are manipulated with a mechanical force caused by SPIOs and a magnetic field, a number of interesting observations were made. Overall, this kind of force loading is unidirectional and allows for recovery of many of the effects noticed in SPIO labeled cells without a magnetic field. These cells mimic the natural polarization seen in the negative control throughout all of these studies and even enhance the rate of cell spreading, adhesion strength, and actin and microtubule stress fiber formation after limited exposure to a magnetic field (3-4 hours) [61]. These findings paired with the increased aspect ratio for SPIO/MF cells with nocodazole and blebbistatin and the heightened local signal of microtubule formation located between the nucleus and the leading SPIO cluster support the belief that the tensile force experienced in the cell truly has a mechanical component.

Conclusion

These cellular responses to a mechanical force caused by internalized MNPs and common static magnets demonstrate that multiple mechanotransduction mechanisms are activated that has not been reported on previously. This force is sufficiently strong to cause increases in adhesion strength, actin and microtubule reorganization, and large cell stretching and cell body configurations.

CHAPTER 7

BYSTANDER CELL MIGRATION

Introduction

As we have shown, MSCs under magnetic force loading exhibit changes in cytoskeletal and focal adhesion protein including actin, tubulin, integrins, and vinculin. These components sense and modulate mechanical responses within the cell through a number of signaling pathways. Talin, vinculin, α-actinin, and paxilin are among focal adhesion protein at the forefront of mechanical sensing and have been known to be quite force dynamic [62]. In the case of vinculin specifically, a conformational change from an inactive to active state can require as little as 1-12 pN of force. Vinculin additionally served a major role in all three stages of the focal adhesion life-cycle: formation, stabilization, and disassembly and thus has a high rate of cycling and control over the cycling rate of other focal adhesion protein [62]. Figure 7.1 shows the pivotal role vinculin plays in downstream signaling as a major mechanosensing protein.

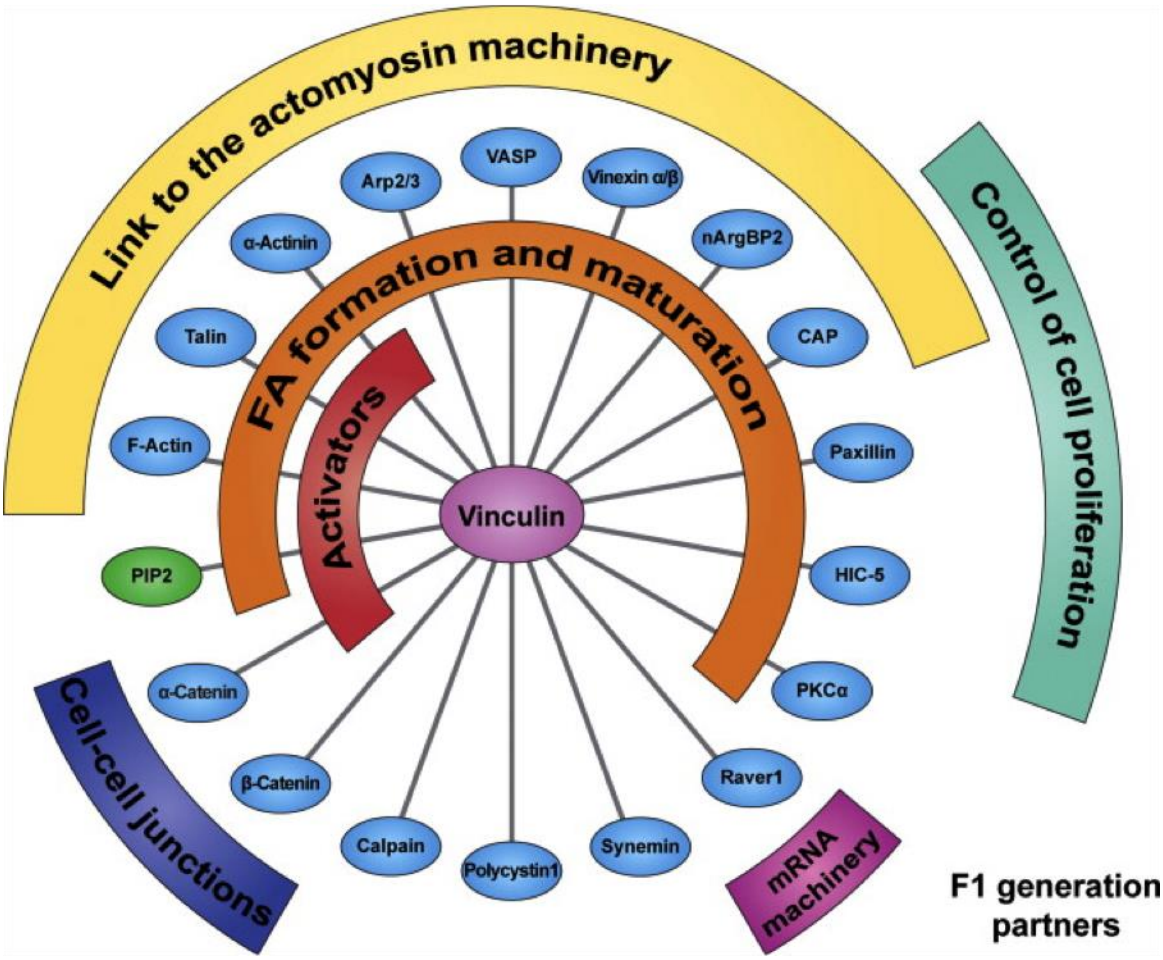

Figure 7.1. Summary of the Role of Vinculin in Cell Biology. Representation of the direct binding partners of vinculin linked to their reported functions. Blue ovals indicate protein, green ovals indicate phospholipids. The semi-circular areas outline the reported function as a consequence of vinculin binding to its individual partner. This figure is originally sourced from a short review by Carisey et al. in the European Journal of Cell Biology [62].

Force loading of MSCs and the noticeable changes to cytoskeletal reorganization and FA protein distribution could have secondary signaling effects that modify cell secretion factors. These modified secretion factors would alter the cell environment

leading to measureable effects to bystander cell populations. Within the popular use of MSCs in regenerative medicine these bystander cells include: epidermal keratinocytes, fibroblasts, myofibroblasts, and macrophages among others.

MSC Secretome

MSCs exhibit a set of pro-regenerative features that make them attractive candidates for modulation of cell and tissue responses and regenerative therapy approaches. MSCs have multi-lineage differentiation capacity, homing to sites of injury and inflammation, and paracrine pro-migratory, immunomodulatory, pro-angiogenic, anti-apoptotic, and pro-proliferative effects [45]. Most of this research conducted in tumor and wound microenvironments has produced a generally well understood (although some contradicting reports exist) MSC secretome including its paracrine and endocrine migratory secreted factors [46]. CCL5, TGFβ, VEGF, IL-17b, IGF1, EGF, FGF, HGF, SDF1, IL-6 are all identified as pro-migratory secreted factors for a number of cancer cell lines both *in vitro* and *in vivo* [45, 46]. Although a number of these migratory factors have reported enhanced cell migration in wound healing studies; TGFβ, VEGF, IGF1, EGF, FGF, HGF, and SDF1 report direct and measureable migratory effects on keratinocytes and fibroblasts *in vitro [37, 47]*. Signaling pathways for TGFβ, VEGF, HGF, and SDF1 expression has substantially similar stimulatory (Wnt-GCPR, Integrin) and secondary signaling factors (Rho-GTPase, PLC, PKC, APC, IP3) as mechanotransduction pathways in MSCs allowing for the possible activation and up/down-regulation of these migratory factors under force loading conditions [37, 45].

Keratinocytes

In the repair of cutaneous wounds it is essential for the wound to be resurfaced as quickly as possible in order to regain structural and functional integrity [47]. This step is achieved by the proliferation and directional migration of keratinocytes from the edges of the wound into the wound space. Intercellular junction complexes must be disrupted in order for migration of keratinocytes to occur and is initiated by direct interaction with the provisional matrix that forms within the wound bed [47]. This fibrin, fibronectin, and vitronectin-rich matrix serves as a functional scaffold for a number of other wound healing cells but is especially necessary for keratinocyte directed migration. Interkeratinocyte adherens junctions have been shown in human epidermis and a release from tight and adherens junctions cause the loss epidermal cell polarity and enables keratinocyte migration [47, 63]. Various growth factors influence keratinocyte colony dissociation, shape, and motility. Hepatocyte Growth Factor (HGF/Scatter Factor) promotes cellular scatter and dissociation of adult epidermal keratinocytes from colonies and clusters [17, 64]. Insulin-like growth factor-1 (IGF-1) stimulates membrane protrusion and cell spreading [63, 64]. Epidermal growth factor (EGF) induces contraction and influences motile cell retraction [16, 63, 65, 66].

Migratory signaling cytokines

Table 7.1. Literature Compilation of Promigratory Cytokines for Keratinocytes

Cytokine	Pro-migratory Concentration	Substrate-enhanced migration	Source	Note
EGF	0.1-100 ng/mL	Fibronectin, Collagen I, Collagen IV	[16, 63, 65-68]	IGF-1 (100 ng/mL) AND EGF (10ng/mL) >> IGF-1 OR EGF
FGF-1,2,7	1-20 ng/mL	Collagen I	[16, 64, 69, 70]	
FGF-10	10 ng/mL + dermatan sulfate (2 µM)	-	[69]	
HGF	5-250 ng/mL	-	[17, 64, 71]	64% wound closure @ 250 ng/mL
IGF-1	8-100 ng/mL	Collagen IV	[63, 64]	
TGF-α	3-200 ng/mL	Fibronectin, Collagen I, Collagen IV	[16, 64, 65, 70]	TGF-α @ 170 ng/mL > EGF @ 64 ng/mL
TGF- β1	2-25 ng/mL	-	[16, 64, 71, 72]	HGF (4-6 ng/mL) AND TGF- β1 (1.5-2 ng/mL) >> HGF OR TGF-β1
VEGF	0.1-10 ng/mL Ca^{2+}(100 ng/mL)	Fibronectin	[67]	Low [Ca^{2+}] and integrin activation dependence

Numerous families of growth factors and cytokines have been tested for effect on cell migration on keratinocytes including but not limited to the: EGF family (EGF, TGF-α, HB-EGF), FGF family (FGF-1, FGF-2, FGF-7, FGF-10), VEGF family (VEGF), PDGF family (PDGF), IGF family (IGF-1,) ANGPTL family (AGF), IL family (IL-1 α, IL-6, IL-8), α-chemokine family (MGSA), and other smaller cytokine families (TGF-β1, HGF, NGF, HMGb1, IP-9 and IP-10) [47]. The majority of these effects have been studied *in vitro* with scratch assay and Boyden and transwell chambers to simulate wound repair *in vivo*. Although multiple pro-migratory growth factors and cytokines have been

found with their respective effective concentrations, new findings have shown that growth factors in combination may be synergistically stimulatory for wound repair than either applied alone. In two specific instances, EGF/IGF-1 and HGF/TGF-β1, combinations of growth factors have caused a greater increase in migration than the same growth factors alone. Other combinations have been speculated in the literature as pro-migratory including, FGF-2/TGF- β, PDGF/TGF-α, PDGF/IGF-2, and FGF-2/IGF-2.

There is a high correlation between keratinocyte pro-migratory cytokines and MSCs' migratory secretome that incorporate these cytokine combinations allowing for stimulation of bystander migration with MSC conditioned media. Specifically, VEGF and HGF/TGF-β1 produce the greatest overlap and potential for a talin/vinculin specific secretion in MSCs and a promigratory effect in keratinocytes.

Results

In order to determine the influence magnetically induced force loading has on MSC secretion factors (refer to Figure 7.2) (1) hMSCs were labeled with SPIOs as previously described and (2) were placed directly on top of a magnetic grid array with magnetic interfaces producing magnetic field gradients as high as 250 mT within 1 mm from the surface. Using this magnetic setup over 80% of the cells within a 1-well LabTekII plate exhibited the expected profile for directional force loading with no uniform direction. Cells were kept in this culture condition for 3 days in serum-depleted media. Then, (3) the conditioned media was taken and secreted factors were quantified by enzyme-linked immunosorbent assay (ELISA) for VEGF, HGF, and TGF- β1.

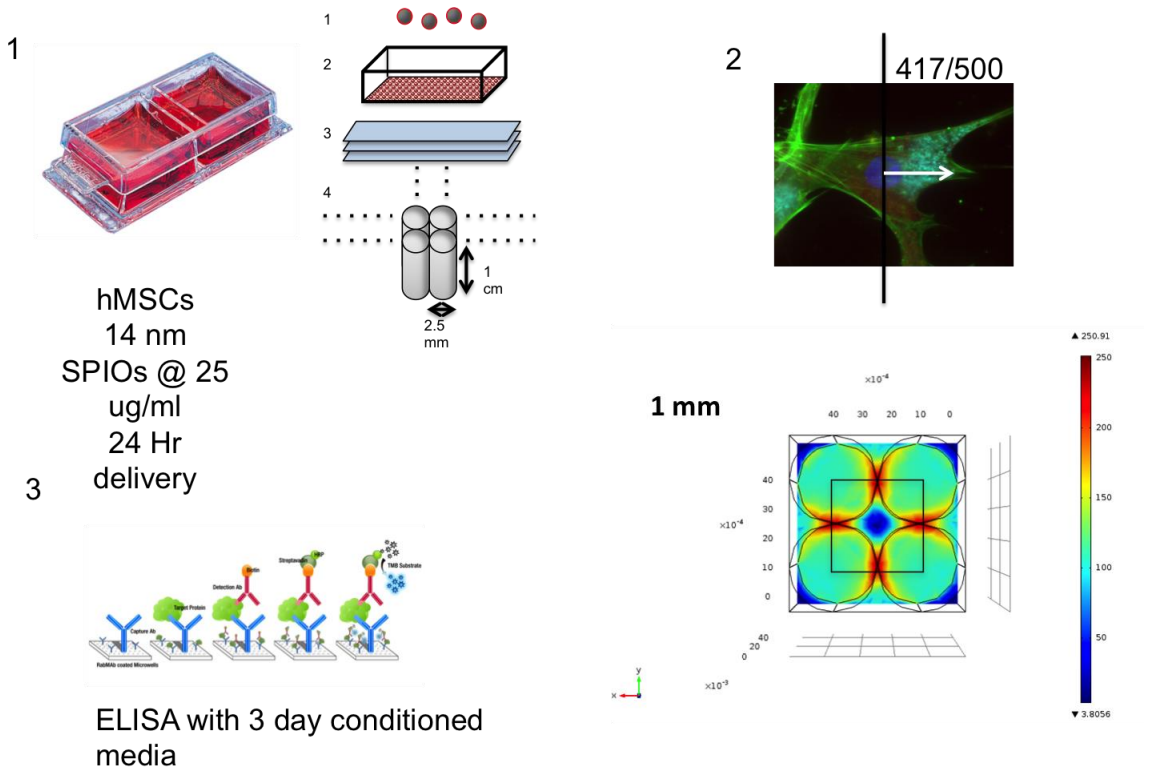

Figure 7.2. MSC Secretion ELISA Schematic. Experimental setup for measuring of VEGF, HGF, and TGF- β1 secretion in 3 day conditioned media by ELISA. (1) Depicts the SPIO delivery method as explained in Aim 1. (2) Depicts a representative cell in the traditional polarized conformation of magnetic loading and the magnet array used to achieve such conformation. (3) Depicts the antibody binding schematic by Abcam, Inc. of the sandwich ELISA used for quantification.

Conditioned media concentrations were measured for VEGF, HGF, and TGF- β1 as adjusted for 1 x 10^6 cells/mL in order to compare quantity release for a standard cell population. Figure 7.3 represents measured quantities for the three selected cytokines for the three culture conditions of –SPIO/-MF, +SPIO/-MF, and +SPIO/+MF. No significant change in VEGF release was noticed however a substantial increase in TGF- β1 release

was noticed for both SPIO labeled controls although only the +SPIO/+MF reported significance. HGF release was highly elevated in only the magnetically force loaded cells with a 54% and 40% mean increase from the –SPIO/-MF and +SPIO/-MF conditions respectively in a significant way.

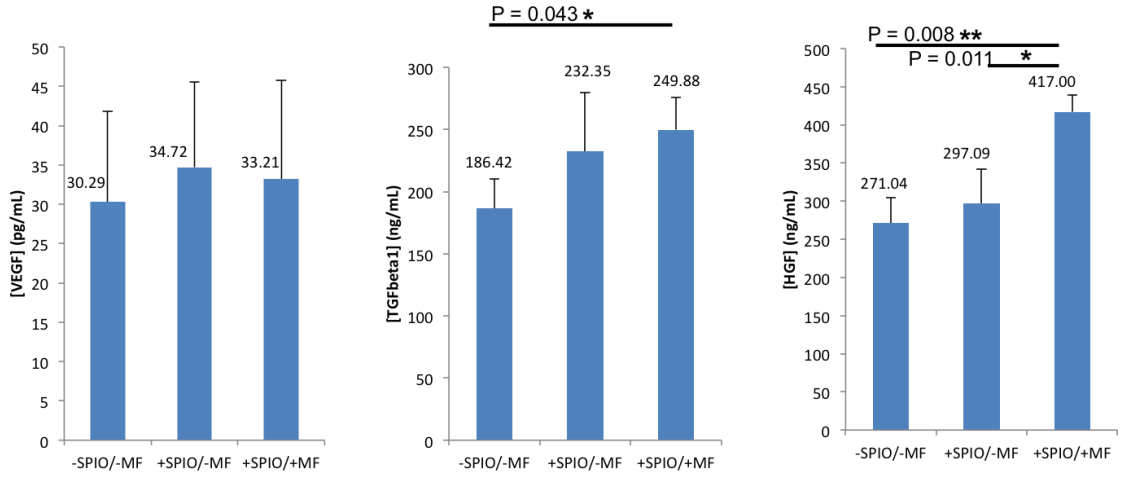

Figure 7.3. Growth Factor Secretion Levels of MSCs. Quantification of secretion of VEGF, TGF- β1, and HGF reported in mass quantity per mL for an adjusted cell density of 1 x 10^6 cells/mL.

VEGF release fell well below threshold value of (0.1-10 ng/mL) for promigratory paracrine signaling in neonatal human epidermal keratinocytes and thus was not further explored in soluble form for subsequent studies. Before measuring the effect of this MSC conditioned media on neonatal human epidermal keratinocytes (NHEK) media optimization and positive controls of soluble HGF and TGF- β1 were established for cell migration studies across 8 μm pores in transwell chambers selected specifically for the much smaller keratinocytes. Media mixtures of MSC basal media and keratinocytes basal

media both sourced from Lonza was assessed for NHEK migration rates and cell viability after 24 hours. Results are reported in Figure 7.4.

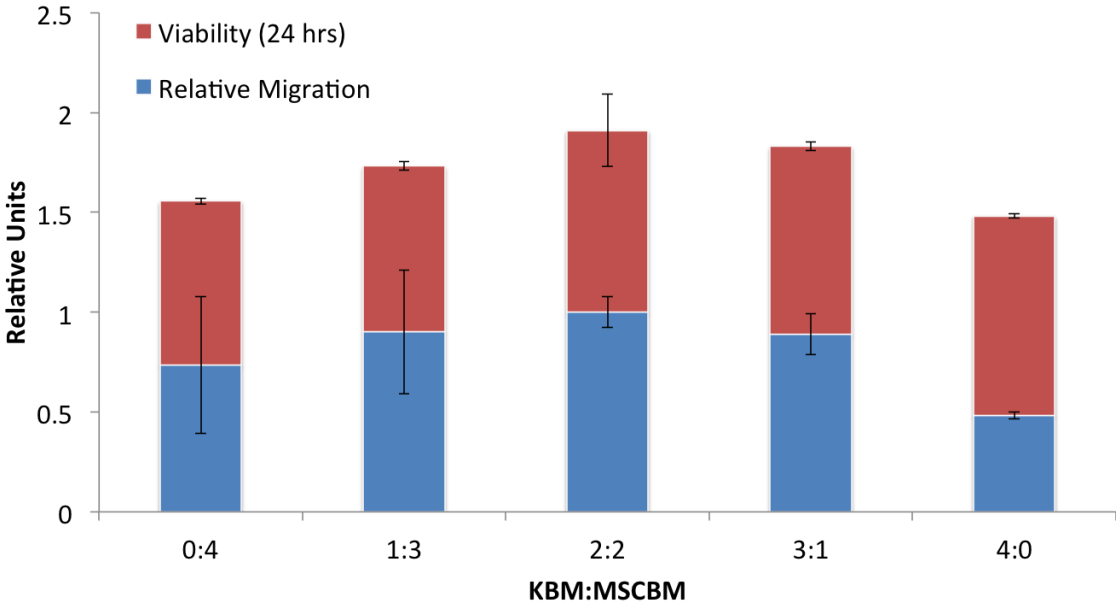

Figure 7.4. Coculture Media Optimization. Relative migration and viability is reported for five media mixtures as basal medium ratios by volume. Migration was measured by calceinAM fluorescence signal after transwell migration and viability by MTS assay after 24 hours.

Of the five media mixtures tested volume ratios of 2:2 and 3:1 KBM:MSCBM outperformed the rest. Although a media mixture of 2:2 outperformed the 3:1 mixture in relative migration on average, the improved viability of the 3:1 mixture took precedence over the slight increase in baseline migration. A 3:1 KBM:MSCBM media mixture was used for all subsequent experiments.

Next, soluble HGF and TGF- β1 were incubated in the above mentioned media mixture in transwell chambers seeded with 20,000 cells per well at final concentrations

ranging the promigratory concentrations reported in the literature for synergistic response. HGF concentration ranged from 0-15 ng/mL in 3 ng/mL increments and TGF-β1 concentrations ranged from 0-4 ng/mL in 1 ng/mL increments. Figure 7.5 reports transwell migration across these concentration combinations after 24 hours incubation with soluble growth factor treated media. TGF- β1 increased concentration alone contributed to increased transwell migration at low concentrations where a plateau is reached by 2 ng/mL in the presence of no HGF. The combination of HGF and TGF- β1 at various produce local maxima for concentration ratios of 3 ng/mL HGF and 1 ng/mL TGF- β1, 6 ng/mL HGF and 2 ng/mL TGF- β1, and 9 ng/mL HGF and 4 ng/mL TGF- β1. Above 9 ng/mL HGF in the presence of any TGF- β1 there is no measureable effect to relative increased transwell migration. Additionally, the presence of TGF- β1 at any of the measured concentrations with HGF outperforms HGF alone for all concentrations between 3 ng/mL and 12 ng/mL. Additionally the reverse is true indicating synergy.

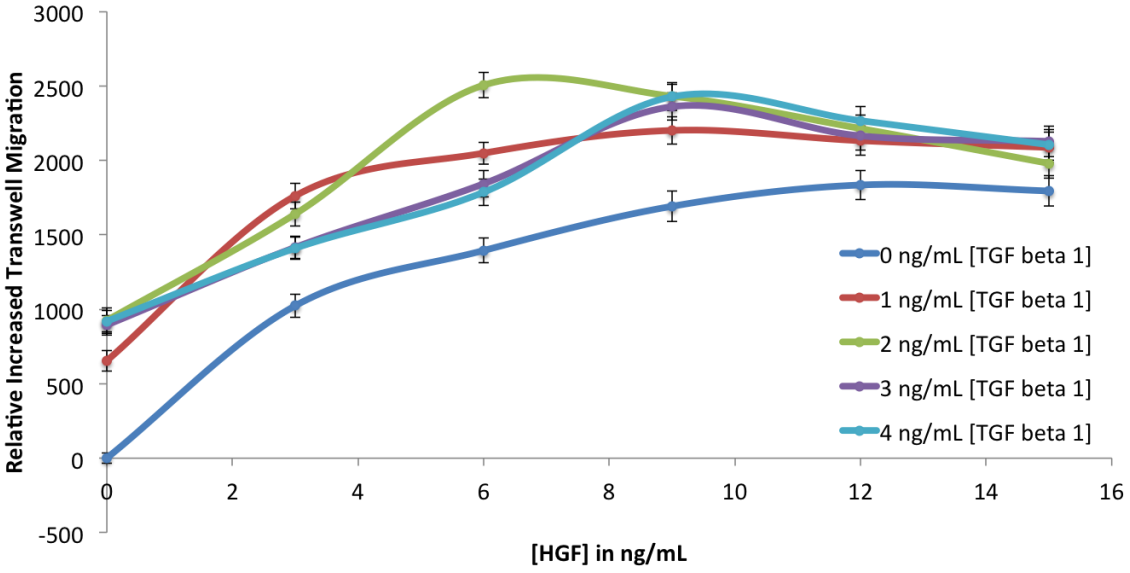

Figure 7.5. HGF/TGF beta 1 Effect on NHEK Transwell Migration. Relative increase in transwell migration across HGF and TGF- β1 concentration combinations from 0-15 ng/mL and 0-4 ng/mL respectively. Data is background subtracted for baseline migration in 3:1 KBM:MSCBM media with 0 ng/mL of either soluble factor.

Once soluble growth factor effect was established, the conditioned media from the three previous conditions: -SPIO/-MF, +SPIO/-MF, and +SPIO/+MF after ELISA analysis was used to measure relative transwell migration at diluted concentrations of HGF release in order to compare to the soluble HGF/TGF- β1 measured soluble factor effects. Figure 7.6 displays the comparisons between conditioned media contribution to relative transwell migration and that of the respective 3 ng/mL and 6 ng/mL HGF soluble growth factor response for the three TGF- β1 concentrations of 1, 2, and 3 ng/mL. The HGF/TGF- β1 concentration ratios from the conditioned media is fixed and falls slightly

below the optimal synergistic ratio of 2:1 – 4:1, HGF:TGF- β1 reported in the literature and confirmed in Figure 7.6.

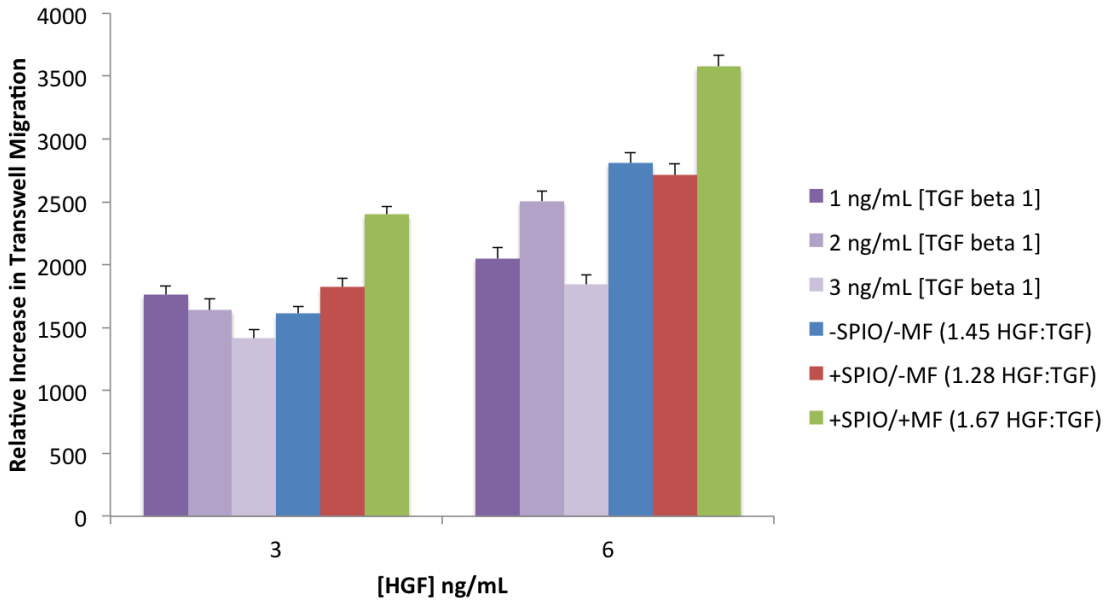

Figure 7.6. Transwell Migration of NHEK cells in MSC Conditioned Media. Relative increase in transwell migration reported for HGF/TGF- β1 soluble growth factor effects for six combinations ranging from 3-6 ng/mL HGF and 1-3 ng/mL TGF- β1 as well as the additional three conditions of –SPIO/-MF, +SPIO/-MF, and +SPIO/+MF diluted to comparable HGF concentration for direct comparison. All samples are background subtracted to a baseline transwell migration from a 3:1 KBM:MSCBM media mixture negative control.

Discussion

This study when taken as a whole reports on the potential effects of magnetic force loading on MSCs on changes to secretion factors. Although only three known pro-migratory cytokines were measured a significant upregulation of HGF and TGF- β1 was

reported which could have substantial paracrine or autocrine signaling effects. One such comparison was measured at reported in the case on MSC conditioned media with a reasonable cell test model. These cells show high levels of overlap between MSC known secretion and scatter/migratory responses in NHEKs and of the many reported cytokine that do overlap, three of the major contributors were selected, VEGF, HGF, and TGF- β1 [47].

VEGF is known to contribute significantly to adhesion effects in NHEKs and disrupt cell-cell interactions this promoting cell migration [64]. HGF/TGF- β1 each individually contribute to NHEK migration through semi-independent mechanisms and have been known to act synergistically in concert. Although VEGF release was not altered by the magnetic force loading mechanism and the baseline release fell well below the known migratory signaling concentration in NHEKs, additional measurements of VEGF and calcium ion concentrations should be explored under different magnetic form loading conformations and shorter time cycles as MSCs are known to be highly responsive to autocrine signaling of VEGF that could have contributed to the response reported herein. HGF/TGF- β1 as soluble factors contributed to NHEK migration consistent with reported literature when adjusted for concentrations/cell for the short concentration ranges reported in this study. Similar to VEGF, time delay, autocrine uptake, and specific magnet arrangements weren't explored and may result in differing up- or down- regulation of growth factor secretion but for the measured effect to both from magnetically force loaded MSC, a substantial upregulation was noted.

The migratory response of NHEKs to MSC conditioned media was not surprising as the HGF concentration was diluted to equal that of the soluble factor controls but what

was surprising was that the +SPIO/+MF condition still significantly outperformed all compared conditions despite carrying a different HGF/TGF- β1 concentration ratio. Unfortunately, the promigratory effect noted in this condition cannot be attributed to HGF/TGF- β1 secretion alone, as no other cytokines that could have made a similar contribution was measured and a more systematic approach of individual knockout or suppression would be needed to pinpoint the primary contributor; HGF/TGF- β1 is likely to be a contributing factor.

Conclusion

This study overall presents a proof of concept that magnetic force loading of MSCs does have a significantly measureable effect on migration secretion factors of HGF and TGF- β1 and conditioned media for this type of cell treatment increases the relative transwell migration of NHEKs in excess of HGF and TGF- β1 soluble factors alone for all pro-migratory concentration combinations reported in the literature. This provides some fuel to the further exploration of paracrine upregulation in force loaded MSCs and its potential effect to bystander cells like NHEKs.

CHAPTER 8

CONCLUSIONS AND FUTURE DIRECTIONS

Burgeoning progess in the field of nanobiotechnology and MNP cell manipulation holds great promise for improving biomedical research and regenerative medicine applications particularly of wound healing where surface magnets have the greatest potential for strong fields. By investigating mechanical cell responses to this unique method of manipulating MSCs with remote controlled MNPs from the cytosol previously unknown, this thesis contributes to the advancement of the field.

First, a delivery method and comparative migration model was developed in order to evaluate the effect an experiences mechanical force has on bulk cell migratory response. Iron loaded cells can be used to specifically direct migration under static magnetic fields when internalized into MSCs by mechanical stress. Work previously done on magnetic force calculations on magnetic nano- and micro-beads in microrheology studies through the use of magnetic tweezers and other static and dynamic magnetic fields, have shown that the force exerted on an individual iron nanoparticle can range from 500-2400 pN [13]. A similar although unique model was developed for the SPIOs resulting in highly controlled directional persistent cell walking with enhanced average speed over 200 minutes on a fibronectin substrate. These forces were further investigated to understand the direct effect this magnetic force loading has on focal adhesions and cytoskeletal reorganization. Previously unreported effects were noticed and surprisingly, the delivery of SPIOs alone contribute to a number of adhesion

observations that can help explains some of the difficulties reported in the field for MRI tracking of SPIO labeled transplanted stem cells.

Finally, we demonstrated that there is a plethora of unanswered questions to expand this line of study towards cellular reprogramming and behavioral modifications of MSC by reporting secretion upregulation of specific cytokines. These changes to MSC secretion has substantial implications on not only a change in behavior of stem cells but that of bystander cells and the overall cellular environment by autocrine and paracrine signaling. The specific experiments described in this thesis lead to a number of conclusions regarding the affect that SPIOs have on MSCs focused primarily on migratory responses. Moreover, these results invite a variety of further studies that improve on the design of MNP remote control and expand the applications of their use. Several of these potential studies are described below.

Improving the SPIO-Magnetic Field System

While the studies reported in this thesis primarily show bulk cell responses due to the limitations of strong magnet size and magnetic field determination and measurement confidence from factory variations on individual NdFeB magnets, other electromagnet systems can allow for single cell studies and improved analytics on cytoskeletal response. One such common magnet arrangement is the use of Nickel-Iron pulled microrods (refer to Figure 8.1)[73] attached to strong magnets in either a fixed conformation or on actuated controllers on a microscope stand similar to microinjection of micropipette single cell studies.

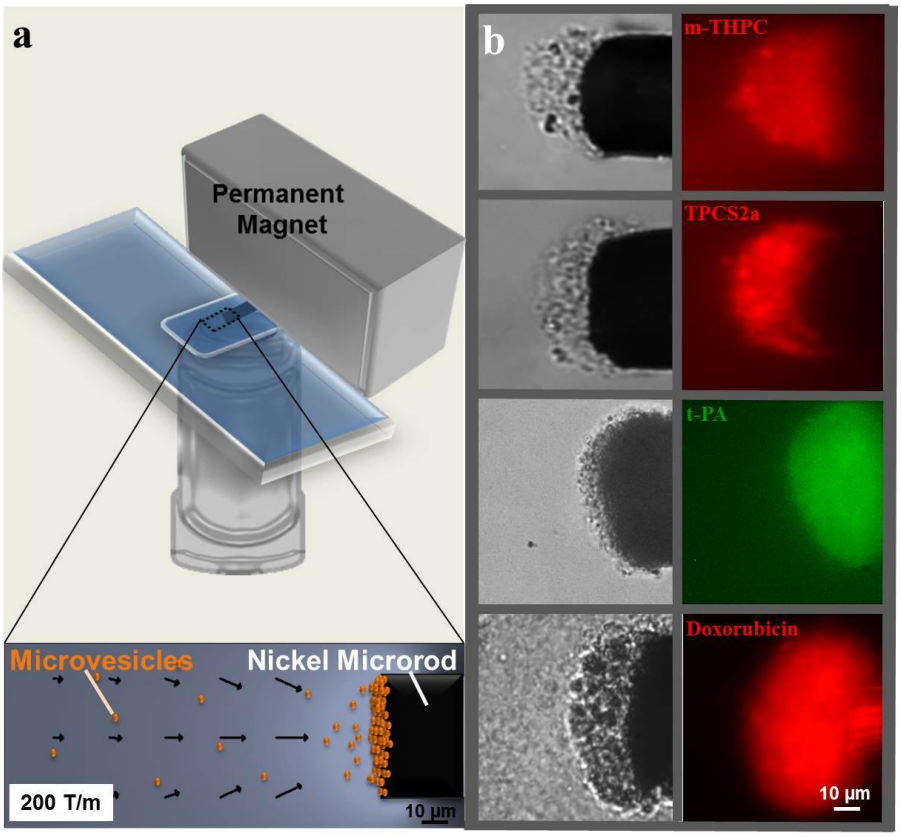

Figure 8.1. Nickel Microrod Magnetophoresis of SPIO Encapsulated Vesicles. (a) Micromagnetophoresis set-up featuring a glass slide/coverslip chamber to which a 50 µm diameter nickel microrod was integrated. Magnetization of the nickel microrod is provided by a rectangular magnet position perpendicular to the micromagnet. (b) Micromagnetophoresis experiment of microvesicles obtained from THP-1 macrophages incubated 2h with 5 mM iron oxide nanoparticles and varying drug types and concentrations and their respective bright field and fluorescent images [73].

Silva et al. here report the ability to concentrate SPIO and cancer drug loaded microvesicles onto this magnet arrangement with excellent visualizations. Other strong and more elegant electromagnets or strong magnet fixed microfluidic models can be designed to accomplish more precise magnetic field influence on individual cells for future studies.

Secretion Factors and Cell Reprogramming

Because of the nature of Aim 3, only the potential for modification of paracrine signaling was determined by magnetic force loading. These results have opened the doors to numerous other applications within determining the force dependence on the MSC migratory secretome initially but has more grand implications of profiling the MSC secretome under this very same arrangement. For immediate studies, addition cytokines listed in the Aim 3 introduction can be tested for short term force loading effect but a more systematic approach would be able to determine more definitely what the bulk secretion effect truly is and secretion and signaling rate changes make this study very ripe for further inquiry. The studies reported in this thesis all take place within 72 hours of force influence, much too short to make substantial changes to differentiation potential and directive programming of MSCs [74]. But because of the multipotency of MSC future developments in long term studies this MNP-magnet system has the potential to be applied towards stem cell directed differentiation and re-programming.

APPENDIX A

ADDITIONAL CELL IMAGES FOR GENERAL REFERENCE

This appendix includes representative cell images of the conformations, cell shapes, and immunofluorochemical staining reported in Aims 1 and 2.

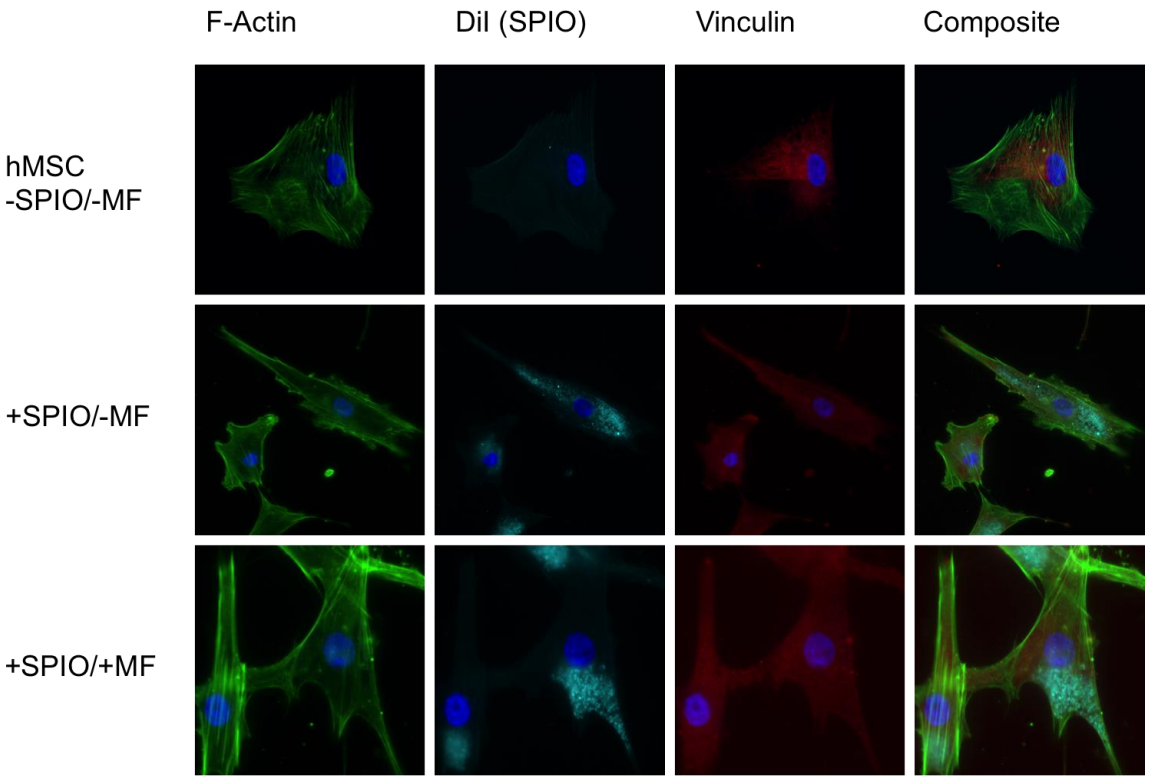

Figure A.1 Panel Images of Actin, DiI-SPIO, Vinculin, for the three cell treatment conditions.

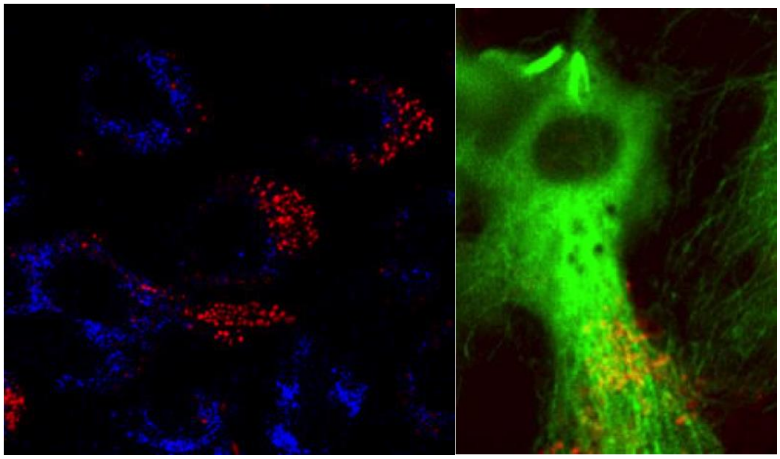

Figure A.2. Images of Beta1 (blue), Tubulin (green), and SPIO (red) of +SPIO/+MF cell treatment group.

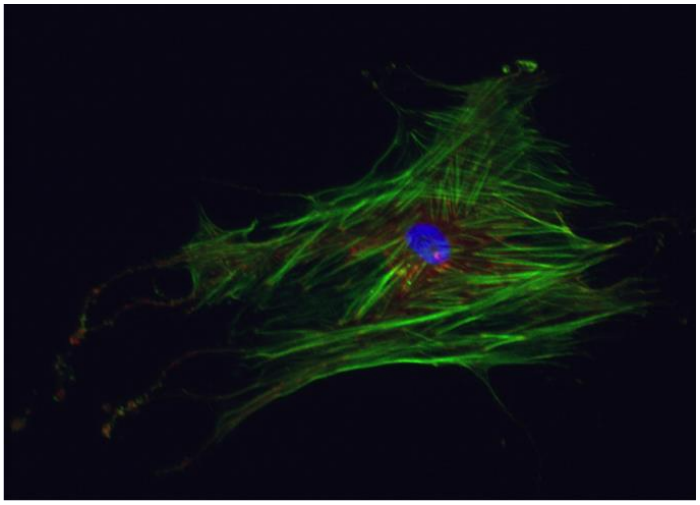

Figure A.3. Single Cell Negative Control. Single cell image with actin (green), vinculin (red), and nuclear staining (blue) of a cell under normal behavior.

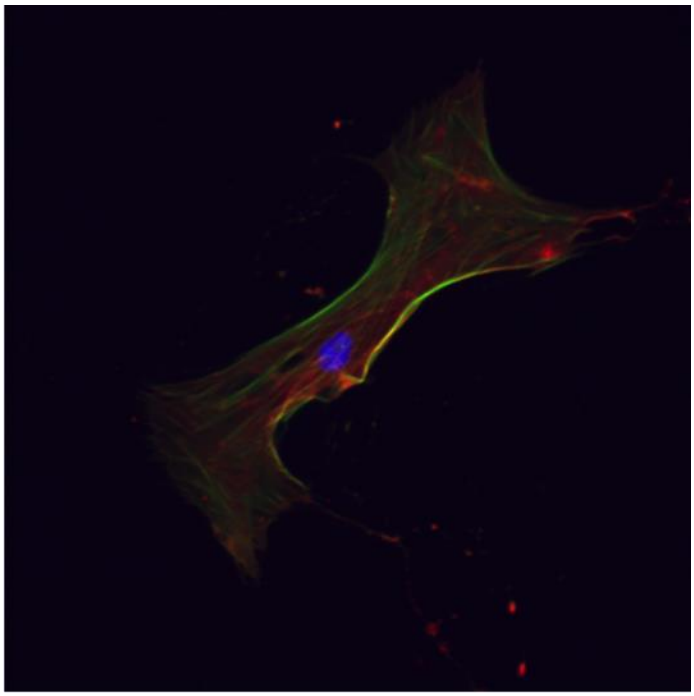

Figure A.4. Stressed MSC. Single cell representation of a SPIO/MF stressed cell expressing a high cell shape aspect ratio and enhanced actin stress fiber formation.

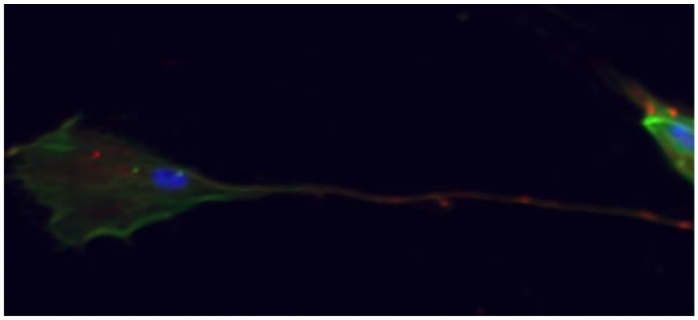

Figure A.5. Elongated SPIO-MSC under Blebbistatin inhibiton. Representative image of a far stretched MSC resulting in a high cell shape aspect ratio and long vinculin rich tail but no star shaped features in the larger cell body.

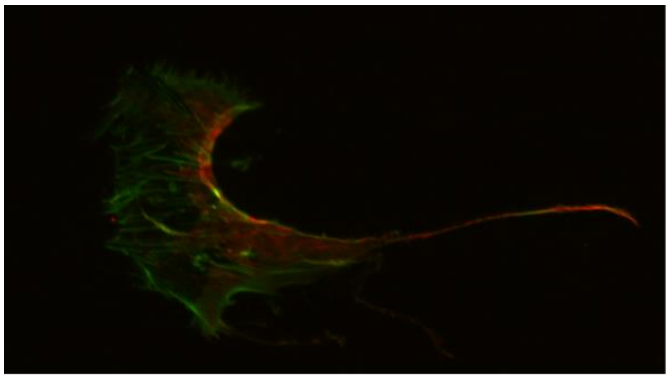

Figure A.6. Fanned Cell Elongation of SPIO-MSC. Representative image of a SPIO loaded Cell under Nocodazole inhibition. The cell body lamellipodia is fanned out slightly in excess of a traditional motile MSC and an occasionally long vinculin rich tail is noted in a large number of cells although not sufficient to change the cell area aspect ratio measurement significantly.

VITA

DAVID CHRISTOPHER SOTTO

David was born in Miami, Florida to Cuban parents. He attended high schools in Miami, Florida at Belen Jesuit Preparatory school, received a B.S. in Biomedical Engineering from Georgia Institute of Technology, Atlanta, Georgia in 2009 before choosing to continue his education at Georgia Tech in pursuit of a doctorate in Bioengineering through the school of Mechanical Engineering. When he is not working on his research, David enjoys playing rugby, reading, and traveling.

REFERENCES

1. Koel, G. and P.E. Houghton, *Electrostimulation: Current Status, Strength of Evidence Guidelines, and Meta-Analysis*. Advances in Wound Care, 2013.
2. Wu, S.C., W. Marston, and D.G. Armstrong, *Wound Care: The Role of Advanced Wound-healing Technologies*. Journal of the American Podiatric Medical Association, 2010. **100**(5): p. 385-394.
3. Kloth, L.C. and J.A. Feedar, *Acceleration of wound healing with high voltage, monophasic, pulsed current*. Physical Therapy, 1988. **68**(4): p. 503-508.
4. Carley, P.J. and S.F. Wainapel, *Electrotherapy for acceleration of wound healing: low intensity direct current*. Archives of physical medicine and rehabilitation, 1985. **66**(7): p. 443-446.
5. Min Zhao, J.P., and Roslyn Rivkah Isseroff, *Electrical Activation of Wound-Healing Pathways*. Advances in Skin and Wound Care, 2010. **1**(1): p. 567-573.
6. Zhiqiang Zhao, C.W., Alexandra Karystinou, Anke J. Roelofs, Colin D. McCaig, Iain R. Gibson and Cosimo De Bari, *Directed migration of human bone marrow mesenchymal stem cells in a physiological direct current electric field*. European Cells and Materials, 2011. **22**(2011): p. 344-358.
7. Dewu, L., et al. *Amniotic membrane loaded with bone marrow mesenchymal stem cells facilitates the healing of deep burn wound*. in *Biomedical Engineering and Informatics (BMEI), 2010 3rd International Conference on*. 2010.

8. Kim, C.H., et al., *Mesenchymal Stem Cells Improve Wound Healing In Vivo via Early Activation of Matrix Metalloproteinase-9 and Vascular Endothelial Growth Factor*. J Korean Med Sci, 2011. **26**(6): p. 726-733.

9. Wesley M Jackson, L.J.N., Rocky S Tuan, *Mesenchymal stem cell therapy for the attenuation of scar formation during wound healing.* Stem Cell Research & Therapy, 2012. **3**(20).

10. Zhang, Q.-Z., et al., *Human Gingiva-Derived Mesenchymal Stem Cells Elicit Polarization of M2 Macrophages and Enhance Cutaneous Wound Healing.* STEM CELLS, 2010. **28**(10): p. 1856-1868.

11. Badiavas, E.V. and V. Falanga, *Treatment of chronic wounds with bone marrow–derived cells.* Archives of Dermatology, 2003. **139**(4): p. 510-516.

12. Arbab, A.S., et al., *Characterization of Biophysical and Metabolic Properties of Cells Labeled with Superparamagnetic Iron Oxide Nanoparticles and Transfection Agent for Cellular MR Imaging.* Radiology, 2003. **229**(3): p. 838-846.

13. Yue Pan, X.D., Fan Zhao, Bing Xu, *Magnetic Nanoparticles for the manipulation of proteins and cells.* Chemical Society Reviews, 2012. **41**: p. 2912-2942.

14. Cromer Berman, S.M., et al., *Cell motility of neural stem cells is reduced after SPIO-labeling, which is mitigated after exocytosis.* Magnetic Resonance in Medicine, 2013. **69**(1): p. 255-262.

15. Denitsa Docheva, D.P., Cvetan Popov, Wolf Mutschler, Hauke Clausen-Schaumann, Matthias Schieker, *Researching into the cellular shape, volume and elasticity of mesenchymal stem cells, osteoblasts and osteosarcoma cells by*

atomic force microscopy. Journal of Cellular and Molecular Medicine, 2007. **12**(2): p. 537-552.

16. Koivisto, L., et al., *HaCaT keratinocyte migration is dependent on epidermal growth factor receptor signaling and glycogen synthase kinase-3alpha*. Exp Cell Res, 2006. **312**(15): p. 2791-805.
17. Peura M, B.J., Salmenpera P, Noro A, Korhonen M., *Bone marrow mesenchymal stem cells undergo nemosis and induce keratinocyte wound healing utilizing the HGF/c-Met/PI3K pathway*. Wound Repair and Regeneration, 2009. **17**(4): p. 569-577.
18. Wollina, U., et al., *The Use of Biophysical Technologies in Chronic Wound Management*, in *Measurements in Wound Healing*. 2013, Springer. p. 313-354.
19. Dunn L, P.H., Tan JT, Vanags LZ, Ng MK, Bursill CA, *Murine model of wound healing*. J Vis Exp, 2013. **28**(75).
20. Gissel, H., R. Lee, and J. Gehl, *Electroporation and Cellular Physiology*, in *Clinical Aspects of Electroporation*, S.T. Kee, J. Gehl, and E.W. Lee, Editors. 2011, Springer New York. p. 9-17.
21. Sujata Sarabahi, V.T., *Principles and Practice of Wound Care*. 1st ed. 2012: Jaypee Brothers Medical Publishers (P) Ltd.
22. Bao, G., J.C. Bischof, and P. Decuzzi, *Challenges for Engineers in Biomedical and Clinical Sciences*. Journal of Nanotechnology in Engineering and Medicine, 2012. **3**: p. 020202.

23. Landázuri, N., et al., *Magnetic Targeting of Human Mesenchymal Stem Cells with Internalized Superparamagnetic Iron Oxide Nanoparticles.* Small, 2013. **9**(23): p. 4017-4026.

24. Shen, H., et al., *Structural responses of cells to intracellular magnetic force induced by superparamagnetic iron oxide nanoparticles.* Physical Chemistry Chemical Physics, 2014. **16**(5): p. 1914-1920.

25. Tong, S., et al., *Coating Optimization of Superparamagnetic Iron Oxide Nanoparticles for High T2 Relaxivity.* Nano Letters, 2010. **10**(11): p. 4607-4613.

26. Howe, D.S., *A WIRELESS ELECTRICAL STIMULATION SYSTEM FOR WOUND HEALING THERAPY WITH BIPHASIC HIGH-VOLTAGE PULSED CURRENT OUTPUT*. 2013, Case Western Reserve University.

27. Moulin, V.J., et al., *Electric Potential Across Epidermis and Its Role During Wound Healing Can Be Studied by Using an In Vitro Reconstructed Human Skin.* Advances in Wound Care, 2012. **1**(2): p. 81-87.

28. Gupta, A.K. and M. Gupta, *Synthesis and surface engineering of iron oxide nanoparticles for biomedical applications.* Biomaterials, 2005. **26**(18): p. 3995-4021.

29. Sophie Laurent, D.F., Marc Port, Alain Roch, Caroline Robic, Luce Vander Elst, Robert N Muller, *Magnetic Iron Oxide Nanoparticles: Synthesis, Stabilization, Vectorization, Physicochemical Characterizations, and Biological Applications.* Chemical Reviews American Chemical Society, 2008. **108**(6): p. 2064-2110.

30. Sun, C., J.S. Lee, and M. Zhang, *Magnetic nanoparticles in MR imaging and drug delivery.* Adv Drug Deliv Rev, 2008. **60**(11): p. 1252-65.

31. Mitchison, T. and L. Cramer, *Actin-based cell motility and cell locomotion.* Cell, 1996. **84**(3): p. 371-379.

32. Mogilner, A., *Mathematics of cell motility: have we got its number?* Journal of mathematical biology, 2009. **58**(1-2): p. 105-134.

33. Edward A Coding, M.J.P., Simon Benhamou, *Random walk models in biology.* Interface, 2008. **10**(14): p. 1098-2021.

34. Daniel Campos, V.M., Isaac Llopis, *Persistent random motion: Uncovering cell migration dynamics.* Journal of Theoretical Biology, 2010. **267**: p. 526-534.

35. Pollard, T.D. and G.G. Borisy, *Cellular motility driven by assembly and disassembly of actin filaments.* Cell, 2003. **112**(4): p. 453-465.

36. Peskin, C.S., G.M. Odell, and G.F. Oster, *Cellular motions and thermal fluctuations: the Brownian ratchet.* Biophysical journal, 1993. **65**(1): p. 316-324.

37. Bershadsky, A., M. Kozlov, and B. Geiger, *Adhesion-mediated mechanosensitivity: a time to experiment, and a time to theorize.* Current opinion in cell biology, 2006. **18**(5): p. 472-481.

38. Volarevic, V., et al., *Concise Review: Mesenchymal Stem Cell Treatment of the Complications of Diabetes Mellitus.* STEM CELLS, 2011. **29**(1): p. 5-10.

39. Kwon, D.S., et al., *Treatment with bone marrow-derived stromal cells accelerates wound healing in diabetic rats.* International Wound Journal, 2008. **5**(3): p. 453-463.

40. Walter, M.N.M., et al., *Mesenchymal stem cell-conditioned medium accelerates skin wound healing: An in vitro study of fibroblast and keratinocyte scratch assays.* Experimental Cell Research, 2010. **316**(7): p. 1271-1281.

41. Hocking, A.M. and N.S. Gibran, *Mesenchymal stem cells: Paracrine signaling and differentiation during cutaneous wound repair.* Experimental Cell Research, 2010. **316**(14): p. 2213-2219.

42. Dubé, J., et al., *Restoration of the transepithelial potential within tissue-engineered human skin in vitro and during the wound healing process in vivo.* Tissue Engineering Part A, 2010. **16**(10): p. 3055-3063.

43. Williams, A.R. and J.M. Hare, *Mesenchymal Stem Cells Biology, Pathophysiology, Translational Findings, and Therapeutic Implications for Cardiac Disease.* Circulation research, 2011. **109**(8): p. 923-940.

44. Yu, J., et al., *The use of human mesenchymal stem cells encapsulated in RGD modified alginate microspheres in the repair of myocardial infarction in the rat.* Biomaterials, 2010. **31**(27): p. 7012-7020.

45. Ranganath, S.H., et al., *Harnessing the mesenchymal stem cell secretome for the treatment of cardiovascular disease.* Cell stem cell, 2012. **10**(3): p. 244-258.

46. Li, H., et al., *Paracrine factors released by GATA-4 overexpressed mesenchymal stem cells increase angiogenesis and cell survival.* American Journal of Physiology-Heart and Circulatory Physiology, 2010. **299**(6): p. H1772-H1781.

47. Peplow, P.V. and M.P. Chatterjee, *A review of the influence of growth factors and cytokines in in vitro human keratinocyte migration.* Cytokine, 2013. **62**(1): p. 1-21.

48. Kolosnaj-Tabi J, W.C., Clement O, Gazeau F, *Cell labeling with magnetic nanoparticles: opportunity for magnetic cell imaging and cell manipulation.* Journal of Nanobiotechnology, 2013. **11**.

49. J.H. Lee, E.S.K., M.H. Cho, M. Son, S.I. Yeon, J.S. Shin, J. Cheon, Angew. Chem. Int. Ed., 2010. **49**: p. 5698-5702.

50. Bharde AA, P.R., Fritsch C, Klaver A, Kanger JS, Jovin TM, Arndt-Jovin DJ, *Magnetic nanoparticles as mediatiors of ligand-free activation of EGFR signaling.* PLoS one, 2013. **8**(7).

51. D.H. Kim, E.A.R., I.V. Ulasov, S.D. Bader, T. Rajhn, M.S. Lesniak, V. Novosad, Nature Materials, 2010(9): p. 165-171.

52. Roman Gorelik, A.G., *Quantitative and unbiased analysis of directional persistence in cell migration.* Nature Protocols, 2014. **9**: p. 1931-1943.

53. Ludovic G. Vincent, Y.S.C., Baldomero Alonso-Latorre, Juan C. del Alamo, Adam J Engler, *Mesenchymal Stem Cell Durotaxis Depends on Substrate Stiffness Gradient Strength.* Journal of Biotechnology, 2013. **8**(4): p. 472-484.

54. Nuccitelli, R., *A role for endogenous electric fields in wound healing.* Current topics in developmental biology, 2003. **58**: p. 1-26.

55. Furuta, Y., et al., *Reduced cell motility and enhanced focal adhesion contact formation in cells from FAK-deficient mice.* Nature, 1995. **377**(6549): p. 539-544.

56. Justin, R.T. and A.J. Engler, *Stiffness gradients mimicking in vivo tissue variation regulate mesenchymal stem cell fate.* PloS one, 2011. **6**(1): p. e15978.

57. Etoc F, L.D., Bellaiche Y, Piehler J, Coppey M, Dahan M, *Subcellular control of Rac-GTPase signalling by magnetogenetic manipulation inside living cells.* Nature Nanotechnology, 2013. **8**(3): p. 193-198.

58. Denitsa Docheva, D.P., Cvetan Popov, Wolf Mutschler, Hauke Clausen-Schaumann, Matthias Schieker, *Researching into the cellular shape, volume and*

elasticity of mesenchymal stem cells, osteoblasts and osteosarcoma cells by atomic force microscopy. Journal of Cellular and Molecular Medicine, 23 October 2007. **12**(2): p. 537-552.

59. Avrum I Gotlieb, L.M.M., Lalitha Subrahmanyan, Vitauts I Kalnins, *Distribution of Microtubule Organizing Centers in Migrating Sheets of Endothelial Cells.* The Journal of Cell Biology, 1981. **91**: p. 589-594.

60. Bischoff M, C.Z., *Cell rearrangements, cell divisions and cell death in a migrating epithelial sheet in the abdoment of Drosophila.* Development, 2009. **136**(14): p. 2403-2411.

61. Joel A. Swanson, A.L., Patricia Ansel, Peter J. Hollenbeck, *Radial movement of lysosomes along microtubules in permeabilized macrophages.* Journal of Cell Science, 1992(103): p. 201-209.

62. Alex Carisey, C.B., *Vinculin, an adapter protein in control of cell adhesion signalling.* European Journal of Cell Biology, 2011. **90**: p. 157-163.

63. Haase, I., et al., *Regulation of keratinocyte shape, migration and wound epithelialization by IGF-1-and EGF-dependent signalling pathways.* Journal of cell science, 2003. **116**(15): p. 3227-3238.

64. Tsuboi, R., et al., *Stimulation of keratinocyte migration by growth factors.* J Dermatol, 1992. **19**(11): p. 652-3.

65. Cha, D., et al., *Enhanced Modulation of Keratinocyte Motility by Transforming Growth Factor-∝(TGF-∝) Relative to Epidermal Growth Factor (EGF).* Journal of investigative dermatology, 1996. **106**(4).

66. Hardwicke, J., et al., *Bioresponsive Dextrin− rhEGF Conjugates: In Vitro Evaluation in Models Relevant to Its Proposed Use as a Treatment for Chronic Wounds*. Molecular pharmaceutics, 2010. **7**(3): p. 699-707.

67. Brem, H., et al., *Mechanism of sustained release of vascular endothelial growth factor in accelerating experimental diabetic healing.* Journal of Investigative Dermatology, 2009. **129**(9): p. 2275-2287.

68. Tochio, T., et al., *Fructose-1, 6-bisphosphate aldolase A is involved in HaCaT cell migration by inducing lamellipodia formation.* Journal of dermatological science, 2010. **58**(2): p. 123-129.

69. Radek, K.A., K.R. Taylor, and R.L. Gallo, *FGF-10 and specific structural elements of dermatan sulfate size and sulfation promote maximal keratinocyte migration and cellular proliferation.* Wound Repair and Regeneration, 2009. **17**(1): p. 118-126.

70. Tsuboi, R., et al., *Keratinocyte Growth Factor (FGF-7) Stimulates Migration and Plasminogen Activator Activity of Normal Human Deratinocytes.* Journal of investigative dermatology, 1993. **101**(1).

71. Nam, H.-J., et al., *Co-treatment with hepatocyte growth factor and TGF-β1 enhances migration of HaCaT cells through NADPH oxidase-dependent ROS generation.* Experimental & molecular medicine, 2010. **42**(4): p. 270-279.

72. Räsänen, K. and A. Vaheri, *TGF-beta1 causes epithelial-mesenchymal transition in HaCaT derivatives, but induces expression of COX-2 and migration only in benign, not in malignant keratinocytes.* Journal of dermatological science, 2010. **58**(2): p. 97-104.

73. Amanda K.A. Silva, N.L., Florence Gazeau, Kelly Aubertin, Stephanie Bonneau, Cedric Chauvierre, Didier Letourneaur, Claire Wilhelm, *Combining magnetic nanoparticles with cell derived microvessicles for drug loading and targeting.* Nanomedicine: Nanotechnology, Biology and Medicine, 2015. **11**(9).

74. Engler, A.J., et al., *Matrix elasticity directs stem cell lineage specification.* Cell, 2006. **126**(4): p. 677-689.